UNIVERSITÀ DELLA CALABRIA

UNIVERSITA' DELLA CALABRIA

Dipartimento di Fisica

Scuola di Dottorato

"Bernardino Telesio"

Indirizzo

Sistemi Complessi

Con il contributo di

Commissione Europea, Fondo Sociale Europeo e Regione Calabria

CICLO

XXVIII

INTERACTION OF WAVES AND PARTICLES WITH INHOMOGENEOUS STRUCTURES IN HELIOSPHERIC PLASMAS

Settore Scientifico Disciplinare FIS/05

Direttore: Prof. Roberto Bartolino

Firma _____

Supervisore: Prof. Francesco Malara

Firma _____

Dottorando: Dott. Francesco Pucci

Firma _____

Abstract

In questo lavoro vengono affrontati alcuni problemi ancora non risolti che riguardano la fisica dell'eliosfera. Nell'introduzione vengono esposti i risultati finora raggiunti nella ricerca in questo campo e presentate le tematiche, ancora oggetto di dibattito scientifico, che vengono affrontate nel lavoro.

Il primo capitolo riguarda la messa a punto di un codice numerico per la risoluzione delle equazioni della magnetoidrodinamica (MHD) in configurazione 2.5 dimensionale; in particolare, sono state implementate delle condizioni al contorno che simulano l'ingresso di onde mediante moti trasversali, oppure bordi aperti, in entrambi i casi utilizzando un metodo basato sulle caratteristiche proiettate. Tale codice è stato usato per modellizzare l'interazione tra onde e strutture di equilibrio disomogenee alla base dei "buchi coronali", ossia quelle regioni dell'atmosfera solare da cui si origina il vento solare. Il modello ha mostrato la formazione precoce di uno spettro, con formazione di piccole scale localizzate lungo le separatrici magnetiche oppure in vicinanza dei punti neutri ad X, ove ha luogo un fenomeno di riconnessione magnetica alternata.

Il secondo capitolo è dedicato allo studio della generazione di Kinetic Alfvén Waves a seguito della propagazione di onde di Alfvén in mezzi disomogenei. Tale lavoro è stato svolto sia tramite l'impiego di simulazioni Hall-MHD, sia di simulazioni cinetiche di tipo Vlasov-ibrido; queste ultime hanno permesso di evidenziare la formazione di strutture non-termiche nella funzione di distribuzione degli ioni, come anisotropie di temperatura e fasci di particelle accelerate.

Nel terzo capitolo viene affrontato il problema della accelerazione di particelle in turbolenza. Attraverso simulazioni di tipo "test particle" viene studiato il processo di accelerazione di particelle in una turbolenza 3D ottenuta in approssimazione di MHD ridotta. I risultati prelimanari mostrano una prevalenza di accelerazione nella direzione del campo magnetico medio e una dipendenza dell'accelerazione dal numero di Reynolds del sistema fisico considerato.

Il quarto capitolo rigurda il problema del trasporto di particelle in turbolenza MHD. Utilizzando un modello di turbolenza sintetica, è stato condotto uno studio parametrico che ha evidenziato come i coefficienti di diffusione parallelo e perpendicolare al campo magnetico medio dipendono da

parametri quali la lunghezza dello spettro, l'ampiezza delle fluttuazioni e il livello di intermittenza. I risultati ottenuti trovano applicazione a numerosi problemi riguardanti la diffusione di particelle energetiche nell'eliosfera.

Infine, nelle conclusioni vengono riassunti brevemente i risultati ottenuti e presentati i possibili sviluppi delle ricerche effettuate.

La presente tesi è cofinanziata con il sostegno della Commissione Europea, Fondo Sociale Europeo e della Regione Calabria. L'autore è il solo responsabile di questa tesi e la Commissione Europea e la Regione Calabria declinano ogni responsabilità sull'uso che potrà essere fatto delle informazioni in essa contenute.

Contents

Introduction

The Heliosphere is the region of influence of our star, the Sun. It contains all the solar system and extends beyond it. It is formed by the continuous flux of particles that emanates from Sun surface, called solar wind, and stops its expansion where the solar wind pressure is balanced by the pressure of the interstellar medium. The Sun, that is the main character in the Heliosphere, determines its feature and the majority of its dynamics. Matter in the heliosphere is principally present in the form of plasma, an ionized gas where positive ions and electrons are not bounded to form atoms. The Sun, the solar wind and the interplanetary medium are made of plasma.

The exploration of the heliosphere has been one of the most exciting scientific challenge of the last decades. Starting from the sixties of last century many satellites have been launched to study the medium that surrounds Earth. In these missions a huge amount of data have been collected. Sun and planets imaging, measures of electric and magnetic field and particle distribution functions in the solar wind, have been the legacy of this technical and scientific effort. Many new phenomena arises from these observation, to which in the last few decades the scientific community has tried to give an answer.

The observations showed that the heliosphere is not an homogeneous medium. The plasma characteristic quantities, like density and tempera-

ture, and the background electric and magnetic field varies in space and time in a broad range of scales. This is not only due to the presence of waves that propagates in such an homogeneous medium, but also to turbulence that is the phenomenon responsible for the transport of energy from bigger to smaller scales. Moreover, the heliospheric plasma is not at thermal equilibrium. It is in fact populated by suprathermal particles whose energies are sometimes even relativistic.

In this work we study the interaction of these features, in particular waves and particles, with typical inhomogeneous structures present in the heliosphere. To tackle this kind of problem, since the equation involved in the plasma mathematical description cannot be solved analytically, a numerical approach is required in all the cases.

The first chapter regards the problem of the interaction of magnetohydrodynamics (MHD) waves with the inhomogeneous magnetic field of a low layers of a coronal hole. A 2.5D numerical model with a method of projected characteristics for simulating open boundaries is employed to study the propagation of such a waves in a potential magnetic field with open and closed field lines where also an X-point is present. A section of the chapter is dedicated to describe the simulation setup with a particular attention payed in the description of the method of characteristics employed. Then results are presented comparing the two different phenomenology that arises from injecting magnetosonic or Alfvén modes.

The second chapter is devoted to the study of a problem at smaller scales. The propagation of an Alfvén wave in a pressure-balanced structure is considered in the linear case using an Hall MHD model and in the non linear case using an Hybrid Vlasov-Maxwell model. The aim of the study is to characterize what kind of fluctuations arises from this interaction, when

fluctuations at scales comparable to the proton inertial length are considered.

The third and fourth chapters are dedicated to the problem of particle acceleration and diffusion respectively. For the first one we use a test particle approach to track the energization of particles in an electromagnetic field generated by a 3D Reduced MHD turbulence. For the second one a different approach is used in the modeling. In fact a synthetic turbulence model is proposed for generating the magnetic field and diffusion of test particle in such a field are performed in order to single out how the characteristics of the turbulence affect transport.

In the conclusion, the results obtained in all the problem studied are summarized and possible future works are discussed

The appendices are dedicated to more numerical aspects. In the first one we describe how the vector potential of the equilibrium magnetic field considered in Chapter 1 is calculated. The second one is devoted to the comparison among different numerical scheme that can be employed to solve the Lorentz equations in test particle simulations. In the third one the numerical code realized for test particle simulations presented in Chapter 3 and 4 is described in terms of capability and performances.

Chapter 1

Evolution of magnetohydrodynamic waves in low layers of a coronal hole

Low-frequency fluctuations in the domain of magnetohydrodynamics (MHD) are believed to populate the plasma of the solar corona. These fluctuations originate from photospheric motions and propagate up to the corona along the magnetic field that permeates the solar atmosphere. In situ measurements have revealed MHD fluctuations in the solar wind for several decades (Belcher & Davis, 1971): this is considered to be an indirect indication of the presence of the same kind of fluctuations in the corona, from where the solar wind emanates. Evidence of velocity fluctuations of the order $\delta v \sim 30 - 50$ km s^{-1} in the corona at unresolved spatial and temporal scales has been deduced from nonthermal broadening of coronal lines (Acton et al., 1981; Warren et al., 1997; Chae et al., 1998). In recent years, velocity fluctuations have also been ubiquitously detected in the corona (Tomczyk et al., 2007; Tomczyk & McIntosh, 2009). Such fluctuations appear to propagate along

magnetic lines at a speed that is consistent with estimations of the Alfvén velocity; thus they are considered to be Alfvén waves, although a different interpretation has also been proposed in terms of kink magnetoacoustic waves (Van Doorsselaere et al., 2008). More recently, Alfvén waves with energy sufficient to power the quiet corona and fast solar wind have been found (McIntosh et al., 2011). Moreover, indirect evidences of Alfvén waves in coronal holes have also been reported (see (Banerjee et al., 2011) for a review).

Waves and turbulence are considered to be one of the energy sources responsible for solar wind expansion (Sorriso-Valvo et al., 2007; Marino et al., 2011; Hellinger et al., 2013). For instance, observed variations of proton temperature with the heliocentric distance are inconsistent with a simple adiabatic expansion, which instead requires a continuous heat deposition along the solar wind path (e.g., Matthaeus et al. (1999a)). Turbulence represents the best candidate to explain such an extended heating. Moreover, turbulence formation has been proposed as a mechanism responsible for solar wind acceleration in the near-Sun region. The main idea is that waves produced by photospheric motions propagate upward in coronal open-field regions, which is where the solar wind originates. As a result of vertical stratification and magnetic field expansion, these waves are partially reflected downward. Nonlinear interactions between MHD waves propagating in two opposite directions generate an energy cascade toward small scales, eventually dissipating part of the wave energy, which would then be responsible for both coronal heating and wind acceleration (Matthaeus et al., 1999b). Several models have been proposed within such a framework: a model of Alfvén wave propagation in the chromosphere and the corona, in which heating and acceleration are a consequence of compressive waves and

shocks formation (Suzuki & Inutsuka, 2005); a model ranging from the chromosphere to the corona, which includes the effects of pressure and acoustic wave gradients (Cranmer et al., 2007); models where nonlinear effects are modeled by phenomenological terms (Verdini & Velli, 2007), by a simplified representation of the wavevector space (shell model, Verdini et al. (2009)), or a strong turbulence closure (Verdini et al., 2010).

In these models, the background structure where perturbations propagate contains a unipolar magnetic field possibly varying on a relatively large spatial scale, at least in the coronal part of the considered domain. Indeed, coronal holes and solar wind are both characterized by a mainly unipolar magnetic field (McComas et al., 2000). However, magnetograms taken in coronal hole regions show a complex structure at low altitudes that is characterized by areas of both magnetic polarities (Zhang et al., 2006). Thus, the magnetic field at low altitude in a coronal hole has a complex 3D structure containing open fieldlines extending to larger altitudes and closed fieldlines connecting regions of opposite polarities (Ito et al., 2010). Perturbations generated by photospheric motions, which cross this complex structure when propagating upward, couple with gradients of the background. As a result, small scales are generated in the perturbations. The present chapter focuses on the mechanism of small-scale formation due to the coupling between perturbation and background inhomogeneity, which has not been considered in the previously cited models.

The evolution of hydromagnetic perturbations propagating in an inhomogeneous background has been widely studied. In a 2D inhomogeneous background, where the Alfvén velocity varies in directions perpendicular to the magnetic field, two mechanisms have been investigated in detail: (1) phase-mixing (Heyvaerts & Priest, 1983), in which differences in group ve-

locity at different locations progressively bend wavefronts; and (2) resonant absorption that concentrates the wave energy in a narrow layer where the local wave frequency matches a characteristic frequency (Alfvén or cusp). These processes have been studied by investigating normal modes of the inhomogeneous structure (Kappraff & Tataronis, 1977; Mok & Einaudi, 1985; Steinolfson, 1985; Davila, 1987; Hollweg, 1987; Califano et al., 1990, 1992) and by considering the evolution of an initial disturbance (Lee & Roberts, 1986; Malara et al., 1992, 1996). The effects of density stratification and magnetic line divergence (Ruderman et al., 1998), as well as nonlinear coupling with compressive modes Nakariakov et al. (1997, 1998), have also been considered. The propagation of MHD waves in magnetic fields containing null points has been studied in detail too (Landi et al., 2005) (see also McLaughlin et al. (2010) for a review).

Studing the evolution of MHD perturbations in 3D structures is more complex. In particular, the evolution of Alfvén waves has been studied using a simplified approach based on a WKB method first proposed by Similon & Sudan (1989), and was also studied in detail both from a general point of view (Petkaki et al., 1998; Malara et al., 2000, 2003) and in the context of the coronal heating problem (Malara et al., 2005, 2007). The same method was used by Malara et al. (2012), and in more detail by Malara (2013), to study the evolution of Alfvén waves propagating in a 3D magnetic field that models the magnetic structure in an open fieldline region with the previously described features (Ito et al., 2010). The results showed that small scales form in the Alfvénic perturbation at very low altitudes ($\sim 10^5$ km above the coronal base) as a consequence of its interactions with specified equilibrium field inhomogeneities. Such small scales are located at magnetic separatrices and the resulting spectra of the perturbation have a power-law dependence,

with a large prevalence of wavevectors perpendicular to the magnetic field.

The main limitations in the model by Malara (2013) are due to the WKB approximation, which assumes that the perturbation wavelength λ is much smaller than the scale of variation of the equilibrium structure, which is of the order of $L_{eq} \sim 3 \times 10^4$ km. Assuming a typical Alfvén velocity $c_A \sim 500$ km s^{-1} and a timescale of perturbations $\tau \sim 500$ s, the wavelength in the direction parallel to the magnetic field is $\lambda_{||} = c_A \tau \sim 2.5 \times 10^5$ km. Thus, the assumption of small wavelength is somewhat questionable. Moreover, all compressive effects have been neglected in this model.

In the present work we try to overcome these limitations of the WKB method by using full compressible MHD simulations instead. In particular, a simplified 2D version of the equilibrium magnetic field used in Malara (2013) is considered, in which both Alfvénic and magnetosonic fluctuations are generated by transverse motions at the base of the domain. The dynamics of the system and the generation of small scales in perturbations after crossing the background inhomogeneity are investigated. Most of the results obtained by the WKB approach are recovered, along with new effects, which are mainly related to the compressive component of perturbations. The implications for the problem of solar wind acceleration and understanding the presence of density fluctuations in the open fieldline corona are discussed.

1.1 The model

We consider an open-field line region of the solar corona. The configuration is given by an inhomogeneous MHD equilibrium with superimposed fluctuations that propagate in the upward direction. We study the dynamics of the interaction between fluctuations and the inhomogeneous background using numerical simulations.

The spatial domain represents a small portion of a coronal hole that is located just above the coronal base. We indicate all quantities relating to the equilibrium configuration by the upper index "(0)". A detailed description of the equilibrium magnetic field $\mathbf{B}^{(0)}$ is available elsewhere (Malara, 2013); in the following we summarize the assumptions and describe the derivation. Although a coronal hole is characterized by an essentially unipolar magnetic field, magnetograms of coronal hole regions (Zhang et al., 2006; Ito et al., 2010) show that there are low lying regions where the photospheric magnetic field has a polarity opposite to the dominant one. The areas of the two polarities appear to be intermixed, forming a complex structure with different spatial scales ranging from $\sim 10^9$ cm down to the resolution limit. The area corresponding to the flux with the dominant polarity represents $\sim 70\%$ of the total area, whereas the remaining 30% corresponds to the opposite polarity (Zhang et al., 2006). The coronal magnetic field above such regions should also have a complex structure: magnetic lines connecting the regions of opposite polarity should be present, along with open magnetic lines emanating from dominant polarity regions. At sufficiently high altitudes only open magnetic lines should be found, with the magnetic field structure becoming less complex (Zhang et al., 2006; Ito et al., 2010). The magnetic field model considered here ctries to represent the above described features in a very simplified form.

Due to the smallness of the considered spatial domain, we neglect curvature effects due to the spherical geometry, and use a Cartesian reference frame XYZ in which the YZ plane corresponds the coronal base, while the X-axis is directed vertically upward. The spatial domain is $D = \{(X, Y, Z)\} = [0, L] \times [0, R_y L] \times [0, R_z L]$, where L is of the order of the characteristic scale of the magnetic field at the coronal base, while the aspect

ratios R_y and R_z are quantities of order 1. The magnetic field structure is more complex at low altitudes, while the influence of boundary conditions at the base $X = 0$ decreases with increasing altitude X. Then, we assume that the equilibrium magnetic field $\mathbf{B}^{(0)}(\mathbf{r})$ becomes uniform and vertically directed at large altitudes X:

$$\lim_{X\to+\infty} \mathbf{B}^{(0)}(X, Y, Z) = B_0 \mathbf{e}_x \tag{1.1}$$

where B_0 is a constant and $\mathbf{e}_x$ is the unit vector in the X-direction. Moreover, we choose $B_0 > 0$ corresponding to a positive polarity at sufficiently high altitudes. Periodicity in the horizontal Y and Z directions is assumed. Because the coronal plasma has a low β, the equilibrium condition requires that $\mathbf{B}^{(0)}$ is a force-free magnetic field:

$$\nabla \times \mathbf{B}^{(0)} = \alpha \mathbf{B}^{(0)} \tag{1.2}$$

where the scalar quantity α is constant along fieldlines. The condition (1.1) implies that α is vanishing at large altitudes and along open fieldlines. Thus, the simplest choice is to assume that $\alpha = 0$ in the whole domain. This assumption is expressed by the condition:

$$\mathbf{B}^{(0)} = -\nabla \Phi \tag{1.3}$$

where the scalar potential Φ must satisfy the Laplace equation

$$\nabla^2 \Phi = 0 \tag{1.4}$$

which follows from the divergence-free condition for $\mathbf{B}^{(0)}$. Using periodicity,

Φ can be expanded in a Fourier series along Y and Z

$$\Phi(X,Y,Z) = \sum_{k_y,k_z} \hat{\Phi}_{k_y,k_z}(X)\, e^{i(k_y Y + k_z Z)} \tag{1.5}$$

where $k_y = 2\pi n/(R_y L)$ and $k_z = 2\pi m/(R_z L)$, with n and m integers. The Laplace Equation (1.4) gives an equation for the Fourier coefficients $\hat{\Phi}_{k_y,k_z}(X)$:

$$\frac{d^2\hat{\Phi}_{k_y,k_z}(X)}{dX^2} = -\left(k_y^2 + k_z^2\right)\hat{\Phi}_{k_y,k_z}(X) \tag{1.6}$$

The solution of Equation (1.6) for $k_y = k_z = 0$ is:

$$\hat{\Phi}_{0,0}(X) = a + bX \tag{1.7}$$

with a and b constants, corresponding to a homogeneous magnetic field. We can set $a = 0$ without lack of generality, while we choose $b = -B_0$. The latter condition is related to the assumption (1.1). The solution for $(k_y, k_z) \neq (0,0)$ is:

$$\hat{\Phi}_{k_y,k_z}(X) = A_{k_y,k_z} e^{-h(k_y,k_z)X} + C_{k_y,k_z} e^{h(k_y,k_z)X} \tag{1.8}$$

with

$$h(k_y,k_z) = \sqrt{k_y^2 + k_z^2} \tag{1.9}$$

and A_{k_y,k_z} and C_{k_y,k_z} constants. The term proportional to C_{k_y,k_z} would give a magnetic field that diverges in the limit $X \to +\infty$. For this reason we discard this solution and choose $C_{k_y,k_z} = 0$. Then, using expressions (1.7) and (1.8), we get:

$$\Phi(X,Y,Z) = \sum_{k_y,k_z \neq (0,0)} A_{k_y,k_z} e^{-h(k_y,k_z)X + i(k_y Y + k_z Z)} - B_0 X \tag{1.10}$$

The last equation can be simplified because Φ is a real quantity, which implies that $A_{-k_y,-k_z} = A^*_{k_y,k_z}$, where the asterisk indicates complex conjugate. Using this condition, expression (1.10) can be written in the following form containing only real quantities:

$$\Phi(X,Y,X) = \sum_{\substack{(k_y,k_z)\neq(0,0)\\ k_z\geq 0}} \phi_{k_y,k_z}\cos(k_yY + k_zZ + \gamma_{k_y,k_z})e^{-h(k_y,k_z)X} - B_0X \tag{1.11}$$

where $\phi_{k_y,k_z} = 2\Re(A_{k_y,k_z})$ and the phases γ_{k_y,k_z} can be chosen in the interval $[0, 2\pi]$. Finally, using expression (1.11) for the potential from Equation (1.3), we can calculate the components of the equilibrium magnetic field:

$$B_x^{(0)}(X,Y,Z) = \sum_{\substack{(k_y,k_z)\neq(0,0)\\ k_z\geq 0}} \Big[h(k_y,k_z)\phi_{k_y,k_z}\times \cos\big(k_yY + k_zZ + \gamma_{k_y,k_z}\big)e^{-h(k_y,k_z)X}\Big] + B_0 \tag{1.12}$$

$$B_y^{(0)}(X,Y,Z) = \sum_{\substack{(k_y,k_z)\neq(0,0)\\ k_z\geq 0}} k_y\phi_{k_y,k_z}\sin\big(k_yY + k_zZ + \gamma_{k_y,k_z}\big)e^{-h(k_y,k_z)X} \tag{1.13}$$

$$B_z^{(0)}(X,Y,Z) = \sum_{\substack{(k_y,k_z)\neq(0,0)\\ k_z\geq 0}} k_z\phi_{k_y,k_z}\sin\big(k_yY + k_zZ + \gamma_{k_y,k_z}\big)e^{-h(k_y,k_z)X} \tag{1.14}$$

Note that the above expressions satisfy condition (1.1). The equilibrium magnetic field (1.12)-(1.14), which is equivalent to the form used by Malara (2013), is a superposition of different harmonics at a given spatial scale determined by the wavevector (k_y, k_z). When many harmonics are present, the resulting magnetic field has a complex structure containing both open and closed fieldlines, with the latter connecting regions of opposite polarity at the base $X = 0$. Magnetic null points and separatrices are also present

(Malara, 2013). The details of the magnetic structure are determined by the choice of parameters (B_0, ϕ_{k_y,k_z} and γ_{k_y,k_z}). In the present case, the dynamics of the system are studied numerically for a 2D configuration in which all quantities depend only on X and Z. In order to better exploit the finite resolution allowed by the spatial grid we use a form for $\mathbf{B}^{(0)}$ that is as simple as possible, where only one single term is retained in the sums contained of Equations (1.12)-(1.14). This term corresponds to the smallest wavevector $(k_y, k_z) = (0, k_{1z})$, with $k_{1z} = 2\pi/(R_z L)$:

$$B_x^{(0)}(X, Z) = B_0[1 + b_1 \cos(k_{1z} Z) e^{-k_{1z} X}] \tag{1.15}$$

$$B_y^{(0)} = 0 \tag{1.16}$$

$$B_z^{(0)}(X, Z) = B_0 b_1 \sin(k_{1z} Z) e^{-k_{1z} X} \tag{1.17}$$

where $b_1 = k_{1z}\phi_{0,k_{1z}}/B_0$ and it has been chosen that $\gamma_{0,k_{1z}} = 0$. The above expressions contain two dimensionless quantities: the relative amplitude b_1 of the inhomogeneous component and the aspect ratio R_z. They are determined by requiring the fulfilment of two conditions: (1) the vertical component $B_x^{(0)}$ must change sign along the base $X = 0$ of the spatial domain, which corresponds to the inequality $|b_1| > 1$. In this case there is a magnetic null point above the coronal base ($X > 0$) located at the position $(X_0, Z_0) = (\ln b_1/k_{1z}, \pi/k_{1z})$ for $b_1 > 0$, or $(X_0, Z_0) = (\ln(-b_1)/k_{1z}, 0)$ for $b_1 < 0$. We also require that (2) the null point is inside the considered domain (i.e., $X_0 < L$). Conditions (1) and (2) correspond to

$$1 < |b_1| < e^{2\pi/R_z} \tag{1.18}$$

In particular, we have chosen $b_1 = 2$ and $R_z = \pi$, which satisfy the in-

equalities (1.18). In this case the magnetic null point is located at the position $(X_0, Z_0) = (L \ln 2/2, L\pi/2)$. The magnetic field (1.15)-(1.17) can be expressed in terms of a vector potential: $\mathbf{B}^{(0)} = \nabla \times (A^{(0)}\mathbf{e}_y)$, where

$$A^{(0)}(X, Z) = -\frac{B_0 b_1}{k_{1z}} \sin(k_{1z} Z) e^{-k_{1z} X} - B_0 Z \tag{1.19}$$

In Figure 1.1 magnetic lines of the equilibrium magnetic field $\mathbf{B}^{(0)}$ are

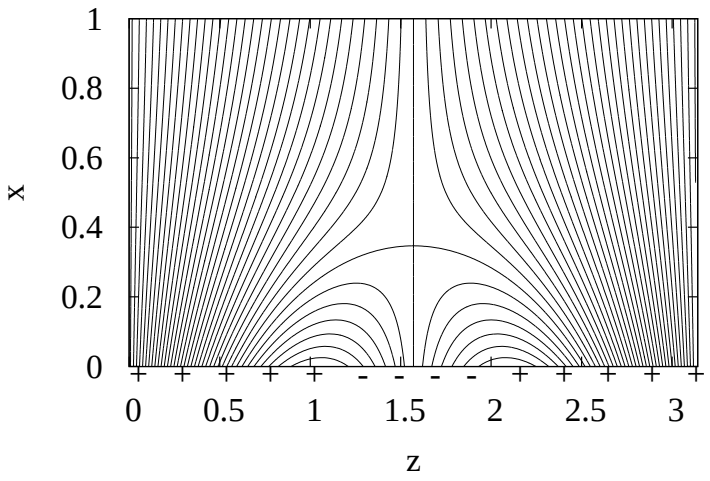

Figure 1.1: Magnetic lines of the equilibrium magnetic field $\mathbf{b}^{(0)}$ in the xz plane. The symbols "+" and "−" represent the polarity of the field at $x = 0$.

represented in the XZ-plane. This plot is obtained by drawing the isolines of the vector potential $A^{(0)}$ (Equation (1.19)). It can be seen that $B_x^{(0)}$ changes sign along the base $X = 0$; it is positive on the left and the right sides and negative in the central part. In the lower part of the domain both open and closed fieldlines are present, whereas only open fieldlines are found in the upper part of D. An X-type magnetic null point is located at the position (X_0, Z_0). Four separatrices intersect at the X-point: those starting from the

base of D separate the two regions of closed and open fieldlines, whereas the separatrix extending above the X-point separates open fieldlines coming from distant parts of the base. Finally, $\mathbf{B}^{(0)}$ tends to become uniform and vertically directed in the uppermost part of D, as required by the condition (1.1). Thus, despite its simple form, $\mathbf{B}^{(0)}$ reproduces all the features we want to model.

A magnetic field similar to that of our model is typically found at much larger scales in pseudostreamers, which are thin coronal structures extending radially up to several solar radii (Wang et al., 2007). A pair of loop arcades with an X-neutral line in between underlay a pseudostreamer, which is supposed to develop along the vertical separatrix (Wang et al., 2012). Thus the equilibrium magnetic field of our model can be considered a small-scale version of the magnetic structures commonly observed in the corona.

The equilibrium mass density and pressure are assumed to be uniform

$$\rho_m^{(0)}(X,Z) = \rho_{m0} = \text{const} \quad , \quad P^{(0)}(X,Z) = \text{const} \tag{1.20}$$

thus neglecting any stratification generated by gravity, whereas the equilibrium velocity is vanishing, $\mathbf{V}^{(0)} = 0$.

MHD waves are superposed on the above described equilibrium. No waves are present at the initial time $\tau = 0$, but they are continuously generated by imposing the velocity at the base $X = 0$. This boundary condition is intended to represent the effects of the motion of underlying denser layers on the coronal plasma, and are specified in the next sections.

1.2 Numerical method

In order to describe the evolution of the model, we numerically solve the nonlinear, compressible, non-ideal, 2D MHD equations:

$$\frac{\partial \rho_m}{\partial t} + \nabla \cdot (\rho_m \mathbf{V}) = 0, \tag{1.21}$$

$$\frac{\partial \mathbf{V}}{\partial t} + (\mathbf{V} \cdot \nabla)\, \mathbf{V} = -\frac{1}{\rho_m}\nabla P + \frac{1}{4\pi\rho_m}(\nabla \times \mathbf{B}) \times \mathbf{B} + \frac{\tilde{\nu}}{\rho_m}\nabla \cdot \vec{\vec{\Pi}}, \tag{1.22}$$

$$\frac{\partial \mathbf{B}}{\partial t} = \nabla \times (\mathbf{V} \times \mathbf{B}) + \frac{c^2\tilde{\eta}}{4\pi}\nabla^2\mathbf{B}, \tag{1.23}$$

$$\frac{\partial P}{\partial t} + \nabla \cdot (P\mathbf{V}) + (\gamma - 1)\, P\, (\nabla \cdot \mathbf{V}) = \tilde{\kappa}\nabla^2 T + (\gamma - 1)\left[\frac{c^2\tilde{\eta}}{(4\pi)^2}(\nabla \times \mathbf{B})^2 + \frac{\tilde{\nu}}{2}\vec{\vec{\Pi}} : \vec{\vec{\Pi}}\right] \tag{1.24}$$

with

$$T = \frac{\mu m_p}{k_B}\frac{P}{\rho_m} \tag{1.25}$$

and the components of the tensor $\vec{\vec{\Pi}}$ are

$$\Pi_{ij} = \frac{\partial \mathbf{V}_i}{\partial X_j} + \frac{\partial \mathbf{V}_j}{\partial X_i} - \frac{2}{3}\delta_{ij}\frac{\partial \mathbf{V}_k}{\partial X_k} \tag{1.26}$$

In the above equations ρ_m, P, T, $\mathbf{V}$, and $\mathbf{B}$ are the mass density, pressure, temperature, velocity and magnetic field, respectively. All physical quantities are functions of the spatial variables X and Z and of the time t. $\tilde{\nu}$, $\tilde{\eta}$, and $\tilde{\kappa}$ are the dynamic viscosity, resistivity, and thermal conductivity, respectively, and are assumed constant. k_b is the Boltzmann constant, c is the speed of light, m_p is the proton mass, $\mu \sim 1$ is the mean molecular weight.

We introduce dimensionless quantities:

$$x = \frac{X}{L}; \quad z = \frac{Z}{L}; \quad \tau = \frac{c_{A0}}{L}t; \quad \rho = \frac{\rho_m}{\rho_{m0}};$$

$$\mathbf{v} = \frac{\mathbf{V}}{c_{A0}}; \quad \mathbf{b} = \frac{\mathbf{B}}{B_0}; \quad p = \frac{P}{\rho_{m0} c_{A0}^2}$$

In these expressions $L = 10^9$ cm is the typical size of structures in coronal hole magnetograms (Zhang et al., 2006); $\rho_{m0} = 5 \times 10^{-16}$ g cm^{-3} is a typical density; $c_{A0} = 2.5 \times 10^7$ cm s^{-1} is a typical value of Alfvén velocity in coronal holes (McIntosh et al., 2011); and $B_0 = c_{A0}\sqrt{4\pi\rho_{m0}}$. Using the dimensionless variables, Equations (1.21)-(1.24) take the following form:

$$\frac{\partial \rho}{\partial \tau} + \nabla \cdot (\rho \mathbf{v}) = 0, \tag{1.27}$$

$$\frac{\partial \mathbf{v}}{\partial \tau} + (\mathbf{v} \cdot \nabla)\, \mathbf{v} = -\frac{1}{\rho}\nabla p + \frac{1}{\rho}\,(\nabla \times \mathbf{b}) \times \mathbf{b} + \frac{\nu}{\rho}\nabla \cdot \vec{\vec{\sigma}}, \tag{1.28}$$

$$\frac{\partial \mathbf{b}}{\partial \tau} = \nabla \times (\mathbf{v} \times \mathbf{b}) + \eta \nabla^2 \mathbf{b}, \tag{1.29}$$

$$\frac{\partial p}{\partial \tau} + \nabla \cdot (p\mathbf{v}) + (\gamma - 1)\, p\, (\nabla \cdot \mathbf{v}) = \kappa \nabla^2 \left(\frac{p}{\rho}\right) + (\gamma - 1)\left[\eta (\nabla \times \mathbf{b})^2 + \frac{\nu}{2}\vec{\vec{\sigma}} : \vec{\vec{\sigma}}\right] \tag{1.30}$$

with

$$\sigma_{ij} = \frac{\partial \mathbf{v}_i}{\partial x_j} + \frac{\partial \mathbf{v}_j}{\partial x_i} - \frac{2}{3}\delta_{ij}\frac{\partial \mathbf{v}_k}{\partial x_k} \tag{1.31}$$

and $\nu = \tilde{\nu}/(L\rho_{m0}c_{A0})$, $\eta = \tilde{\eta}c^2/(4\pi c_{A0}L)$, $\kappa = \tilde{\kappa}\mu m_p/(\kappa_b L \rho_{m0} c_{A0})$.

Using the new variables the spatial domain D is transformed into the domain $D' = \{(x, z)\} = [0, 1] \times [0, R_z]$. It is worth noting that for the aspect ratio we used, the value $R_z = \pi$, corresponds to the horizontal length $L_z \simeq 3 \times 10^9$ cm. The initial condition is given by the equilibrium structure specified in the previous section. The initial dimensionless density and pressure are $\rho = 1$ and $p = 0.05$, respectively, with the latter corresponding to a plasma beta value:

$$\beta = p\left[\frac{1}{R_z}\int_{D'} \frac{b^2}{2} dx dz\right]^{-1} \approx 5 \times 10^{-2}. \tag{1.32}$$

Concerning boundary conditions, the lower boundary $x = 0$ represents the border through which perturbations coming from layers underlying the corona are entering. On this boundary we impose the value of the velocity field. In particular, we consider two cases:

(a) uniform oscillatory motion at the base directed in the y-direction, $\mathbf{v}(x = 0, z, \tau) = v_1 \sin(\omega\tau)\mathbf{e}_y$, where v_1 and ω are the velocity amplitude and frequency, respectively. This boundary condition generates fluctuations propagating inside the domain with a polarization (y), which is perpendicular both to the equilibrium magnetic field $\mathbf{b}^{(0)}$ and the perturbation wavevector (which is in the xz-plane). For this reason we refer to this kind of fluctuation as *Alfvénic*.

(b) uniform oscillatory motion at the base directed in the z-direction, $\mathbf{v}(x = 0, z, \tau) = v_1 \sin(\omega\tau)\mathbf{e}_z$. In this case generated fluctuations are polarized in the plane containing both $\mathbf{b}^{(0)}$ and the wavevector. We refer to this kind of fluctuation as *magnetosonic*.

In both cases we used the value $\omega = \pi/2$ for the frequency, corresponding to a waveperiod $t_w = 160s$ and $v_1 = 0.1$ corresponding to the amplitude $V_1 = 2.5 \times 10^6$ cm s^{-1}, in accordance with observations (McIntosh et al., 2011). The value of other physical quantities at $x = 0$ is calculated using a method of projected characteristics (Nakagawa et al., 1987; Sun et al., 1995; Poinsot & Lele, 1993; Grappin et al., 2000; Landi et al., 2005). In our case, we use this method to evaluate ρ, p, and $\mathbf{b}$ in a way that is consistent with the values specified for the velocity field and with the MHD equations. A detailed description of this procedure is given in the next section.

The upper boundary $x = 1$ is a free boundary that must allow perturbations propagating inside the domain to exit without reflection. Again, the method of projected characteristics has been implemented on the upper

boundary to simulate this physical condition. The details of boundary conditions at $x = 1$ are given in the next section. Finally, periodic boundary conditions are imposed in the horizontal z-direction.

Equations (1.27)-(1.30), with the specified boundary conditions, are numerically solved by employing a Cartesian 2D version of a compressible MHD code that was originally written for 3D cylindrical configurations with time-dependent boundary conditions (Onofri et al., 2007). The uniform spatial grid is formed by $nx \times nz$ points ($nx = 1024$, $nz = 256$). A sixth-order finite difference method in the x-direction and a pseudospectral Fourier method in the z-direction are used. Time derivatives are calculated using a third-order Runge-Kutta scheme. Viscosity, resistivity, and thermal conductivity are uniform over the domain and constant: $\nu = \eta = \kappa = 10^{-3}$.

The Equation (1.30) can be rewritten in the form of an evolution equation for the internal energy density $u = p/(\gamma - 1)$:

$$\frac{\partial u}{\partial \tau} + \nabla \cdot (u\mathbf{v}) + (\gamma - 1)\, u\, (\nabla \cdot \mathbf{v}) = \kappa \nabla^2 \left(\frac{p}{\rho}\right) + P_\eta + P_\nu \tag{1.33}$$

where

$$P_\eta = \eta(\nabla \times \mathbf{b})^2; \qquad P_\nu = \frac{\nu}{2}\vec{\vec{\sigma}} : \vec{\vec{\sigma}} \tag{1.34}$$

are the dissipated power per unit volume due to resistivity and to viscosity, respectively. Other useful quantities are defined by

$$w_\eta(\tau) = \int_{D'} P_\eta(x, z, \tau)\, dxdz \quad ; \quad w_\nu(\tau) = \int_{D'} P_\nu(x, z, \tau)\, dxdz \tag{1.35}$$

which represent the dissipated resistive and viscous power integrated over the domain D'. Using Equations (1.27)-(1.29) and (1.33) it is possible to write a conservation law for total energy density in a differential form. In-

tegrating this equation on the domain D' and using the divengerce theorem gives the energy conservation equation:

$$\frac{dE}{d\tau} + \Phi = 0 \tag{1.36}$$

where

$$E = \int_{D'} \left(\frac{1}{2}\rho|\mathbf{v}|^2 + \frac{|\mathbf{b}|^2}{2} + u \right) dxdz \tag{1.37}$$

is the total energy per unit length in the domain D', and

$$\Phi = \oint_{\partial D'} \left[\left(\frac{1}{2}\rho|\mathbf{v}|^2 + \gamma u \right) \mathbf{v} + \mathbf{S} + \nu \left((\mathbf{v}\cdot\nabla)\,\mathbf{v} - (\nabla\cdot\mathbf{v})\,\mathbf{v} \right) - \kappa\nabla\left(\frac{p}{\rho}\right) \right] \cdot \hat{\mathbf{n}} dl \tag{1.38}$$

In this expression $\mathbf{S} = |\mathbf{b}|^2\mathbf{v} - (\mathbf{v}\cdot\mathbf{b})\mathbf{b} + \eta(\nabla\times\mathbf{b})\times\mathbf{b}$ is the Poynting vector, $\partial D'$ is the contour of D', $\hat{\mathbf{n}}$ is the outer-pointing normal to $\partial D'$, and dl is an infinitesimal piece of $\partial D'$. The quantity (1.38) represents the energy flux through the boundary that is due to four different effects: advection of matter, Poynting vector flux, viscous forces work along the boundaries, and heat flux. In our particular configuration, the net flux through the boundaries $z = 0$ and $z = R_z = \pi$ is null because of periodicity. Thus, we can write the total flux in the form $\Phi = \Phi_0 + \Phi_1$, where Φ_0 and Φ_1 are the fluxes through the boundaries $x = 0$ and $x = 1$, respectively. Taking into account the form of boundary conditions imposed at these boundaries (see next section) we find:

$$\Phi_0 = \int_{x=0} \left[-\eta\,(\mathbf{b}\cdot\nabla)\,b_x + \eta\frac{\partial}{\partial x}\left(\frac{|\mathbf{b}|^2}{2}\right) + (\mathbf{v}\cdot\mathbf{b})\,b_x \right] dz \tag{1.39}$$

$$\Phi_1 = \int_{x=1} \left[\left(\frac{1}{2}\rho|\mathbf{v}|^2 + \gamma u \right) v_x + \eta \left((\mathbf{b}\cdot\nabla)\, b_x - \frac{\partial}{\partial x}\left(\frac{|\mathbf{b}|^2}{2} \right) \right) + |\mathbf{b}|^2 v_x - (\mathbf{v}\cdot\mathbf{b})\, b_x + \nu \left(2v_x \frac{\partial v_x}{\partial x} + v_y \frac{\partial v_x}{\partial y} + v_z \frac{\partial v_x}{\partial z} + v_x \frac{\partial v_y}{\partial y} + v_x \frac{\partial v_z}{\partial z} \right) \right] dz \quad (1.40)$$

.

1.3 The method of projected characteristics

The method of characteristics can be used to build boundary conditions that are consistent with the hyperbolic structure of fluid or MHD equations. It is based on the decomposition of solutions of the Equations (1.27)-(1.30) into characteristic modes that cross the domain boundary propagating from inside to outside, or the reverse. We employed a version of the method that has been formulated by Sun et al. (1995) and was used to simulate the entrance and exit of Alfvénic perturbations both in a large-scale coronal model (Grappin et al., 2000) and in an equilibrium structure with an X-point (Landi et al., 2005). In these cases the entrance of Alfvén waves was obtained by imposing the amplitude of incoming perturbations at the boundary. In the present case we follow a different approach, i.e., the input of perturbations is obtained by imposing a time-dependent velocity field on the lower boundary $x = 0$. We use the method of projected characteristics to deduce the time evolution of the other physical quantities (density, pressure, and magnetic field) at the same boundary in a way that is consistent with the MHD equations. At the upper boundary $x = 1$, the method is used to simulate the free exit of perturbations by imposing that no perturbation enters the domain through that boundary (Grappin et al., 2000; Landi et al., 2005).

We write the compressible, non-ideal, MHD Equations (1.27)-(1.30) sep-

arating the terms containing first-order derivatives with respect to x from the other terms:

$$\frac{\partial U_i}{\partial \tau} + A_{ij}\frac{\partial U_j}{\partial x} + T_i = 0 \ , \quad i = 1, ..., 7 \tag{1.41}$$

where $\mathbf{U}^t = (\rho, v_x, v_y, v_z, b_y, b_z, p)$ and the vector $\mathbf{T}$ contain all the terms with derivatives with respect to y and z and the non-ideal terms. Hereafter, summation over dummy indices is understood. We eliminated the equation for b_x in the system (1.41) because we calculate its value at the boundaries $x = 0$ and $x = 1$ by using the divergence free condition. The matrix A has the following form:

$$A = \begin{pmatrix} v_x & \rho & 0 & 0 & 0 & 0 & 0 \\ 0 & v_x & 0 & 0 & \frac{b_y}{\rho} & \frac{b_z}{\rho} & \frac{1}{\rho} \\ 0 & 0 & v_x & 0 & -\frac{b_x}{\rho} & 0 & 0 \\ 0 & 0 & 0 & v_x & 0 & -\frac{b_x}{\rho} & 0 \\ 0 & b_y & -b_x & 0 & v_x & 0 & 0 \\ 0 & b_z & 0 & -b_x & 0 & v_x & 0 \\ 0 & \gamma p & 0 & 0 & 0 & 0 & v_x \end{pmatrix}$$

The eigenvalues of the matrix A are: $\lambda^{(1)} = v_x$, $\lambda^{(2)} = v_x + c_{ax}$, $\lambda^{(3)} = v_x + c_f$, $\lambda^{(4)} = v_x + c_s$, $\lambda^{(5)} = v_x - c_{ax}$, $\lambda^{(6)} = v_x - c_f$, $\lambda^{(7)} = v_x - c_s$, where $c_{ax} = b_x/\sqrt{\rho}$ is the Alfvén speed along the x-direction,

$$c_f = 1/\sqrt{2}\left(\sqrt{(c_a{}^2 + a^2) + 1/2\sqrt{(c_a{}^2 + a^2) - 4c_{ax}{}^2 a^2}}\right)$$

and

$$c_s = 1/\sqrt{2}\left(\sqrt{(c_a{}^2 + a^2) - 1/2\sqrt{(c_a{}^2 + a^2) - 4c_{ax}{}^2 a^2}}\right)$$

are the fast and slow magnetosonic speeds, with $a^2 = \sqrt{\gamma P/\rho}$ and ${c_a}^2 = b^2/\rho$. The eigenvalues $\lambda^{(k)}$ represent the propagation velocities of the seven different waves (Alfvén, fast and slow magnetosonic, and entropy waves) crossing the boundary in both senses. For each of the two boundaries we distinguish between *incoming perturbations* (corresponding to positive $\lambda^{(k)}$ at $x = 0$, or negative $\lambda^{(k)}$ at $x = 1$) and *outgoing perturbations* (corresponding to negative $\lambda^{(k)}$ at $x = 0$, or positive $\lambda^{(k)}$ at $x = 1$).

We indicate by $\xi^{(k)}$ and $\eta^{(k)}$ the right and left eigenvector of the matrix A corresponding to the k-th eigenvalue $\lambda^{(k)}$:

$$A_{ij}{\xi_j}^{(k)} = \lambda^{(k)}{\xi_i}^{(k)} \qquad {\eta_i}^{(k)}A_{ij} = \lambda^{(k)}{\eta_j}^{(k)}{}^{1} \qquad k = 1, \ldots, 7 \tag{1.42}$$

A right (left) eigenvector and a left (right) eigenvector corresponding to different eigenvalues are mutually orthogonal. Moreover, we choose to normalize eigenvectors so that:

$${\xi_i}^{(k)}{\eta_i}^{(l)} = \delta_{kl} \tag{1.43}$$

In the following we illustrate the procedure in the most general case, in which all magnetic field components are non vanishing at the given grid point on the boundary. The two particular cases in which $b_x = 0$ or $b_\perp = \left(b_y^2 + b_z^2\right)^{1/2} = 0$ have been treated in a similar way. The explicit expressions of left eigenvectors are:

$$\eta^{(1)} = \left(\frac{1}{\rho}, 0, 0, 0, 0, 0, -\frac{1}{\gamma p}\right) \tag{1.44}$$

$$\eta^{(2)} = \left(0, 0, -\sigma\frac{\sqrt{\rho}b_z}{2b_\perp^2}, \sigma\frac{\sqrt{\rho}b_y}{2b_\perp^2}, \frac{b_z}{2b_\perp^2}, -\frac{b_y}{2b_\perp^2}, 0\right) \tag{1.45}$$

[1] No summation is to be intended over the upper index in parenthesis (k)

$$\eta^{(3)} = \left(0, \frac{1}{2\gamma_f c_f}, -\frac{b_y}{2b_x\alpha_f\gamma_f c_f}, -\frac{b_z}{2b_x\alpha_f\gamma_f c_f}, \frac{b_y}{2b_x^2\alpha_f\gamma_f}, \frac{b_z}{2b_x^2\alpha_f\gamma_f}, \frac{1}{2\rho\gamma_f c_f^2}\right) \tag{1.46}$$

$$\eta^{(4)} = \left(0, \frac{1}{2\gamma_s c_s}, -\frac{b_y}{2b_x\alpha_s\gamma_s c_s}, -\frac{b_z}{2b_x\alpha_s\gamma_s c_s}, \frac{b_y}{2b_x^2\alpha_s\gamma_s}, \frac{b_z}{2b_x^2\alpha_s\gamma_s}, \frac{1}{2\rho\gamma_s c_s^2}\right) \tag{1.47}$$

$$\eta^{(5)} = \left(0, 0, \sigma\frac{\sqrt{\rho}b_z}{2b_\perp^2}, -\sigma\frac{\sqrt{\rho}b_y}{2b_\perp^2}, \frac{b_z}{2b_\perp^2}, -\frac{b_y}{2b_\perp^2}, 0\right) \tag{1.48}$$

$$\eta^{(6)} = \left(0, -\frac{1}{2\gamma_f c_f}, \frac{b_y}{2b_x\alpha_f\gamma_f c_f}, \frac{b_z}{2b_x\alpha_f\gamma_f c_f}, \frac{b_y}{2b_x^2\alpha_f\gamma_f}, \frac{b_z}{2b_x^2\alpha_f\gamma_f}, \frac{1}{2\rho\gamma_f c_f^2}\right) \tag{1.49}$$

$$\eta^{(7)} = \left(0, -\frac{1}{2\gamma_s c_s}, \frac{b_y}{2b_x\alpha_s\gamma_s c_s}, \frac{b_z}{2b_x\alpha_s\gamma_s c_s}, \frac{b_y}{2b_x^2\alpha_s\gamma_s}, \frac{b_z}{2b_x^2\alpha_s\gamma_s}, \frac{1}{2\rho\gamma_s c_s^2}\right) \tag{1.50}$$

while the right eigenvectors are:

$$\xi^{(1)} = (\rho, 0, 0, 0, 0, 0, 0) \tag{1.51}$$

$$\xi^{(2)} = \left(0, 0, -\sigma\frac{b_z}{\sqrt{\rho}}, \sigma\frac{b_y}{\sqrt{\rho}}, b_z, -b_y, 0\right) \tag{1.52}$$

$$\xi^{(3)} = \left(\rho\frac{c_{ax}^2}{c_f^2}\alpha_f, c_f\frac{c_{ax}^2}{c_f^2}\alpha_f, -\frac{b_x b_y}{\rho c_f}, -\frac{b_x b_z}{\rho c_f}, b_y, b_z, \frac{c_{ax}^2}{c_f^2}\gamma p\alpha_f\right) \tag{1.53}$$

$$\xi^{(4)} = \left(\rho\frac{c_{ax}^2}{c_s^2}\alpha_s, c_s\frac{c_{ax}^2}{c_s^2}\alpha_s, -\frac{b_x b_y}{\rho c_s}, -\frac{b_x b_z}{\rho c_s}, b_y, b_z, \frac{c_{ax}^2}{c_s^2}\gamma p\alpha_s\right) \tag{1.54}$$

$$\xi^{(5)} = \left(0, 0, \sigma\frac{b_z}{\sqrt{\rho}}, -\sigma\frac{b_y}{\sqrt{\rho}}, b_z, -b_y, 0\right) \tag{1.55}$$

$$\xi^{(6)} = \left(\rho\frac{c_{ax}^2}{c_f^2}\alpha_f, -c_f\frac{c_{ax}^2}{c_f^2}\alpha_f, \frac{b_x b_y}{\rho c_f}, \frac{b_x b_z}{\rho c_f}, b_y, b_z, \frac{c_{ax}^2}{c_f^2}\gamma p\alpha_f\right) \tag{1.56}$$

$$\xi^{(7)} = \left(\rho\frac{c_{ax}^2}{c_s^2}\alpha_s, -c_s\frac{c_{ax}^2}{c_s^2}\alpha_s, \frac{b_x b_y}{\rho c_s}, \frac{b_x b_z}{\rho c_s}, b_y, b_z, \frac{c_{ax}^2}{c_s^2}\gamma p\alpha_s\right) \tag{1.57}$$

The symbols used in the above expressions are defined as

$$b_\perp = \sqrt{b_y^2 + b_z^2},\ \alpha_f = \left(\frac{c_f^2}{c_{ax}^2} - 1\right),\ \gamma_f = \left(1 - \frac{c_{ax}^2 a^2}{c_f^4}\right)$$

$$\sigma = \frac{b_x}{|b_x|},\ \alpha_s = \left(\frac{c_s^2}{c_{ax}^2} - 1\right),\ \gamma_s = \left(1 - \frac{c_{ax}^2 a^2}{c_s^4}\right)$$

The right eigenvectors (1.51)-(1.57) (as the left eigenvectors) are linearly independent, so they form a complete set of vectors in a seven dimensional space. This allows us to write the second term in the MHD Equations (1.41) as a linear combination of the ${\xi_i}^{(k)}$:

$$A_{ij}\frac{\partial U_j}{\partial x} = \sum_k L^{(k)} {\xi_i}^{(k)} \tag{1.58}$$

The left-hand side of Equation (1.58) contains the advective terms representing the propagation of perturbations in the x-direction (i.e., across the boundary). In this equation the contribution of the different modes to the propagation is singled out as the coefficients $L^{(k)}$ representing the weight of each mode. Using expression (1.58), we re-write the Equation (1.41) in the form

$$\frac{\partial U_i}{\partial \tau} = -\sum\nolimits_k L^{(k)} {\xi_i}^{(k)} - T_i \tag{1.59}$$

where the time derivatives of the fields U_i are expressed in terms of the coefficients $L^{(k)}$. Multiplying Equation (1.59) by $\eta_i^{(k)}$ and using the condition (1.43) we obtain the projected Equation

$$L^{(k)} = -{\eta_i}^{(k)}\frac{\partial U_i}{\partial \tau} - {\eta_i}^{(k)} T_i \tag{1.60}$$

in which the coefficients $L^{(k)}$ are expressed as functions of the time deriva-

tives $\partial U_i/\partial\tau$. Finally, another expression for $L^{(k)}$ is obtained by multiplying Equation (1.58) by $\eta_i^{(k)}$:

$$L^{(k)} = \lambda^{(k)}\eta_i{}^{(k)}\frac{\partial U_i}{\partial x} \tag{1.61}$$

where we used Equation (1.42) and the condition (1.43). In Equation (1.61) the coefficients $L^{(k)}$ are expressed in terms of the normal derivatives of the fields. Boundary conditions are determined using Equations (1.59)-(1.61) evaluated at the boundaries. In particular, Equation (1.59) allows us calculate the time evolution of the fields U_i at the boundaries once the coefficients $L^{(k)}$ have been determined.

Concerning the determination of $L^{(k)}$, we observe that boundary conditions can influence only incoming perturbations, whereas outgoing perturbations are entirely determined by the field configuration inside the domain. Therefore, the number of boundary conditions we can impose is equal to number of incoming modes. The first step of the procedure consists of calculating the sign of each eigenvalue $\lambda^{(k)}$ at the given gridpoint on the boundary, in order to distinguish between the $L^{(k)}$ corresponding to incoming perturbations and those corresponding to outgoing perturbations. Since the former coefficients are determined by boundary conditions, we must distinguish between the lower and the upper boundary.

1.3.1 Lower Boundary

On the lower boundary $x = 0$ we impose the value of the three components of the velocity field. In particular, we choose $v_x(x = 0, z, \tau) = 0$. In that case we have only three positive eigenvalues ($\lambda^{(2)}$, $\lambda^{(3)}$, and $\lambda^{(4)}$) corresponding to incoming Alfvén, fast and slow magnetosonic perturbations, three nega-

tive eigenvalues ($\lambda^{(5)}$, $\lambda^{(6)}$, and $\lambda^{(7)}$), while $\lambda^{(1)} = 0$. Since $\lambda^{(1)} = 0$ we can look at the entropy mode as an outgoing mode with null speed. The coefficients $L^{(1)}$, $L^{(5)}$, $L^{(6)}$, and $L^{(7)}$ corresponding to outgoing perturbations are calculated using Equation (1.61). The explicit expressions are the following:

$$L^{(1)} = 0 \tag{1.62}$$

$$L^{(5)} = -\sigma \frac{b_x}{\sqrt{\rho}} \left[\sigma \frac{\sqrt{\rho} b_z}{2{b_\perp}^2} \left(\frac{\partial v_y}{\partial x} \right)_+ - \sigma \frac{\sqrt{\rho} b_y}{2{b_\perp}^2} \left(\frac{\partial v_z}{\partial x} \right)_+ + \frac{b_z}{2{b_\perp}^2} \left(\frac{\partial b_y}{\partial x} \right)_+ - \frac{b_y}{2{b_\perp}^2} \left(\frac{\partial b_z}{\partial x} \right)_+ \right] \tag{1.63}$$

$$L^{(6)} = -c_f \left[-\frac{1}{2\gamma_f c_f} \left(\frac{\partial v_x}{\partial x} \right)_+ + \frac{b_y}{2b_x \alpha_f \gamma_f c_f} \left(\frac{\partial v_y}{\partial x} \right)_+ + \frac{b_z}{2b_x \alpha_f \gamma_f c_f} \left(\frac{\partial v_z}{\partial x} \right)_+ + \frac{b_y}{2{b_x}^2 \alpha_f \gamma_f} \left(\frac{\partial b_y}{\partial x} \right)_+ + \frac{b_z}{2{b_x}^2 \alpha_f \gamma_f} \left(\frac{\partial b_z}{\partial x} \right)_+ + \frac{1}{2\rho \gamma_f {c_f}^2} \left(\frac{\partial p}{\partial x} \right)_+ \right] \tag{1.64}$$

$$L^{(7)} = -c_s \left[-\frac{1}{2\gamma_s c_s} \left(\frac{\partial v_x}{\partial x} \right)_+ + \frac{b_y}{2b_x \alpha_s \gamma_s c_s} \left(\frac{\partial v_y}{\partial x} \right)_+ + \frac{b_z}{2b_x \alpha_s \gamma_s c_s} \left(\frac{\partial v_z}{\partial x} \right)_+ + \frac{b_y}{2{b_x}^2 \alpha_s \gamma_s} \left(\frac{\partial b_y}{\partial x} \right)_+ + \frac{b_z}{2{b_x}^2 \alpha_s \gamma_s} \left(\frac{\partial b_z}{\partial x} \right)_+ + \frac{1}{2\rho \gamma_s {c_s}^2} \left(\frac{\partial p}{\partial x} \right)_+ \right] \tag{1.65}$$

In these equations the lower symbol "+" indicates right x-derivatives, which are calculated using boundary and internal gridpoints by a forward finite difference method. Thus, the internal configuration determines the coefficients

$L^{(5)}$, $L^{(6)}$, and $L^{(7)}$ through these derivatives. The coefficients $L^{(2)}$, $L^{(3)}$, and $L^{(4)}$, corresponding to incoming perturbations, are determined by the velocity field imposed at the boundary by means of Equations (1.59)-(1.60), with $i = 2, 3, 4$, where $L^{(2)}$, $L^{(3)}$, and $L^{(4)}$ are treated as unknown. Solving these three equations, we find the explicit expressions for $L^{(2)}$, $L^{(3)}$, and $L^{(4)}$:

$$L^{(2)} = \frac{\sigma\sqrt{\rho}b_z}{{b_\perp}^2}\left(\frac{\partial v_y}{\partial \tau} + T_3\right) - \frac{\sigma\sqrt{\rho}b_y}{{b_\perp}^2}\left(\frac{\partial v_z}{\partial \tau} + T_4\right) + L^{(5)} \tag{1.66}$$

$$L^{(3)} = -\frac{1}{\gamma_f c_f}T_2 + \frac{b_y}{b_x\alpha_f\gamma_f c_f}\left(\frac{\partial v_y}{\partial \tau} + T_3\right) + \frac{b_z}{b_x\alpha_f\gamma_f c_f}\left(\frac{\partial v_z}{\partial \tau} + T_4\right) + L^{(6)} \tag{1.67}$$

$$L^{(4)} = -\frac{1}{\gamma_s c_s}T_2 + \frac{b_y}{b_x\alpha_s\gamma_s c_s}\left(\frac{\partial v_y}{\partial \tau} + T_3\right) + \frac{b_z}{b_x\alpha_s\gamma_s c_s}\left(\frac{\partial v_z}{\partial \tau} + T_4\right) + L^{(7)} \tag{1.68}$$

The quantities in the right-hand side of Equations (1.66)-(1.68) (velocity component time derivatives $\partial v_y/\partial\tau$, $\partial v_z/\partial\tau$; outgoing perturbation coefficients $L^{(5)}$, $L^{(6)}$, and $L^{(7)}$; and the quantities T_2, T_3, and T_4) are determined by the velocity field imposed at the boundary or by the configuration of fields in the interior of the domain. Thus, equations (1.66)-(1.68) represent the compatibility conditions. Finally, the coefficients $L^{(k)}$ calculated by Equations (1.62)-(1.68) at a given time are used in Equation (1.59) with $i = 1, 5, 6, 7$ to calculate the time advance of ρ, b_y, b_z, and p at the boundary $x = 0$.

1.3.2 Upper Boundary

The upper boundary $x = 1$ represents an open boundary that can be freely crossed by matter and/or outgoing perturbations. No velocity field is imposed on that boundary. Instead, boundary conditions correspond to the

requirement that no incoming perturbations cross that boundary. In this case, since v_x can have any sign, the number of incoming or outgoing waves on a given gridpoint cannot be determined a priori. As for the lower boundary, coefficients $L^{(k)}$ corresponding to outgoing perturbations are determined by Equation (1.61) that we write in the form

$$L^{(k)}_{\text{out}} = \lambda^{(k)} \eta_i{}^{(k)} \left(\frac{\partial U_i}{\partial x} \right)_- , \quad \text{for } (k) \text{ such that } \lambda^{(k)} \geq 0 \tag{1.69}$$

The lower symbol "-" indicates left x-derivatives which are calculated using boundary and internal gridpoints by a backward finite difference method. Coefficients $L^{(k)}$ corresponding to incoming perturbations are calculated using the projected MHD Equation (1.60). In this equation we set

$$\eta_i^{(k)} \frac{\partial U_i}{\partial \tau} = 0 \ , \quad \text{for } (k) \text{ such that } \lambda^{(k)} < 0 \tag{1.70}$$

where only values of the index (k) corresponding to a negative eigenvalue $\lambda^{(k)}$ are considered. Equation (1.70) represents the boundary conditions and corresponds to the requirement that incoming perturbations alone do not generate any time evolution of the fields U_i. Note that the number of boundary conditions (1.70) is equal to the number of incoming perturbations at the given gridpoint. Using Equation (1.70) into Equation (1.60) we get the expression for the coefficients $L^{(k)}$ corresponding to incoming perturbations:

$$L^{(k)}_{\text{in}} = -\eta_i^{(k)} T_i \ , \quad \text{for } (k) \text{ such that } \lambda^{(k)} < 0 \tag{1.71}$$

Finally, by inserting the coefficients $L^{(k)}$ (Equations (1.69) and (1.71) into the Equation (1.59), the time advance of all the fields U_i at the boundary $x = 1$ is calculated.

As claimed by Poinsot & Lele (1993), who applied this method for a fluid case in order to guarantee stability and/or well-posedness it is necessary to add further boundary conditions. In our case, we impose that some diffusive terms in Equations (1.27)-(1.30) ($\kappa[\partial^2(p/\rho)/\partial x^2]$, $\eta\,\nabla^2 b_y$, $\eta\,\nabla^2 b_z$) are vanishing at $x = 0$ and $x = 1$.

1.4 Numerical results

In the following we describe the results obtained in numerical simulations. We first consider the case of the Alfvénic perturbation.

1.4.1 Alfvénic Perturbation

In this case the velocity component directed perpendicularly to the plane of the simulation v_y is directly excited by boundary conditions at the lower boundary. Magnetic lines are locally bent in the y-direction and a non-vanishing b_y magnetic field component is generated at $x = 0$. The y-components of the velocity and magnetic field represent the main Alfvénic wave component of the fluctuation generated at the lower boundary. Such a wave propagates inside the domain following magnetic lines. In Figure 1.2

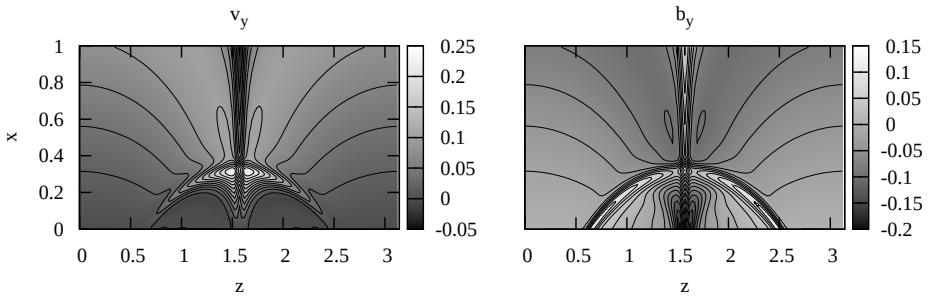

Figure 1.2: Components v_y and b_y at time $\tau = 10$ in the case of Alfvénic perturbations, with isolines.

the velocity v_y and magnetic field b_y components are plotted at the time $\tau = 10$. At that time, the perturbation continuously produced at $x = 0$ has filled the whole spatial domain. We can discriminate two different behaviors of fluctuations in open or closed fieldline regions. In the former regions, fluctuations cross the domain in the upward direction and eventually exit from the top. We verified that no significant reflection takes place at the upper boundary; this shows that an open boundary is well reproduced by the method of characteristics. Open fieldline regions are separated in the lower part of the domain, but they come in contact in the upper part through the vertical separatrix which is above the X-point (see Figure 1.1); thus, upward-propagating waves completely fill the upper part of the domain. In this region v_y and b_y appear to be anticorrelated (Figure 1.2), as required for Alfvén waves propagating in the direction of the background magnetic field. Since the Alfvén speed is not uniform, the wave propagates faster at the flanks than in the middle of the domain, thus producing phase-mixing (Heyvaerts & Priest, 1983). This can be seen in Figure 1.2, where wavefronts (indicated by the isolines of v_y and b_y), which are nearly horizontal in the lower domain, approach one another and become nearly vertical in the upper central part. This effect increases the wavevector component perpendicular to the background magnetic field; $\mathbf{b}^{(0)}$ is nearly vertical at large x, so small scales in the horizontal z-direction are produced in the upper part of the domain. This effect is more significant around the vertical separatrix, because fluctuations traveling in this region have passed near the X-point, where the Alfvén velocity vanishes. As a result, small scales in the upper part of the domain are concentrated in the central region around the separatrix.

In closed fieldline regions the perturbation generated at the lower boundary remains confined beneath the separatrices and cannot propagate higher.

In this region waves coming from different parts of the lower boundary propagate along magnetic lines in opposite directions. In these waves v_y and b_y can be either positively correlated or anticorrelated, according to the sense of propagation. As a consequence, no particular correlation between v_y and b_y is observed in the closed fieldline regions, where these two kinds of waves are superposed (Figure 1.2). However, all waves propagating close to the curved separatrices pass close to the X-point where the Alfvén velocity vanishes and undergo an intense phase-mixing. Then, small scales form around the separatrices that are also in closed fieldline regions. This phenomenon had been previously reported by McLaughlin et al. (2010).

The formation of small scales can be visualized by plotting the spatial distribution of the heat-source terms P_η and P_ν due to resistive and viscous dissipation, as defined in Equation (1.34). In fact, dissipation becomes stronger at locations where small scales are present. In Figure 1.3 $P_\eta(x, z, \tau)$

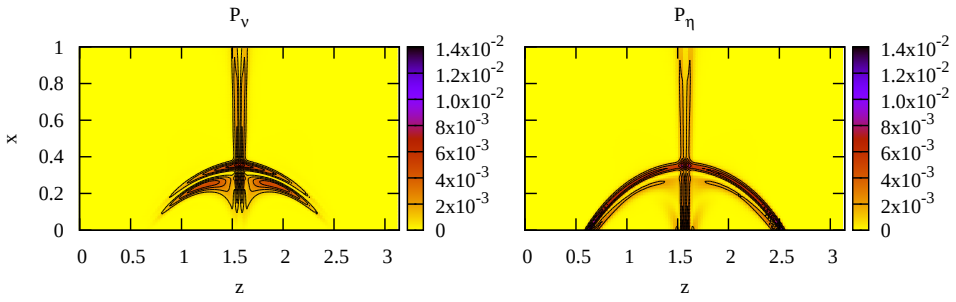

Figure 1.3: Dissipated power per unit volume due to viscosity P_ν (left panel) and resistivity P_η (right panel) in the xz plane at the time $\tau = 10$ for the Alfvénic perturbation.

and $P_\nu(x, z, \tau)$ are plotted at the time $\tau = 10$. As expected, most of the dissipated power is concentrated around the four separatrices. Around the upper separatrix we found that $P_\eta \simeq P_\nu$, which is a consequence of the velocity-magnetic field correlation ($v_y \simeq -b_y$) found in that region along

with the choice that viscosity ν and resistivity η are equal. On the contrary, around the other separatrices v_y and b_y are no longer correlated, so P_η and P_ν can be different. In particular, we found that P_η is slightly larger than P_ν.

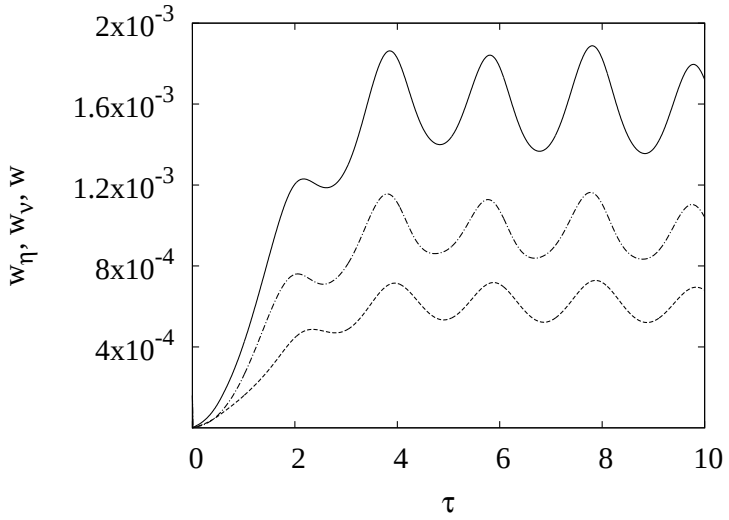

Figure 1.4: Integrated dissipated power due to viscosity w_ν (dashed line), to resistivity w_η (dash-dotted line), and total w (solid line), plotted as functions of time for the Alfvénic perturbation.

To obtain a quantitative evaluation of the dissipated power, we calculated the integrated dissipated power $w_\eta(\tau)$, $w_\nu(\tau)$ defined in Equation (1.35), and their sum $w(\tau) = w_\eta(\tau) + w_\nu(\tau)$. These quantities are plotted in Figure 1.4 as functions of time τ. The dissipated power is initially null and grows until the time $\tau \sim 3$, when it reaches a quasi-stationary state where it oscillates around a mean value $\langle w \rangle \simeq 0.0017$. Comparing this value with the mean input energy flux $\langle \Phi_0 \rangle$ calculated at the lower boundary $x = 0$, we found that $\langle w \rangle / \langle \Phi_0 \rangle \sim 0.15$ for $\nu = \eta = 10^{-2}$ whereas $\langle w \rangle / \langle \Phi_0 \rangle \sim 0.1$ for $\nu = \eta = 10^{-3}$. Then, for the considered values of the dissipative coefficient, about 10% of the power that enters the domain in

form of Alfvén waves is dissipated inside the domain (i.e., at very low levels in the corona). However, the above results do not allow us to obtain an evaluation of the ratio $\langle w \rangle / \langle \Phi_0 \rangle$ for more realistic values of dissipative coefficient, which are much lower in the coronal plasma than the values we used in the simulation. Comparing resistive and viscous dissipated power, we see that $w_\eta(\tau) > w_\nu(\tau)$ (i.e., more magnetic energy is dissipated than kinetic energy). Within the linear approximation we can assume that velocity and magnetic field perturbations are polarized along the y-direction. Since the equilibrium magnetic field $\mathbf{b}^{(0)}$ is a current-free field, dissipated powers in the region around separatrices dissipated powers can be estimated by

$$P_\eta \simeq \eta \left(\nabla b_y\right)^2 \sim \eta \frac{(\delta b_y)^2}{\ell^2} \quad , \quad P_\nu \simeq \nu \left(\nabla v_y\right)^2 \sim \nu \frac{(\delta v_y)^2}{\ell^2} \tag{1.72}$$

where ℓ is the dissipative scale and δb_y and δv_y are local amplitudes of magnetic field and velocity fluctuations, respectively. Around the upper separatrix only upward-propagating waves are present with $\delta b_y \simeq \delta v_y$. In contrast, around the lower separatrices where waves propagate in both senses, we observe that $\delta b_y > \delta v_y$. Thus, the slight unbalance between $w_\eta(\tau)$ and $w_\nu(\tau)$ could be due to lack of fluctuating magnetic and kinetic energy equipartition in the region of closed magnetic fieldlines.

In order to illustrate the presence of small scales in the fluctuations leaving the domain from the upper boundary, we calculated the spectrum of the velocity component v_y. As explained previously, we expect that small scales formation due to phase-mixing takes place only in the direction perpendicular to $\mathbf{b}^{(0)}$ (i.e., mainly in the horizontal direction). Thus, we calculated a 1D spectrum giving the energy distribution at the various scales in the z-direction. The velocity y-component calculated at the upper boundary

$x = 1$ is expanded in the Fourier series

$$v_y(1, z, \tau) = \sum_{k_z} \hat{v}_y(k_z, \tau) e^{ik_z z} \tag{1.73}$$

The time-dependent spectrum is given by $|\hat{v}_y(k_z, \tau)|^2$. We found that the shape of such a spectrum varies quasi-periodically in time according to the instantaneous value of the wave phase. For this reason it is suitable to consider a spectrum averaged in time over a wave period $T = 2\pi/\omega$:

$$e_{v_y}(k_z) = \frac{1}{T} \int_T |\hat{v}_y(k_z, \tau)|^2 d\tau. \tag{1.74}$$

The time-averaged velocity spectrum is plotted in Figure 1.5 in logarithmic

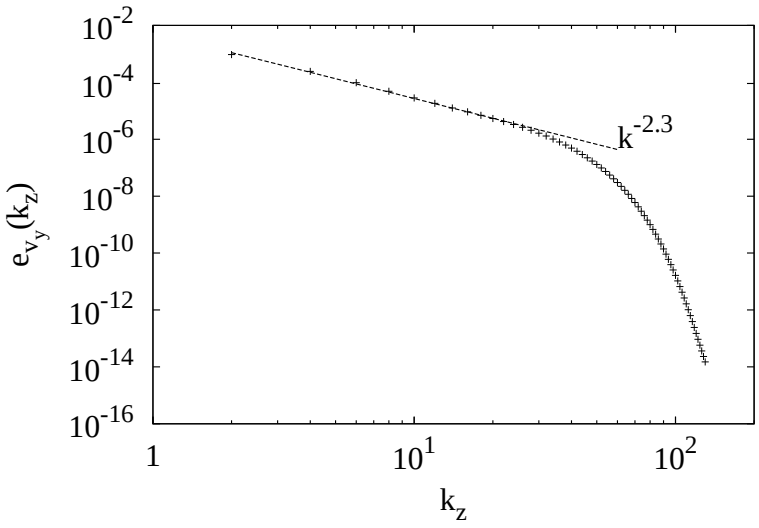

Figure 1.5: Time-averaged velocity y-component spectrum $e_{v_y}(k_z)$ calculated at $x = 1$ for the Alfvénic perturbation (crosses), and a power-law function that fits the spectrum in the low-wavenumber range (dashed line) are plotted in logarithmic scale.

scale. It can be seen that $e_{v_y}(k_z)$ follows a power law remarkably well, up to wavevectors $k_z \sim 30$. For larger wavevectors the spectrum becomes

curved, which is probably due to dissipation. In the power-law range, the spectrum is well fitted by a law $\propto {k_z}^{-2.3}$. A very similar spectrum has also been found for the magnetic fluctuation b_y. Thus, the effect of the inhomogeneous magnetic field $\mathbf{b}^{(0)}$ where the Alfvénic fluctuation propagates is to create a power-law spectrum in the initially uniform perturbation. We point out that the power-law spectrum we found is steeper than the Kolmogorov spectrum. We note that the same result, with a similar value for the spectral slope, has also been found by Malara (2013) in a model based on the WKB approximation, in which small-wavelength Alfvén waves propagate along magnetic lines at the local Alfvén speed. McLaughlin et al. (2010) showed that a small-amplitude Alfvén wave in a 2D equilibrium magnetic field with a uniform density follows magnetic lines with the local Alfvén speed, regardless of its wavelength. Thus, the formation in our simulation of a spectrum similar to that found in the WKB limit was expected.

The wave amplitude is small with respect to the background magnetic field, being $b_y/b^{(0)} \sim 0.1$. Thus, it could be expected that nonlinear effects depending on the square of the wave amplitude, such as the generation of compressive fluctuations, should be negligible when compared with the Alfvénic fluctuation. However, magnetic pressure gradients could locally be large enough to drive significant compressible fluctuations. This happens around separatrices, because of the presence of small-scale structures in the wave profile. The Laplace force associated with the total magnetic field $\mathbf{b} = [\mathbf{b}^{(0)} + b_y \mathbf{e}_y]$ is $\mathbf{f} = (\nabla \times \mathbf{b}) \times \mathbf{b}$. Taking into account the condition $\nabla \times \mathbf{b}^{(0)} = 0$, $\mathbf{f}$ has the form

$$\mathbf{f} = -\frac{\partial}{\partial x}\left(\frac{b_y^2}{2}\right)\mathbf{e}_x + \left(b_x^{(0)}\frac{\partial b_y}{\partial x} + b_z^{(0)}\frac{\partial b_y}{\partial z}\right)\mathbf{e}_y - \frac{\partial}{\partial z}\left(\frac{b_y^2}{2}\right)\mathbf{e}_z \qquad (1.75)$$

Thus, the components of $\mathbf{f}$ in the xz-plane are opposite to the magnetic pressure gradient associated with the perturbation field b_y. These components can reach significant values at locations where small scales form (i.e., around the separatrices). In Figure 1.6 the magnetic pressure $p_M = b_y^2/2$ due to the

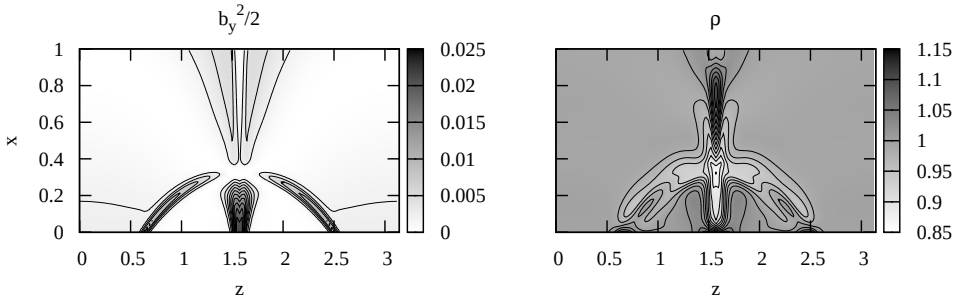

Figure 1.6: Magnetic pressure p_M associated with the Alfvénic perturbation (left panel) and density ρ (right panel) calculated at the time $\tau = 8.5$

perturbation of the magnetic field component b_y, and the density ρ are plotted at time $\tau = 8.5$ in the left and right panels, respectively. We observe an increase of magnetic pressure on both sides of the vertical separatrix above the X-point, with lower values of p_M in between. This is due to the accumulation of wavefronts of the Alfvén wave caused by phase-mixing. This results in strong localized gradients of p_M that push the fluid toward the separatrix from both sides. The result is the formation of a dense, vertically elongated "bubble" localized on the separatrix, where the density reaches values up to $\sim 10 - 15\%$ larger than the unperturbed value. This compressive structure can be seen in the right panel of Figure 1.6. The compressive perturbation evolves in time propagating upward, pushed by the magnetic pressure of the Alfvén wave. This time evolution is represented in Figure 1.7, where the density profile is plotted as a function of x along the separatrix at $z = \pi/2$ for different times. At the time $\tau = 8$ a maximum of density, where ρ reaches

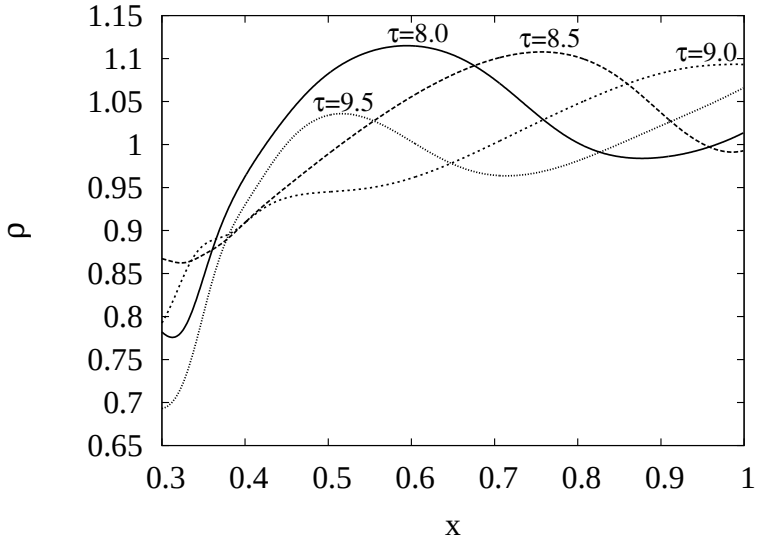

Figure 1.7: Density profiles as functions of x along the vertical separatrix $z = \pi/2$ at different times.

the value $\simeq 1.12$ is located above the X-point, at $x \simeq 0.59$. This fluctuation propagates upward with a speed $\sim 0.3 - 0.4$ (in dimensionless units), which increases with increasing x, whereas the fluctuation amplitude slightly decreases. The Alfvén velocity on the separatrix at $x = 1$ is $c_A \simeq 0.26$, even if it increases on the two sides of the separatrix. Eventually, the density perturbation exits the domain through the boundary $x = 1$, while a new compression forms above the X-point (time $\tau = 9.5$). We verified that the period of the compressive fluctuations is ~ 2, which is $1/2$ the period of the Alfvénic perturbation. Summarizing, in the vicinity of the separatrix nonlinear effects generate density fluctuations with an amplitude $\delta\rho/\rho$ of the same order as the amplitude of the Alfvén wave. Such fluctuations are driven by the Alfvén wave magnetic pressure gradient and propagate along the magnetic field at a speed comparable with the Alfvén velocity.

1.4.2 Magnetosonic Perturbation

In this case a velocity perturbation polarized in the z-direction is imposed at the lower boundary. This motion locally distorts the equilibrium field magnetic lines, generating a perturbation of both x and z magnetic field components. At variance with the previous case, no perturbation y components is generated. Then, the perturbation produced at the boundary belongs to the magnetosonic mode. We shall see that the behaviour of the system is different from the previous case, with a more important role played by the X-point.

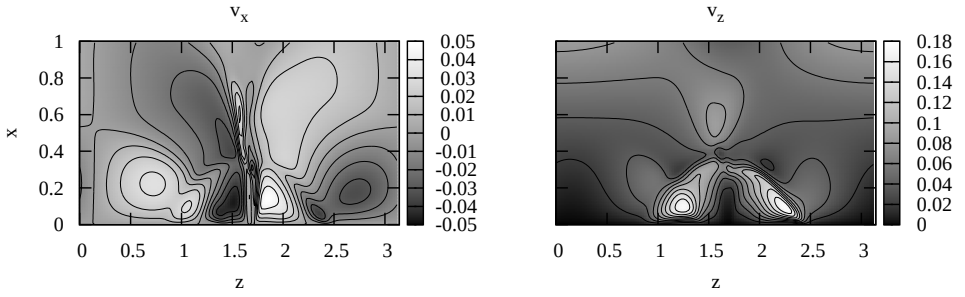

Figure 1.8: Velocity components v_x and v_z at time $\tau = 2$ for the magnetosonic perturbation.

In Figure 1.8 the velocity components v_y and v_z are plotted at the time $\tau = 2$. It can be seen that the distribution of the velocity field is no longer symmetric. Moreover, the spatial distribution of $\mathbf{v}$ is smoother and more isotropic than in the Alfvénic case. No small scales appear to be present in the upper part of the domain (i.e. in the region where the perturbation leaves the domain). We then calculated the time-averaged spectra of the x and z components of the velocity and magnetic field. In the same way as the Alfvénic perturbation case, these spectra are calculated using the profiles of the above quantities taken along the upper boundary $x = 1$. The

averaged spectra e_{v_x}, e_{v_z}, e_{b_x} and e_{b_z}, are plotted in Figure 1.9. All such

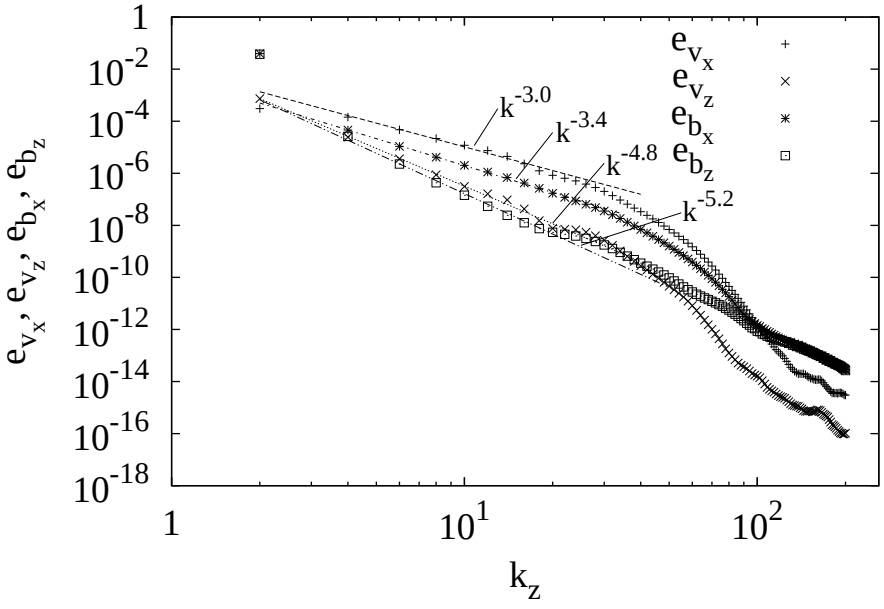

Figure 1.9: Velocity $e_{v_x}(k_z)$ (crosses), $e_{v_z}(k_z)$ ("x" symbols) and magnetic field $e_{b_x}(k_z)$ (stars), $e_{b_z}(k_z)$ (squares). Time-averaged spectra calculated at $x = 1$ are plotted with power laws fits (lines).

spectra are much steeper than those found for the Alfvénic perturbation. We can conclude that no relevant small scales are present in the magnetosonic perturbations that leave the domain through the upper boundary.

Indeed, small scales are present in the domain, but only in a limited region around the X-point. This confirms a finding by McLaughlin et al. (2010) who reported that magnetosonic perturbations are diffracted by the background inhomogeneities, and, in the presence of an X-point, wrap around it locally generating small scales. Because of the imposed v_z at the lower boundary and the frozen-in law, magnetic fieldlines at the lower boundary are forced to follow the oscillatory motion at the base. We remember that

the magnetic field is not imposed at the boundary, but is calculated using a method of projected characteristics that takes into account physical conditions imposed for the velocity. The oscillation of the value of v_z along the lower boundary causes a distortion of the magnetic structure, which is also oscillatory. In Figure 1.10 magnetic field lines are plotted at two different

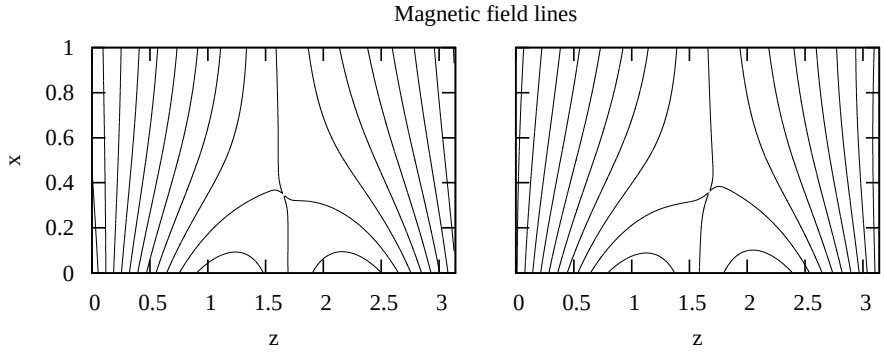

Figure 1.10: Magnetic field lines in the xz plane at times $\tau = 2$ (left panel) and $\tau = 3.5$ (right panel).

times. Each plot is obtained by drawing the isolines of the vector potential $A(x, z)$. In Appendix A we describe the method we used to calculate $A(x, z)$. By comparing Figure 1.1 we can see the distortion of the magnetic lines generated by the perturbation. In particular, the separatrices crossing at the X-point have collapsed – they no longer form right angles in the distorted configuration of Figure 1.10. This implies that a current directed along the y-direction is localized at the X-point. The current density component $j_y = \partial b_x/\partial z - \partial b_z/\partial x$ is plotted in Figure 1.11 at the time $\tau = 2$ (corresponding to the left panel of Figure 1.10). This figure represents a zoom of the region around the X-point. We can see that j_y has a maximum at the X-point and it is flattened along an oblique direction, which is between separatrices. Such an elongated X-point becomes a site of magnetic reconnection. The presence of magnetic reconnection can be revealed

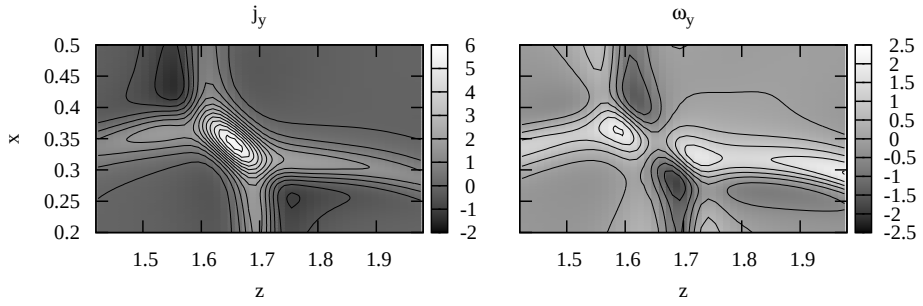

Figure 1.11: Current component j_y (left panel) and vorticity component ω_y (right panel) in the xz plane around the X-point at the time $\tau = 2$.

by plotting the vorticity y component $\omega_y = \partial v_x/\partial z - \partial v_z/\partial x$ (Figure 1.11, right panel); ω_y displays a quadrupolar structure that is typical of magnetic reconnection (Matthaeus , 1982): two opposite inflows carry magnetic flux that reconnects at the X-point and is carried away by two opposite outflows. Thus, the magnetic field distortion produced by the perturbation works as a trigger for the magnetic reconnection. This goes on until the change of sign in the velocity v_z at the base pulls fieldlines in the opposite direction, causing the X-point to become currentless and stopping the reconnection for a moment. The distortion continues until the configuration shown in the right panel of Figure 1.10 is formed, which is specular to the previous one. In this new configuration reconnection starts again, but is opposite to the previous case – previous inflows turn into outflows, and vice versa. This cycle of reconnection reversals continues periodically. In our simulation reconnection is oscillatory in time, which is a consequence of the periodic motion imposed at the lower boundary. The presence of oscillatory reconnection in a magnetic X-point perturbed by a magnetosonic was previously reported by McLaughlin et al. (2009). These authors considered an X-point at the center of a cylindrical domain, where a single δ-like magnetosonic pulse coming from the boundary converges to the X-point. The

pulse generates a sequence of alternate reconnections decaying in time that are caused by the increase of kinetic pressure in the outflow regions of the reconnection. In our simulation, we considered magnetosonic waves with a well-defined frequency, so that oscillatory reconnection goes on indefinitely without decaying. Moreover, our results show that this phenomenon can also act in more general (less symmetrical) configurations, provided that an initially potential X-point is solicited by some perturbation polarized in the same plane as the background magnetic field.

1.5 Discussion

In this chapter we studied the propagation of MHD waves in the lower layers of a coronal hole, through 2D MHD numerical simulations. Such waves are supposed to be generated by photospheric motions and propagate upward reaching higher regions of the corona and the solar wind. The main motivation is to study the formation of small scales in fluctuations, as a consequence of their interaction with features of the inhomogeneous background magnetic field, such as separatrices and X-points. Indeed, although a coronal hole is characterized by a dominant magnetic polarity, magnetograms have revealed the presence of several regions of opposite polarity (Zhang et al., 2006; Ito et al., 2010), with a typical size of the order of 10^4 km. This suggests that at low altitudes the magnetic field has a complex structure containing both open and closed fieldlines, the latter connecting regions of opposite polarity at the base. When a fluctuation crosses such a complex structure, small scales are generated. These effects have been neglected in the models of solar wind acceleration, where only large-scale inhomogeneities due to vertical stratification and spherical expansion have been included.

We considered magnetic structures with a typical size $L = 10^4$ km $\ll 1\ R_\odot$. Then, in our model we neglected curvature effects due to the spherical geometry, instead using a simpler Cartesian geometry. The equilibrium magnetic field we considered tries to reproduce the above observational features – it is a simple inhomogeneous 2D current-free field, whose vertical component b_x changes sign when moving along the base $x = 0$. In the model there are both open and closed fieldlines at small x, while only open fieldlines with a single polarity are present at large x. The magnetic structure contains separatrices that intersect at an X-point; the separatrices and the X-point play a key role in the dynamics of perturbations. The equilibrium density is supposed to be uniform. The scale height H_ρ of the density in the corona can be estimated by assuming an uniform temperature and an equilibrium between gravity and pressure gradient. $H_\rho \simeq \kappa_B T^{(0)}/(m_p g)$, where κ_B is the Boltzmann constant, m_p the proton mass, $g \simeq 2.74 \times 10^4$ cm s^{-2} the surface gravity of the Sun, and $T^{(0)} \simeq 10^6$ K. Using these values, we find $H_\rho \simeq 3 \times 10^4$ km, which is larger than the vertical size L of our domain. Thus, a uniform density is a reasonable approximation.

Fluctuations are produced by imposing a velocity v_y or v_z at the base $x = 0$ of the domain. This is intended to represent movements of lower denser layers of the solar atmosphere. In consequence of the frozen-in condition, magnetic fieldlines are carried by these motions, thus generating MHD waves that propagate from the base into the domain. The time evolution of magnetic field, density, and pressure at the base has been calculated consistently with MHD equations using a method of projected characteristics. The same method allows perturbations to exit without reflection through the upper boundary $x = 1$. Since the background magnetic field is 2D, it is possible to distinguish between Alfvénic and magnetosonic perturbations,

according to the polarization (y or xz) of the generated fluctuations.

In the case of Alfvénic perturbation we found that the formation of small scale structures takes mainly place along the separatrices. This holds both for the lower separatrices, where trapped perturbations propagates back and forth, and for the upper separatrix in the open fieldline region where fluctuations leave the domain propagating upwards. Small scales form both in the magnetic field and in the velocity perturbation. The generation of small scales along the separatrices confirms the results of previous studies, carried out using various approaches (analytical, WKB, simulation), concerning Alfvén wave propagation around an X-point (see, e.g., McLaughlin et al. (2010) for a review). The separatrices are also the places where the energy carried by the waves is trasformed into heat through dissipative effects. During the time evolution the dissipated power reaches a quasi-stationary state after an initial transient. In this quasi-stationary situation we have estimated that $\sim 10\%$ of the energy flux entering from the base is dissipated in the domain and the rest is carried out with the waves. This percentage decreases with decreasing the dissipative coefficients which in our simulations are necessarely much higher than in the coronal plasma. A more detailed analysis of this point is left for a future work. On the other hand, we can expect that if the domain had a larger extension in the x-direction, the ratio of dissipated to incoming power would be larger. In our simulation more power is dissipated by resistivity than by viscosity; this difference is due to the behaviour of waves trapped in the region of closed fieldlines, where magnetic perturbations are larger than velocity perturbations. The dominance of magnetic perturbations has been observed for low-frequency perturbations in models of turbulence in coronal loops (Nigro et al., 2004; Buchlin et al., 2007). As in our case, in these models a fluctuating velocity

is imposed at the boundaries, while outgoing perturbations are free to leave the spatial domain. The observed unbalance between velocity and magnetic field perturbations in closed fieldline regions of our model could be ascribed to a mechanism similar to that found in the models by Nigro et al. (2004); Buchlin et al. (2007), though the excitation of "in phase" fluctuations at the footpoints of closed fieldlines could also play a role in determining the excess of magnetic fluctuations.

In analysing the spectrum of the perturbation exiting from the top, we found that the energy is distributed as a power law $\propto {k_z}^{-2.3}$, at least at scales sufficiently large to neglect dissipative effects. k_z represents the main component of the wavevector, which is essentially perpendicular to $\mathbf{b}^{(0)}$. Then, the interaction of an initially spatially uniform Alfvénic perturbation with the background inhomogeneity produces an anisotropic power-law spectrum that mainly extends in the direction perpendicular to the magnetic field. This spectrum forms at low altitudes in the corona – at $X = L = 10^4$ km above the coronal base the spectrum is completely formed. These results largely confirm what has been found by Malara et al. (2012) and Malara (2013). However, while these authors employed a WKB approximation in a 3D configuration, our results are based on a direct MHD simulation in a 2D equilibrium. The above features of the spectrum are reminiscent of what happens in MHD turbulence, where nonlinear couplings generate power-law spectra with an energy cascade that mainly flows in the direction perpendicular to the mean magnetic field (e.g., Shebalin et al. (1983); Carbone & Veltri (1990)). In the present model this anisotropy is generated by the coupling between the perturbation and the inhomogeneous background, instead of nonlinear effects. However, the slope $\alpha \simeq 2.3$ of the pertubation spectrum that we find is definitely larger than what is typically found in turbulence

(e.g., 1.5 or 1.66 for a Kraichnan or a Kolmogorov spectrum, respectively). Thus, the present model cannot account for the formation of a fully developed spectrum. However, models studying the evolution of fluctuations from the corona to the solar wind, or the solar wind acceleration by dissipation of wave energy should take the phenomenon we studied here into account. For instance, Verdini et al. (2009) presented a model of turbulence formation in the sub-Alfvénic solar wind, where Alfvén waves on large scales are injected at the base and partially reflected by the vertical stratification. Although a turbulence spectrum forms as a consequence of nonlinear wave-wave interactions, the produced heat seems to be deposited at greater distances than what is needed to sustain the background wind. Our model suggests that upward-propagating waves start forming small scales at very low altitudes. Such a phenomenon can decrease the altitude of heat deposition, thus leading to a better agreement between the results of the turbulence model and the background wind structure.

The relative amplitude of perturbations we considered is low ($\delta v/c_A \sim 10^{-1}$), so that nonlinear effects should be mostly negligible. Nevertheless, the magnetic pressure gradient associated with the perturbation can locally reach larger values at locations where small scales form. As a consequence, in the vicinity of the vertical separatrix we observed the formation of density fluctuations with a relative amplitude ($\delta\rho/\rho \sim 10^{-1}$) comparable with that of the Alfvén wave. These fluctuations are sort of localized "bubbles" that propagate upward along the separatrix at a speed (~ 100 km s^{-1}) comparable with the local Alvén velocity pushed by the magnetic pressure of the Alfvén wave. The presence of density fluctuations in coronal holes with a period ~ 6 minutes has been revealed by Ofman et al. (1997). DeForest & Gurman (1998) found compressive waves in polar plumes with waveperiods

of ~ 10 minutes, propagating upward at a speed $\sim 75 - 150$ km s^{-1}, where the density fluctuation is $5\% - 10\%$ of the background value, interpreted as slow magnetosonic fluctuations (Ofman et al., 1999). On the other hand, magnetograms reveal the presence of small regions of magnetic polarity opposite the dominant plume polarity located all around the plume footpoint (DeForest et al., 1997). This could give rise to magnetic separatrix surfaces associated with the plume boundary. Our model suggests an alternative interpretation of the observed density fluctuations – namely, compressive waves, nonlinearly driven by Alfvénic fluctuations, which propagate upward along such magnetic separatrices. Finally, we noted an analogy between our magnetic structure and that of pseudostreamers (Wang et al., 2012). A certain activity has been observed in the form of faint density structures radially propagating along pseudostreamers up to distances $\sim 3R_\odot$ (Wang et al., 2007). The similarity with our model would suggest that such structures could be generated by steep magnetic pressure gradients of Alfvén waves that concentrate around the magnetic separatrix. However, since pseudostreamers can extend up to about few solar radii density stratification and spherical geometry are no longer negligible. These effects could somehow modify the wave dynamics with respect to that found in our model.

The phenomenology of magnetosonic fluctuations is completely different. First, no relevant small scales formation is observed in the waves that leave the domain through the upper boundary: spectra of velocity and magnetic field components at $x = 1$ are much steeper than for Alfvénic fluctuations, with slopes ranging from $\simeq -3.0$ to $\simeq -5.2$. We can conclude that only Alfvénic fluctuations contribute to the formation of small scales in waves that leave the domain, at least in the considered 2D configuration. However, in the magnetosonic case small scales do actually form and

dissipation takes place, but only around the X-point. The magnetic field is perturbed by the magnetosonic fluctuation so that an elongated current j_y forms at the initially potential X-point; the separatrices collapse and reconnection starts. In this scenario, fluctuations work as a trigger for reconnection. With increasing time, the motion at the base is reversed until magnetic lines at the X-point reach a configuration specular to the previous one: the reconnection pattern is reversed, with outflows turned into inflows, and vice versa. The oscillatory motion imposed at the base gives rise to an oscillatory reconnection. The phenomenon of oscillatory reconnection has been observed by Murray et al. (2009) in simulations of an emerging flux tube within a coronal hole. McLaughlin et al. (2009) studied oscillatory reconnection when a magnetosonic pulse propagates on a potential X-point. However, while these authors considered a single δ-like pulse generating a self-sustained time-decaying sequence of reconnections, in our simulation alternate reconnection indefinitely goes on driven by a continuous wave injection. Moreover, the configuration studied by McLaughlin et al. (2009) is more particular than ours, since these authors considered a cylindrically symmetric pulse converging toward the X-point. In this respect, we can say that our results extend the findings by McLaughlin et al. (2009) to more general configurations that are not necessarily constrained by cylindrical symmetry assumptions. Oscillatory reconnection has been invoked (Murray et al., 2009) to explain oscillatory emission observed during flares (e.g., Mitra-Kraev et al. (2005); McAteer et al. (2005); Inglis et al. (2008)), as well as swaying outflow jets observed above emitting loops (Cirtain et al., 2007; Shibata et al., 2007). Our results indicate that oscillatory reconnection should be a general phenomenon taking place every time a current-free X-point is stressed by a quasi-periodic perturbation.

Despite its simplicity, we believe that the present model has allowed us to gain some insight in the mechanism of small-scale formation into perturbations that propagate in the lower layers of a coronal hole. Possible improvements that we are planning for future work include both the extension to a more complex 3D structure and a more realistic representation of motions at the coronal base, which takes into account the observed temporal spectrum of photospheric motions.

Chapter 2

From Alfvén waves to kinetic Alfvén waves in an inhomogeneous equilibrium structure

Solar wind turbulence at scales much larger than the proton inertial length is dominated by Alfvénic fluctuations, which are characterized by highly-correlated velocity and magnetic field fluctuations and by low-level (with respect to the background values) density and magnetic field intensity variations (Belcher & Davis, 1971). Several indications have been found of the presence of Alfvén waves also in the solar corona (Tomczyk et al., 2007; Tomczyk & McIntosh, 2009) from where the solar wind emanates. In the scenario of solar wind turbulence, the role of spectral anisotropy must be taken into account. Theoretical studies, indeed, have shown that in a magneohydrodynamic (MHD) turbulence the energy cascade preferentially takes

place perpendicularly to the background magnetic field $\mathbf{B}_0$ (e.g., Shebalin et al. (1983); Carbone & Veltri (1990); Oughton et al. (1994)). Then, it is expected that at smaller scales the fluctuation energy tends to concentrate in nearly perpendicular wavevectors. In fact, observations show that the distribution of wavevectors of magnetic fluctuations has a significant population quasi-perpendicular to the mean magnetic field (Matthaeus et al., 1986, 1990). Moreover, all the above features, such as Alfvénic correlations and spectral anisotropy, as well as the presence of several characteristic lengthscales, can interact with large scale structures such as shears and magnetic equilibria, with a subsequent generation of wave-like activity. The a description of the full picture is a complex task, which could be addressed by means of simplified models.

Waves belonging to the Alfvén branch, with wavelengths comparable with the proton inertial length d_p and wavevectors nearly perpendicular to the mean magnetic field are often indicated as "kinetic Alfvén waves" (KAWs). During the last decades, KAWs have received considerable attention and have been studied in detail due to their possible role in a wave description of the turbulent cascade. Since the MHD cascade favours nearly perpendicular wavevectors, the expectation within a wave perspective would be that KAWs are naturally present at scales of the order of d_p. An extensive analysis in KAW physics is found in Hollweg (1999) (see also references therein for a more complete view on the subject). Many solar wind observational analyses (Bale et al., 2005; Sahraoui et al., 2009; Podesta & Tenbarge, 2012; Salem et al., 2012; Chen et al., 2013; Kiyani et al., 2013), theoretical works (Howes et al., 2008a; Schekochihin et al., 2009; Sahraoui et al., 2012) as well as numerical simulations (Gary & Nishimura, 2004; Howes et al., 2008b; TenBarge & Howes, 2012) have suggested that fluctuations near the

end of the magnetohydrodynamics inertial cascade range may consist primarily of KAWs, and that such kind od fluctuations can play an important role in the dissipation of turbulent energy. Due to a nonvanishing electric field parallel component associated with KAWs, these waves have also been considered in the problem of particle acceleration (Voitenko & Goossens, 2004; Décamp & Malara, 2006). Recently, Vásconez et al. (2014) have studied collisionless Landau damping and wave-particle resonant interactions in KAWs.

There are also situations simpler than fully developed turbulence where formation of small scales in the direction perpendicular to a background magnetic field could take place. For instance, this effect appears in the context of nonlinear MHD when imposed parallel propagating waves interact with with an inhomogeneous background consisting either of pressure balanced structures or velocity shears (Ghosh et al., 1998). In 2D inhomogeneous equilibria, where quantities vary in the direction transverse to the magnetic field, small amplitude waves can be subject to phase-mixing (Heyvaerts & Priest, 1983), in which differences in group velocity at different locations progressively bend wavefronts, thus generating small scales in the perpendicular direction. Another mechanism is resonant absorption which concentrates the wave energy in a narrow layer where the wave frequency locally matches a characteristic frequency. These processes have been studied both by a normal modes approach (Kappraff & Tataronis, 1977; Mok & Einaudi, 1985; Steinolfson, 1985; Davila, 1987; Hollweg, 1987; Califano et al., 1990, 1992) and by considering the evolution of an initial disturbance (Lee & Roberts, 1986; Malara et al., 1992, 1996). Effects of density stratification and magnetic line divergence (Ruderman et al., 1998), as well as nonlinear coupling with compressive modes (Nakariakov et al., 1997, 1998),

and evolution of localized pulses (Tsiklauri & Nakariakov, 2002; Tsiklauri et al.,, 2003) have been considered. The propagation of MHD waves in inhomogeneous magnetic fields containing null points has also been studied in detail (Landi et al., 2005; McLaughlin et al., 2010; Pucci et al., 2014), finding a fast formation of small scales perpendicular to the ambient magnetic field. In 3D inhomogeneous equilibria this process has been considered in the small wavelength limit (Similon & Sudan, 1989; Petkaki et al., 1998; Malara et al., 2000), also within the problem of coronal heating (Malara et al., 2003, 2005, 2007). Particle acceleration in phase-mixing of Alfvén waves in a dispersive regime has been studied both in 2D (Tsiklauri et al., 2005; Tsiklauri, 2011) and in 3D (Tsiklauri, 2012) configurations. Finally, instabilities generating KAWs in plasma with transverse density modulations have been considered by Wu & Chen (2013). Similar ideas involving dissipative mechanisms related to interaction of Alfvén waves or KAWs and phase mixing have been examined in the context of the magnetospheric plasma sheet (Lysak & Song, 2011) and in coronal loops (Ofman & Aschwanden, 2002).

The above considerations suggest (Hollweg, 1999) that the interaction of Alfvén waves with inhomogeneous background structures might represent a mechanism to produce KAWs, when the wavelength of waves becomes enough small to be comparable with the proton inertial length d_p. This effect could work, for instance, in the solar corona where the background magnetic field is clearly nonuniform and where the presence of Alfvén waves has been ascertained, or in the solar wind where large-scale inhomogeneities like current sheets and velocity shears are present. In a recent paper Vásconez et al. (2015) have studied a problem in which phase-mixing acting on an initial Alfvén wave generates KAWs localized in regions where the background is inhomogeneous. In this study, both fluid and kinetic simulations have

been employed; in particular, it has been found that the KAWs produced by this mechanism can modify the ion distribution function, generating temperature anisotropy and beams of particles moving parallel to the magnetic field. In the configuration considered by Vásconez et al. (2015) the initial perturbation is propagating parallel to the background magnetic field $\mathbf{B}^{(0)}$ and it is linearly polarized along a direction which is perpendicular both to $\mathbf{B}^{(0)}$ and to the inhomogeneity direction. As a consequence, the polarization remains transverse to the wavevector up to the time in which dispersive effects become active. This gives a smooth evolution of the initial Alfvén wave towards a KAW.

Clearly, the situation considered by Vásconez et al. (2015) is a particular case, and there are other possible configurations in which an initial Alfvén wave propagates in a transverse inhomogeneous structure. The aim of this work is to generalize the results of Vásconez et al. (2015) by extending the study to such different configurations, thus investigating the possibility to generate KAWs in a more general case. In particular, we want to clarify the role of phase-mixing in the generation of KAWs, by considering situations where phase-mixing may be active or not. Both fluid (Hall-MHD) and kinetic (Hybrid Vlasov-Maxwell) simulations will be employed in the present study, considering both small and large amplitude cases to investigate possible effects of nonlinearities.

In Section 1 the two models (fluid and kinetic) are presented; in section 2 we recall the main features of linear waves in Hall MHD; the results of simulations are described in Section 3, while a discussion and a summary of results are given in Section 4.

2.1 Hall-MHD and hybrid Vlasov–Maxwell numerical simulations

We study the evolution of Alfvén waves propagating in an inhomogeneous equilibrium pressure–balanced structure by means of 2.5D numerical simulations. Perturbations wavelength is large enough to make dispersive effects initially negligible. During the time evolution, the interaction between the perturbation and the equilibrium inhomogeneity generates small scales structures in which both dispersive and kinetic effects play an important role. We first study the linear case, where the perturbation amplitude is small compared with the equilibrium quantities, using an Hall-MHD (HMHD) numerical code. Then we move to the nonlinear case in which we use an hybrid Vlasov–Maxwell (HVM) code in order to single out the role of kinetic effects in the evolution of the proton distribution function. In this section we present the two models and describe the simulation initial conditions.

The HMHD description of a plasma composed by protons and electrons is valid under the following assumptions: the plasma is quasi–neutral ($n_p \simeq n_e$, with n_e and n_p the number density of protons and electrons), the temperature of the two species are the same $T_p = T_e = T_0$, the scale considered are sufficiently large to neglect the electron mass ($m_e \ll m_p$) and the characteristic plasma speed is small compared to the speed of light, so that the displacement–current term in the Ampere equation can be neglected. Under these assumptions the plasma can be described by the HMHD equations, here written in non-dimensional form:

$$\frac{\partial \rho}{\partial t} + \nabla \cdot (\rho \mathbf{v}) = 0 \tag{2.1}$$

$$\frac{\partial \mathbf{v}}{\partial t} + (\mathbf{v}\cdot\nabla)\mathbf{v} = -\frac{\tilde{\beta}}{2\rho}\nabla(\rho T) + \frac{1}{\rho}\left[(\nabla\times\mathbf{B})\times\mathbf{B}\right] \tag{2.2}$$

$$\frac{\partial \mathbf{B}}{\partial t} = \nabla\times\left[\mathbf{v}\times\mathbf{B} - \frac{\tilde{\epsilon}}{\rho}(\nabla\times\mathbf{B})\times\mathbf{B}\right] \tag{2.3}$$

$$\frac{\partial T}{\partial t} + (\mathbf{v}\cdot\nabla)T + (\gamma-1)T(\nabla\cdot\mathbf{v}) = 0 \tag{2.4}$$

In Equations (2.1)–(2.4) the mass density ρ (which is only due to protons) is normalized to a typical density $\tilde{\rho}$, temperature T to a typical value $\tilde{T}$, the pressure $p = \rho T$ due to both protons and electrons is normalized to the value $\tilde{p} = 2\kappa_B\tilde{\rho}\tilde{T}/m_p$, being κ_B the Boltzmann constant and m_p the proton mass. The spatial coordinates $\mathbf{x} = (x, y)$ are normalized to a typical length $\tilde{L}$, magnetic field $\mathbf{B}$ is normalized to a typical magnetic field $\tilde{B}$, fluid velocity $\mathbf{v}$ to the typical Alfvén speed $\tilde{c}_A = \tilde{B}/(4\pi\tilde{\rho})^{1/2}$, time t to the Alfvén time $\tilde{t}_A = \tilde{L}/\tilde{c}_A$. Moreover, $\tilde{\beta} = \tilde{p}/(\tilde{B}^2/8\pi)$ is a typical value for the kinetic to magnetic pressure ratio; $\gamma = 5/3$ is the adiabatic index; $\tilde{\epsilon} = \tilde{d}_p/\tilde{L} = 0.125$ is the Hall parameter measuring the relative amplitude of the Hall term with respect to the $\mathbf{v}\times\mathbf{B}$ term in the Ohm's law, $\tilde{d}_p = \tilde{c}_A/\tilde{\Omega}_{cp} = \tilde{c}_A m_p c/(q\tilde{B})$ being the proton inertial length.

It is worth to note that Equations (2.1)–(2.4) are ideal and adiabatic; however, to ensure numerical stability, we included an hyperviscosity and an hyperesistivity term in Equation (2.2) and in Equation (2.3), respectively. Details about the numerical algorithm can be found in Vásconez et al. (2015).

The nonlinear simulations have been performed by using an HVM code (Valentini et al.,, 2007) in which the Vlasov equation for protons is solved in a 2D–3V (two dimensional in physical space and three dimensional in velocity space) phase space, while electrons are represented as an isothermal fluid. Equations solved by the HVM code in non dimensional units are the

following:

$$\frac{\partial f}{\partial t} + \mathbf{u} \cdot \nabla f + \frac{1}{\tilde{\epsilon}} \left(\mathbf{E} + \mathbf{u} \times \mathbf{B} \right) \cdot \frac{\partial f}{\partial \mathbf{u}} = 0 \tag{2.5}$$

$$\mathbf{E} = -\mathbf{v} \times \mathbf{B} + \frac{\tilde{\epsilon}}{n} \left(\mathbf{j} \times \mathbf{B} - \frac{\tilde{\beta}}{2} \nabla P_e \right) \tag{2.6}$$

$$\frac{\partial \mathbf{B}}{\partial t} = -\nabla \times \mathbf{E} \quad ; \quad \nabla \times \mathbf{B} = \mathbf{j} \tag{2.7}$$

where $f = f(\mathbf{x}, \mathbf{u}, t)$ is the proton distribution function, $n = \int d^3u\, f$ is the proton number density normalized to $\tilde{n} = \tilde{\rho}/m_p$, $\mathbf{B}$ is the magnetic field normalized to $\tilde{B}$, $\mathbf{v} = n^{-1} \int d^3u f\, \mathbf{u}$ is the proton bulk velocity normalized to $\tilde{c}_a$, $\mathbf{E}$ is the electric field normalized to $\tilde{E} = (\tilde{c}_a \tilde{B})/c$ (where c is the speed of light), the spatial coordinates are normalized to $\tilde{L}$, time is normalized to $\tilde{t}_a = \tilde{L}/\tilde{c}_a$, j is the current density normalized to $\tilde{j} = c\tilde{B}/(4\pi \tilde{d}_p)$, and P_e is the electron pressure normalized to $\tilde{p}$. These equations are obtained under the assumption of quasi neutrality, and in the low–frequency regime where the displacement current in Ampere equation can be neglected. The value of their pressure is set equal to the initial value of the proton pressure and their inertia effects are neglected. The numerical grid is discretized with 256×1024 points in the physical domain and 51^3 points in the velocity domain. Stability is ensured by Landau damping and by dissipation inherent in the finite difference methods employed in the HVM algorithm. Periodicity is imposed in the physical space, while in the velocity domain the distribution function f is set equal to zero for $|u_i| > u_{max}$ $(i = x, y, z)$, where $u_{max} = 5v_{th,p}$, being $v_{th,p}$ the proton thermal speed. A detailed description of the numerical method employed to solve Equations (2.5)–(2.7) can be found in Valentini et al., (2007).

For both models we choose a spatial domain $D(x, y) = [0, 2\pi] \times [0, 2\pi]$ and we set the same initial condition, which consists in a pressure–balanced

equilibrium structure with a perturbation superposed on it. The equilibrium magnetic field, that varies only in the y direction, has this form:

$$\mathbf{B}^{(0)} = B^{(0)}(y)\cos(\theta)\mathbf{e}_x + B^{(0)}(y)\sin(\theta)\mathbf{e}_z \tag{2.8}$$

where:

$$B^{(0)}(y) = 1 + \frac{b_m - 1}{1 + \left(\dfrac{y-\pi}{2\pi h}\right)^r} + \alpha\left(\frac{y}{\pi} - 1\right)^2 \tag{2.9}$$

$\mathbf{e}_x$ and $\mathbf{e}_z$ are the unit vector along x and z, θ is the angle that $\mathbf{B}^{(0)}$ forms with $\mathbf{e}_x$, $b_m = 1.5$, $h = 0.2$, $r = 10$ and

$$\alpha = \frac{(b_m - 1)r}{2(2h)^r\left[1 + \left(\dfrac{1}{2h}\right)^r\right]^2} \simeq 2.62 \times 10^{-4}. \tag{2.10}$$

The value of α has been set in order to make the first derivatives of $B^{(0)}(y)$ null at the two boundaries $y = 0$ and $y = 2\pi$. The field $B^{(0)}(y)$ is symmetrical with respect to $y = \pi$, that is the middle of the domain, where it reaches the maximum value b_m. It is worth to note that the $B^{(0)}(y)$ intensity is almost homogeneous in the central part of the domain, while moving to the sides it rapidly decreases to a smaller value. The two shear regions where $B^{(0)}(y)$ sharply varies can be seen in Figure 2.1 and have a width $\Delta y \sim 1$. In these regions two strong current sheets in the z direction are present. The temperature is homogeneous, its value being $T^{(0)} = 1$, and the velocity is null at the initial time. The mass density $\rho^{(0)}$ is set to guarantee equilibrium between kinetic and magnetic pressure:

$$\frac{\tilde{\beta}}{2}\rho^{(0)}(y)T^{(0)} + \frac{{B^{(0)}}^2(y)}{2} = P_T^{(0)} \tag{2.11}$$

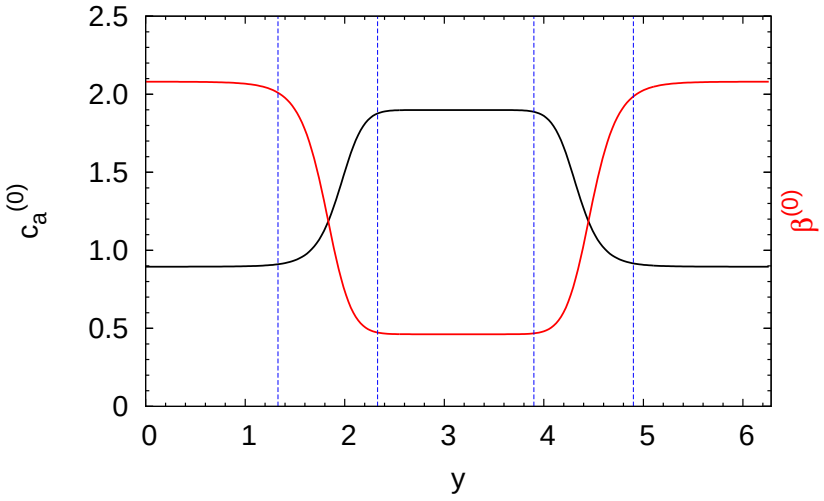

Figure 2.1: Alfvén velocity (red solid line) and plasma β (black solid line) in the equilibrium structure in function of y. The dashed blue lines delimit the two shear region.

where $P_T^{(0)} = 1.748$ and $\tilde{\beta} = 2$. The initial Alfvén velocity

$$c_a{}^{(0)} = B^{(0)}(y)/(\rho^{(0)})^{1/2}(y)$$

and plasma β:

$$\beta^{(0)}(y) = [c_s{}^{(0)}/c_a{}^{(0)}]^2$$

profiles (where $c_s{}^{(0)} = [\gamma T^{(0)}]^{1/2}$ is the sound speed) are plotted in Figure 2.1 as functions of y. The Alfvén velocity is larger in the middle of the domain and decreases in the shears to reach a lower value on the two sides. On the other hand, the plasma β has an opposite trend: it varies from smaller values $\beta < 1$ in the middle of the domain to higher values $\beta > 1$ in the two side regions. (Vásconez et al., 2015) considered this equilibrium structure in the particular case where $\theta = 0$. This case corresponds to an in-plane equilibrium magnetic field.

The initial perturbation represents a linearly polarized Alfvén wave.

Table 2.1: Numerical parameters in simulations (Hall parameter $\tilde{\epsilon} = 0.125$).

RUN	Type	Spatial Resolution ($n_x \times n_y$)	Amplitude (a)	θ
1	HMHD	256×256	0.01	0
2	HMHD	256×256	0.01	$\pi/4$
3	HVM	256×1024	0.25	0
4	HVM	256×1024	0.25	$\pi/4$

Thus, the polarization direction must be perpendicular both to $\mathbf{B}^{(0)}$ and to the initial wavevector $\mathbf{k}_0$. In the initial condition $\mathbf{k}_0$ is oriented along x, while $\mathbf{B}^{(0)}$ is in the xz plane. Thus, the initial perturbation must be polarized along y, at least for $\theta \neq 0$. Then, we choose the following form for the initial velocity and magnetic field perturbation:

$$\mathbf{B}^{(1)}(x, y, t = 0) = a\cos(x)\mathbf{e}_y, \quad \mathbf{v}^{(1)}(x, y, t = 0) = -a[\rho^{(0)}(y)]^{-1/2}\cos(x)\mathbf{e}_y \tag{2.12}$$

where a gives the perturbation amplitude and $k_0 = 1$.

In the case $\theta = 0$ (in-plane magnetic fild), $\mathbf{B}^{(0)}$ and $\mathbf{k}_0$ are parallel and directed along x, so the initial polarization could be directed along any direction in the yz plane. In practice, for $\theta = 0$ it is sufficient to consider only two independent orientations for the initial polarization: the first one is along y and has again the form (2.12); the second one is along z and has the form (2.12) in which the unit vector $\mathbf{e}_y$ is replaced by the unit vector $\mathbf{e}_z$. The latter case corresponds to the configuration studied by Vásconez et al. (2015). Then, in the present work we will consider the other two possibilities, using the form (2.12) for the velocity and magnetic field perturbation and considering both the case $\theta = 0$ and a case with $\theta \neq 0$, for which we set $\theta = \pi/4$. In both cases, the initial density and temperature fluctuations are vanishing: $\rho^{(1)}(x, y, t = 0) = 0$, $T^{(1)}(x, y, t = 0) = 0$. The numerical

parameter of the various simulation performed are summarized in Table 2.1. Note that the wave amplitude chosen for the HMHD runs is $a = 0.01$, while we set $a = 0.25$ for the HVM simulations in order to make the effects on the particle distribution function more visible. We will refer to the to HMHD simulation with $\theta = 0$ and $\theta = \pi/4$ as RUN 1 and RUN 2, respectively, and to the corresponding HVM simulation as RUN 3 and RUN 4, respectively.

2.2 Linear waves in Hall MHD

This section is devoted to describe the main feature of the linear waves that are normal modes in Hall MHD. We start from Equations (2.1)-(2.4) and consider an homogeneous plasma with dimensionless density ρ_0 and temperature T_0, that is permeated by an homogeneous magnetic field $\mathbf{B}_0$. The plasma is at rest at the beginning: $\mathbf{v}_0 = 0$. We perturb this equilibrium structure with a small amplitude fluctuation and linearize the equations getting equations for the fluctuations. Then we write the unknown fluctuations as a superposition of plane waves and we get the equation for the fluctuations amplitudes. Imposing non vanishing amplitudes leads to an equation of this type:

$$\omega^6 + C_1\omega^4 + C_2\omega^2 + C_3 = 0 \tag{2.13}$$

with

$$C_1 = -k_\parallel^2\left(2c_{A0}^2 + c_{s0}^2\right) - k_\perp^2\left(c_{A0}^2 + c_{s0}^2\right) - \frac{c_{A0}^4 k_\parallel^2\left(k_\parallel^2 + k_\perp^2\right)}{\omega_{p0}^2} \tag{2.14}$$

$$C_2 = c_{A0}^2 k_\parallel^2\left(c_{A0}^2 + 2c_{s0}^2\right)\left(k_\parallel^2 + k_\perp^2\right) + \frac{c_{A0}^4 c_{s0}^2 k_\parallel^2\left(k_\parallel^4 + 2k_\parallel^2 k_\perp^2 + k_\perp^4\right)}{\omega_{p0}^2} \tag{2.15}$$

$$C_3 = -c_{A0}^4 c_{s0}^2 k_\parallel^4\left(k_\parallel^2 + k_\perp^2\right) \tag{2.16}$$

In Equations (2.13)-(2.16), $k_\parallel$ and $k_\perp$ are the wavevector component parallel and perpendicular to $\mathbf{B}_0$, respectively, normalized to a typical length $\tilde{L}$; $c_{A0} = B_0/(4\pi\rho_0)^{1/2}$ and $c_{s0} = (\tilde{\beta}\gamma T_0/2)^{1/2}$ are the Alfvén and sound speed associated with the equilibrium structure, respectively, where $\tilde{\beta}$ is the typical ratio between the kinetic and magnetic pressure; ω is the frequency normalized to $\tilde{t}_A^{-1} = \tilde{L}/\tilde{c}_{A0}$ and $\omega_{p0} = (q\tilde{B}B_0/(m_p c))(\tilde{L}/\tilde{c}_A)$ is the normalized proton gyrofrequency. The expression (2.13)-(2.16) are equivalent to what found by Vásconez et al. (2014) in a two fluid model if the electron inertia is neglected. Equation (2.13) has been analytically solved (Vásconez et al., 2014) using the Vieta's substitution method (Birkhoff & Mac Lane, 1977) for the calculation of the complex roots of a third-degree algebraic equation. For given values of $k_\parallel$ and $k_\perp$ three real and positive solutions are found for ω^2, corresponding to the Alfvén, fast magnetosonic (FM) and slow magnetosonic (SM) branches, respectively. In particular, KAWs correspond to the Alfvén branch for $k_\parallel \ll k_\perp \sim \omega_{p0}/c_{A0}$.

It is possible to calculate the expression of the fluctuations amplitudes from linear analysis. If a reference frame is considered where the x-axis is along $\mathbf{B}_0$ and the wavevector $\mathbf{k}$ is in the xy plane, the perturbation components for a wave with wavevector $\mathbf{k} = k_\parallel \mathbf{e}_x + k_\perp \mathbf{e}_y$ can be expressed in the following form:

$$v_{1x} = a\frac{c_{A0}^2 c_{s0}^2 k_\parallel^2 k_\perp \omega_{p0}}{\omega^2\left(\omega^2 - c_{s0}^2 k^2\right)}\left(1 - \frac{\omega^2}{c_{A0}^2 k_\parallel^2}\right)\sin(k_\parallel x + k_\perp y - \omega t + \phi) \tag{2.17}$$

$$v_{1y} = a\frac{c_{A0}^2 k_\parallel \omega_{p0}\left(\omega^2 - c_{s0}^2 k_\parallel^2\right)}{\omega^2\left(\omega^2 - c_{s0}^2 k^2\right)}\left(1 - \frac{\omega^2}{c_{A0}^2 k_\parallel^2}\right)\sin(k_\parallel x + k_\perp y - \omega t + \phi) \tag{2.18}$$

$$v_{1z} = -a\frac{c_{A0}^2 k_\parallel}{\omega}\cos(k_\parallel x + k_\perp y - \omega t + \phi) \tag{2.19}$$

$$B_{1x} = aB_0 \frac{k_\parallel k_\perp \omega_{p0}}{\omega k^2} \left(1 - \frac{\omega^2}{c_{A0}^2 k_\parallel^2}\right) \sin(k_\parallel x + k_\perp y - \omega t + \phi) \tag{2.20}$$

$$B_{1y} = -aB_0 \frac{k_\parallel^2 \omega_{p0}}{\omega k^2} \left(1 - \frac{\omega^2}{c_{A0}^2 k_\parallel^2}\right) \sin(k_\parallel x + k_\perp y - \omega t + \phi) \tag{2.21}$$

$$B_{1z} = aB_0 \cos(k_\parallel x + k_\perp y - \omega t + \phi) \tag{2.22}$$

where a is the perturbation amplitude, $\phi \in [0, 2\pi]$ is the phase and $\omega = \omega(\mathbf{k})$ is derived from the dispersion relation (2.13). From (2.13) it is also possible to find the expression for the parallel and perpendicular group velocity. We consider Equation (2.13) written in the implicit form:

$$F(\omega(k_\parallel, k_\perp), k_\parallel, k_\perp) \equiv 0 \tag{2.23}$$

which holds for any value of $k_\parallel$ and $k_\perp$. The total derivative of Equation (2.23) respect to $k_\parallel$ is:

$$\frac{dF}{dk_\parallel} = \frac{\partial F}{\partial \omega}\frac{\partial \omega}{\partial k_\parallel} + \frac{\partial F}{\partial k_\parallel} = 0$$

from which we obtain

$$v_{g\parallel} = \frac{\partial \omega}{\partial k_\parallel} = -\frac{\partial F/\partial k_\parallel}{\partial F/\partial \omega}. \tag{2.24}$$

where $v_{g\parallel}$ is the parallel group velocity. In a similar way we obtain the perpendicular group velocity:

$$v_{g\perp} = \frac{\partial \omega}{\partial k_\perp} = -\frac{\partial F/\partial k_\perp}{\partial F/\partial \omega}. \tag{2.25}$$

The derivatives of F appearing in equations (2.24-2.25) calculated by using

Equation (2.13) are:

$$\frac{\partial F}{\partial k_\parallel} = -2\left[k_\parallel\left(2c_{A0}^2 + c_{s0}^2\right) + \frac{{c_{A0}}^2}{{\omega_{p0}}^2}\left(2k_\parallel^3 + k_\parallel k_\perp^2\right)\right]\omega^4 +$$
$$2\left[\left(2c_{s0}^2 c_{A0}^2 + c_{A0}^4\right)\left(2k_\parallel^3 + k_\parallel k_\perp^2\right) + \frac{{c_{A0}}^4 {c_{s0}}^2}{\omega_{p0}^2}\left(3k_\parallel^5 + k_\parallel^4 k_\perp^2 + k_\parallel k_\perp^4\right)\right]\omega^2 -$$
$$2c_{s0}^2 c_{A0}^4\left(3k_\parallel^5 + 2k_\parallel^3 k_\perp^2\right) \quad (2.26)$$

$$\frac{\partial F}{\partial k_\perp} = -2\left[k_\perp\left(c_{A0}^2 + c_{s0}^2\right) + \frac{k_\perp k_\parallel^2 c_{A0}^4}{\omega_{p0}^2}\right]\omega^4 +$$
$$2\left[k_\perp k_\parallel^2\left(2c_{s0}^2 c_{A0}^2 + c_{A0}^4\right) + 2\frac{\left(k_\perp k_\parallel^4 + k_\perp^3 k_\parallel^2\right) c_{A0}^4 c_{s0}^2}{\omega_{p0}^2}\right]\omega^2 - 2k_\perp k_\parallel^4 c_{s0}^2 c_{A0}^4 \quad (2.27)$$

$$\frac{\partial F}{\partial \omega} = 6\omega^5 - 4\left[k^2\left(c_{A0}^2 + c_{s0}^2\right) + k_\parallel^2 c_{A0}^2 + \frac{k^2 k_\parallel^2 c_{A0}^2}{\omega_{p0}^4}\right]\omega^3 +$$
$$2\left[k^2 k_\parallel^2\left(2c_{s0}^2 c_{A0}^2 + c_{a0}^4\right) + \frac{k_\parallel^2 k^4 c_{A0}^4 c_{s0}^2}{\omega_{p0}^2}\right]\omega \quad (2.28)$$

where $k^2 = k_\parallel^2 + k_\perp^2$. Since in the simulation considered in this work fluctuations at large $k_\perp$ develops during the system evolution we plotted in Figure 2.2 the parallel and perpendicular velocities in function of $k_\perp$ for $k_\parallel = 1$ and for two different values of β_0 corresponding to the shear and homogeneous side regions of the equilibrium structure considered. We can see that in the parallel direction the group velocities are positive for all the three modes. In particular parallel group velocity increases with $k_\perp$ for KAW and decreases for FM and SM modes. Perpendicular group velocity increases for all the three modes at increasing $k_\perp$ rapidly reaching an asymptotic value. It is

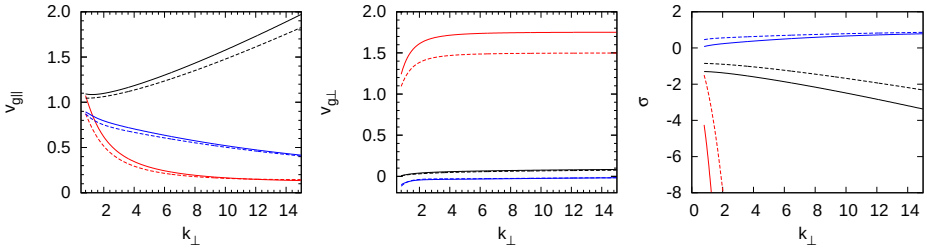

Figure 2.2: Parallel group velocity (left panel), perpendicular group velocity (middle panel), and σ (right panel) as functions of $k_\perp$, for $k_\parallel = 1$ (RUN 1). Red lines correspond to Fast mode, black lines to kinetic Alfvén wave and blue lines to Slow mode. Dashed lines for $\beta = 1.25$, full lines for $\beta = 2.08$.

always positive for KAW and FM and negative for SM. It is worth noting perpendicular group velocity for FM is much more bigger than for KAW. We notice also that the group velocities are similar for the two values of β_0 considered for all the three modes. Finally in Figure 2.2 (right panel) we plotted the quantity:

$$\sigma = 1 - \frac{\omega^2}{c_{A0}^2 k_\parallel^2}. \tag{2.29}$$

that appears in Equations (2.17)-(2.22). If the condition $k_y \gg k_x$ holds, that in our configuration means $k_\perp \gg k_\parallel$, $\nabla \cdot \mathbf{B} = 0$ implies that the dominant components of a quasi-oblique fluctuation will be B_{1x} and B_{1z}. Equations (2.17)-(2.22) indicates that in this case such fluctuation is elliptically polarized. For positive $k_\parallel$ and $k_\perp$ and given values of t and x, as one increases the y coordinate, the perturbation magnetic field rotates clockwise (counterclockwise) in the zx plane for negative (positive) values of σ. Since the sign of σ is unique for the three modes, positive for SM and negative for KAW and FM, the polarization of the magnetic field perturbation can be used, along with information about group velocity, to distinguish one mode from the other.

2.3 Numerical results

We first summarize results obtained by Vásconez et al. (2015) in order to make a comparison with the new configuration here considered. In Vásconez et al. (2015) the initial Alfvénic perturbation, which propagates in the inhomogeneous equilibrium structure, undergoes phase-mixing, as predicted by the linear MHD theory (Heyvaerts & Priest, 1983). Phase-mixing is localized in the two shear layers, where the Alfvén velocity is inhomogeneous. The wavevector of the initial perturbation is $k_0 = k_\parallel = 1 \ll \tilde{\varepsilon}^{-1}$, so that dispersive effects are initially negligible. However, in consequence of phase-mixing, within the shear layers the perpendicular wavevector $k_\perp$ of the perturbation increases in time, while the parallel wavevector $k_\parallel$ remains constant. When the condition $k_\perp \sim {d_p}^{-1} \gg k_\parallel$ is satisfied, the Alfvén wave becomes a kinetic Alfvén wave (KAW), in which dispersive effects are no longer negligible. In particular, the initial linear polarization is transformed into an elliptical polarization. KAWs formed by this mechanisms are initially localized within the shear layers; however, due to a non-vanishing perpendicular group velocity $v_{g\perp}$, KAWs drift laterally and move into the homogeneous regions. This time evolution is observed in the low-amplitude case and a similar behavior is found also in the non-linear case, both in HMHD and in HVM simulations. Moreover, in the kinetic simulation a departure of the proton distribution function from a Maxwellian is observed to take place, but only in the regions where KAWs are present: while f remains essentially gyrotropic in the velocity space, the parallel temperature $T_\parallel$ can locally become either larger or smaller than the perpendicular temperature $T_\perp$, according to the phase of the KAW. In regions where $T_\parallel$ is particularly large, a well-distinct protons beam moving parallel to the local magnetic field is recovered. The beam velocity is comparable with the KAW parallel

velocity of propagation, indicating that KAWs can accelerate protons along the magnetic field, at least for a large-amplitude initial perturbation. KAWs are also characterized by a parallel electric field $E_{\parallel}$, due to electron pressure gradients. The related electric potential energy modulation is of the order of the proton thermal energy; thus indicating that the observed particle beams are probably generated by $E_{\parallel}$ associated with KAW.

2.3.1 HMHD simulation in the in-plane $B^{(0)}$ case

We discuss now the results relative to RUN 1. In this case both the initial perturbation and the equilibrium magnetic field are in the plane xy. In this run the phenomenology is more complex and richer than that observed by Vásconez et al. (2015), though KAWs formation of is found also in this case. Since the equilibrium structure quantities depend only on y, we define quantities relative to the perturbation at any time as $\delta g = g - < g >_x$, where g indicates any physical quantity and $< g >_x$ is its average in the x direction. At the beginning of the simulation a rapid formation of compressive fluctuations is observed in the two shear layers. In particular, density perturbations are generated. This phenomenon, which was absent in Vásconez et al. (2015), is due both to the perturbation y-polarization and to the background density inhomogeneity; in fact, from the continuity equation at the initial time we derive:

$$\left.\frac{\partial \rho}{\partial t}\right|_{t=0} = -\frac{\partial \left(v^{(1)}\rho^{(0)}\right)}{\partial y} = -\frac{a\cos(x)}{2\sqrt{\rho^{(0)}(y)}}\frac{d\rho^{(0)}}{dy} \tag{2.30}$$

where we used Equations (2.12). Equation (2.30) indicates that density fluctuations are initially generated at positions where $\rho^{(0)}$ is inhomogeneous, with the same periodicity in the x direction as the initial wave and a width

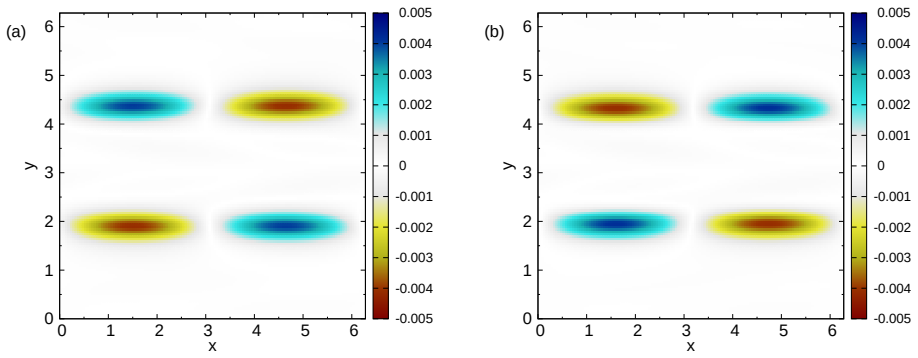

Figure 2.3: Entropy waves in shear regions: time averaged density fluctuation $\delta\rho_t$ (a) and temperature fluctuation δT_t (b) (RUN 1).

in the y direction of the order of the shear layer width $2\pi h \sim 1$. At subsequent times this perturbation remains partially confined within the shear layers. This density perturbation has a non-vanishing time average, which is indicated as $\delta_t\rho = \langle\delta\rho\rangle_t$, where the average is calculated over the whole simulation time. $\delta_t\rho$ represents a static component of the density perturbation and it is plotted in Fig. 2.3, along with the time-averaged temperature fluctuation $\delta_t T = \langle\delta T\rangle_t$. It can be seen that the static components of density and temperature fluctuations are perfectly anti-correlated; then we can interpret such fluctuations as entropy waves, which are static pressure-balanced structures in which no velocity and magnetic field fluctuations are involved. The amplitude of the entropy waves is $\sim 5\times10^{-3}$, which is $\sim 25\%$ of the amplitude of the density perturbation in the shear layers. The remaining part corresponds to a density perturbation which propagates along x remaining essentially confined within the shear layers. This perturbation could tentatively be attributed to a slow-mode wave, whose group velocity is directed along $B^{(0)}$ in the MHD limit.

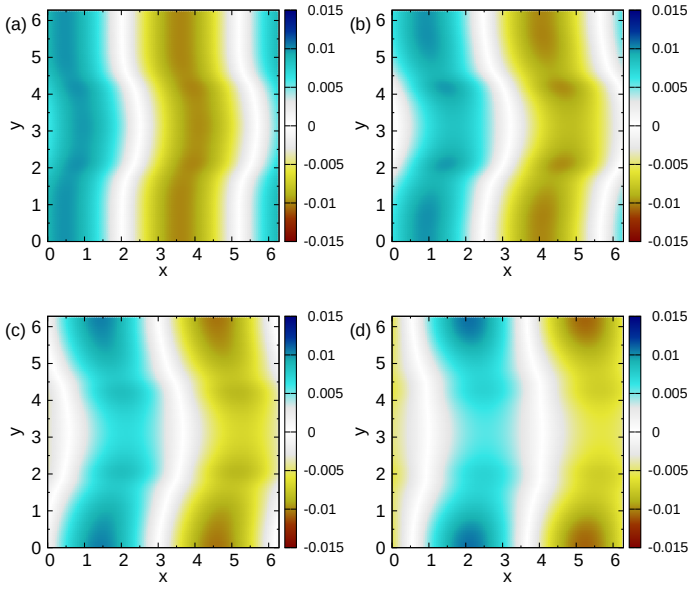

Figure 2.4: Fast wave generation at initial times (RUN 1). δB_y is plotted at the time $t = 0.5$ (a), $t = 1.0$ (b), $t = 1.5$ (c), $t = 2.0$ (d).

Another phenomenon that develops starting from the initial time is the formation of fast-mode perturbations which have origin at the shear layers and propagates perpendicularly to the background magnetic field. In Figure 2.4 the rapid formation and propagation of this structure is showed. We can see that at time $t = 2$ this kind of waves are exiting the domain and, because of periodicity, they enter from the other side. This propagation of a fast-mode perturbation goes on along all the simulation and involves only vector components in the xy plane.

To summarize, in the first stage of the time evolution the initial perturbation couples with the background inhomogeneity producing compressive perturbations belonging to the three compressive MHD modes (fast, slow and entropy waves). We note that a similar behavior was also found in previous purely MHD simulations (Malara et al., 1996). These features were not found in the linear simulations by Vásconez et al. (2015), except for

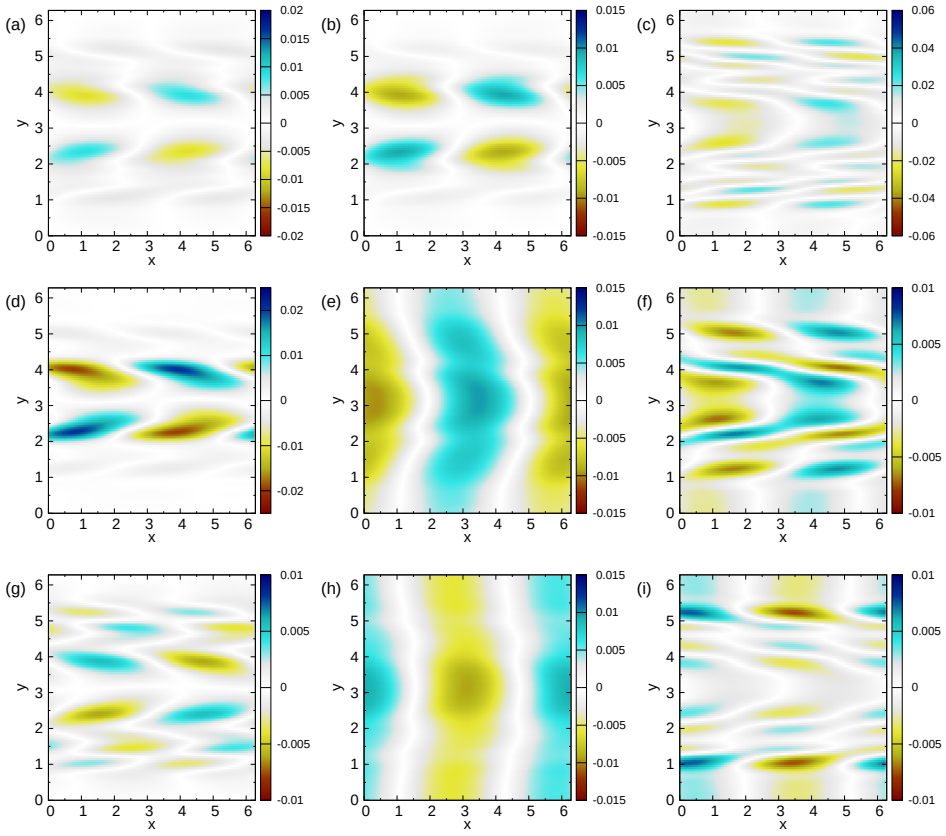

Figure 2.5: $\delta\rho$ (a), δT (b), δj_z (c), δv_x (d), δv_y (e), δv_z (f), δB_x (g), δB_y (h), δB_z (i) at time $t = 15.0$ (RUN 1).

much smaller compressive fluctuations generated by higher-order nonlinear couplings. As time goes on, other dynamical features can be appreciated. In Figure 2.5 various quantities are represented at time $t = 15$ for RUN 1. A relevant characteristic is the lack of phase-mixing of the initial wave, as it can be seen in the plots of δv_y and δB_y. This is an important difference with respect to the configuration considered in Vásconez et al. (2015), where phase-mixing is present and produces small scales. The lack of phase-mixing in this configuration has been found also in purely MHD simulations (Malara et al., 1996). In Fig. 2.5 the formation of fluctuations in the z direction can be observed: this phenomenon can only be due to dispersive effects, since

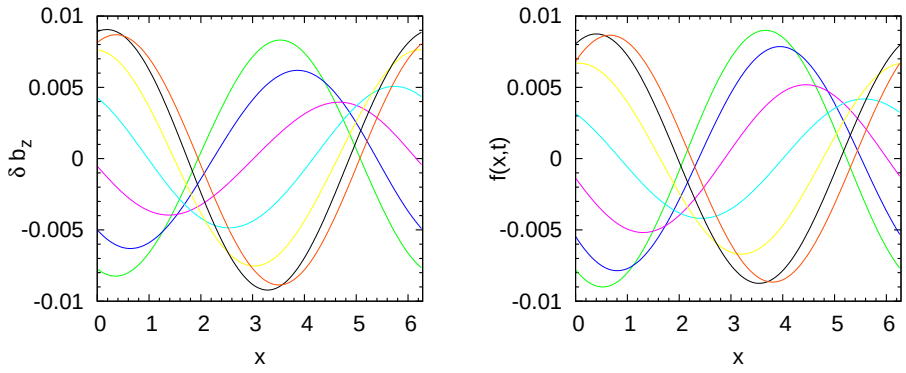

Figure 2.6: $\delta b_z(x, y = 5, t)$ (left panel) and $b(x, t)$ (right panel) as functions of x at different times: $t = 11.0$ (green), $t = 11.5$ (blue), $t = 12.0$ (purple), $t = 12.5$ (light blue), $t = 13.0$ (yellow), $t = 13.5$ (black), $t = 14.0$ (orange).

in the MHD limit an initial 2D configuration must necessarily remains 2D for subsequent times. Dispersive effects are more relevant at small scales, and in RUN 1 the velocity and magnetic field z components are present in structures which have a small transverse size and are localized at the shear layers. These structures are still visible at subsequent times ($t = 15$, Fig. 2.5), outside the shear layers where they have drifted in the meanwhile.

However, since no phase-mixing is present, another kind of coupling between the initial wave and the background inhomogeneity must be responsible for such a small-scale structure formation. We will show that these structures can be identified as the z component of KAW fluctuations. The typical transverse size of such structures is of the order of the shear layer width ~ 1, while it was smaller for the configuration considered in Vásconez et al. (2015), where phase-mixing was active. To study in more detail the nature of this perturbation we plotted the profile of δB_z as a function of x at $y = 5$ for different times (left panel in Figure 2.6). These profiles are sinusoidal with a wavelength equal to the domain size (2π), propagating in the direction of increasing x; their amplitude is not constant in time, but

it is modulated changing periodically between a maximum and a minimum value. We can interpret this behavior as due to the superposition of two waves with different amplitudes; these two waves have the same wavevector k_x but opposite frequencies $\pm\omega$, so their profiles appear to oppositely propagate along x. The wave with the largest (smallest) amplitude propagates in the direction of increasing (decreasing) x. At the time of maximum amplitude the two waves are in phase, while they are out of phase by π when the amplitude of δB_z is minimum. To prove this interpretation we considered the following analytical expression:

$$b(x,t) = A_1 \sin\left[k_x x - \omega(t-t_0) + \phi_1\right] - A_2 \sin\left[k_x x + \omega(t-t_0) + \phi_2\right] \quad (2.31)$$

that represents the two waves propagating in the opposite direction, and we tried to choose the free parameters in the above expression in a way to reproduce the time evolution of the δB_z profile. In Figure 2.6 (right panel) the function $b(x,t)$ is plotted at the same times as in the left panel, for the following values of the parameters: $A_1 = 6.5\times10^{3}$, $A_2 = 2.5\times10^{-3}$, $\omega = 1.2$, $\phi_1 = -(2/3)\pi$, $\phi_2 = \pi/3$ and $t_0 = 13$. By comparing the two panels of Fig. 2.6, we can see that $b(x,t)$ reproduces remarkably well the time evolution of the δB_z profile. Then, we conclude that the δB_z perturbation is formed by two opposite propagating waves. The wave with the largest amplitude propagates along x in the same direction as the initial perturbation.

In order to identify these waves, we followed the following procedure. First we estimated the perpendicular wavenumber of the δB_z perturbation finding $k_\perp \simeq 6.24$. This means that these waves propagate highly oblique to the direction of the background magnetic field. The angle between the wavevector and the background magnetic field direction (x direction) is $\theta =$

$\arctan(k_\perp/k_\parallel) \simeq 81°$. Considering $\omega \simeq 1.2$ and $k_\parallel = 1$ we can estimate a parallel velocity of propagation as $v_\parallel = \omega/k_\parallel \simeq 1.2$. We have also estimated the perpendicular velocity of propagation of this kind of structures in the following way. We identify the position of the structure in the y direction at time t as $y_m(t) \pm \delta y$, where y_m is the point where δB_z is minimum and $\delta y = 0.1$ is an estimation of the incertitude of the minimum position; this incertitude is partially due to the fact that the two opposite-propagating perturbations are not exactly superposed along y . Then, we measure the displacement $\Delta y_m = y_m(t_1) - y_m(t_1 + \Delta t)$ of the minimum, where t_1 is the initial time of an oscillation period and Δt is the period duration. Finally, we estimate the perpendicular velocity as $v_\perp = \Delta y_m/\Delta t$ finding the value $v_\perp = (5.32 \pm 2.8) \times 10^2$. The above values found for the parallel $v_\parallel$ and perpendicular $v_\perp$ propagation velocities of the observed structures have been respectively compared with the parallel $v_{g\parallel}$ and perpendicular $v_{g\perp}$ group velocities of propagating modes, derived from the linear HMHD theory. The details on the calculation of the explicit expressions for $v_{g\parallel}$ and $v_{g\perp}$ have been given in Section 2.2. The two components of the group velocity depend on $k_\parallel$, $k_\perp$ and β (equations (2.24)-(2.28)); for $k_\parallel$ and $k_\perp$ we used the above-estimated values, while we used $\beta = 2.08$ corresponding to the value of $\beta^{(0)}$ at the position $y = 5$ where the considered perturbations are localized. The corresponding values of the ω and of the group velocities $v_{g\parallel}$ and $v_{g\perp}$ calculated by Equations (2.24)-(2.28) are given in Table 2.2. We can see that the parallel and perpendicular propagation velocities, along with the value of the frequency ω, are in agreement with the values predicted by linear theory for KAW. It is also important to notice that the estimated values of ω, $v_\parallel$ and $v_\perp$ are very different from the corresponding values obtained from the linear theory for the Fast Magnetosonic (FM) and Slow Magnetosonic

Table 2.2: Frequency ω, group velocities $v_{g\parallel}$ and $v_{g\perp}$, and parallel phase velocity $v_{\phi\parallel} = \omega/k_\parallel$, for $k_\parallel = 1$, $k_\perp = 6.24$, $\beta = 2.08$, for kinetic Alfvén wave (KAW), fast magnetosonic (FM) and slow magnetosonic (SM) wave. The velocities values are normalized to the local Alfvén velocity.

	ω	$v_{g\parallel}$	$v_{g\perp}$	$v_{\phi\parallel}$
KAW	1.30	1.31	0.066	1.30
FM	11.0	0.23	1.74	11.1
SM	0.062	0.62	-0.032	0.62

(SM) modes. For example, the FM velocity in the perpendicular direction would be much greater, and the SM velocity, even if of the same order, would be directed in the opposite direction. Then, the observed localized structure behaves as a KAW, as long as frequency and propagation velocities are concerned.

A further evidence concerning the nature of this perturbation can be deduced on the base of the magnetic field polarization. In Fig. 2.7 we have plotted an hodogram of the perturbation, where the two components δB_x and δB_z are plotted as functions of y. We selected these two components because they are almost transverse to the wavevector orientation, which is almost aligned in the y direction. The hodogram shows that the magnetic field in the considered perturbation turns clockwise when moving in the wavevector direction. On the other hand, from the linear theory (see section 2.2) we can deduce that the magnetic field perturbation is elliptical and it turns clockwise for KAW and FM waves, while it turns counterclockwise for SM waves. Then, the sense of polarization of the localized δB_x-δB_z perturbation is coherent with that of a KAW.

On the base of the above considerations, we conclude that this perturbation belongs to the KAW mode. In particular, this perturbation contains two distinct KAWs, with amplitudes of the same order, which propagate

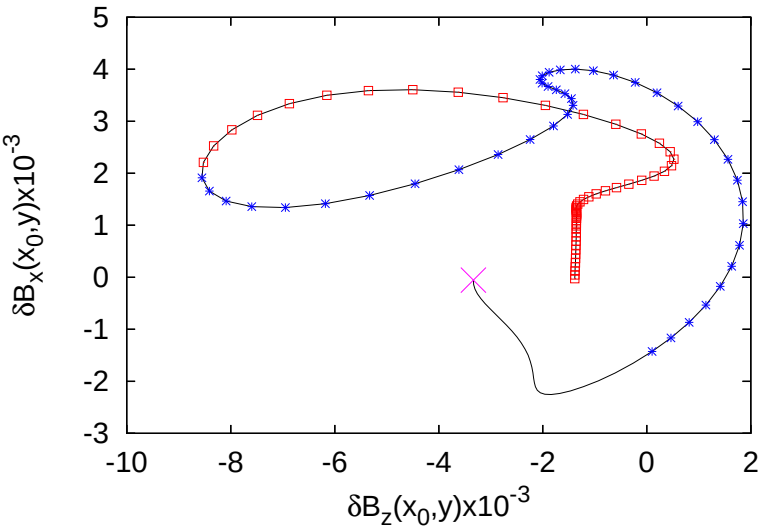

Figure 2.7: Hodogram of δB_z and δB_x for $\pi \leq y \leq 2\pi$ at $x = \pi$ and $t = 13.0$ (black line). The purple cross indicates the value at $y = \pi$, shear region values are plotted with blue asterisks and out of shear values with red squares.(RUN 1)

in opposite directions along x, but drifting in the same direction along y. This condition can be obtained assuming that the two KAWs have the same parallel wavenumber $k_\parallel$, opposite frequency ω and opposite perpendicular wavevector $k_\perp$. In fact, from Equations (2.13)-(2.16) we see that the dispersion relation does not changes under the transformation $k_\perp \rightarrow -k_\perp$. Moreover, from Equations (2.24)-(2.28) we see that $v_{g\parallel}$ changes sign and $v_{g\perp}$ remains unchanged under the transformation $k_\perp \rightarrow -k_\perp$, $\omega \rightarrow -\omega$. Finally, we note that, from Equations (2.20) and (2.22), the sense of polarization remains unchanged under the above transformation; then, we can deduce that the two KAWs forming the considered perturbation have the same sense of polarization.

In conclusion, the simulation shows that in the considered configuration KAWs are formed from the initial Alfvénic perturbation. This happens even in this case in which phase-mixing is not present. Since the equilib-

rium structure is not homogeneous in the perpendicular direction, there is a coupling between the initial perturbation with wavevector k_x with a k_y associated with the equilibrium structure. This is also confirmed by the fact that the estimated $k_\perp$ of the KAW is of the order of $2\pi/\delta y_s$ where δy_s is the size of the shear layers.

2.3.2 HMHD simulation in the out-of-plane $B^{(0)}$ case

Now we discuss the results obtained in RUN 2. Comparing with the case of RUN 1 where equilibrium magnetic field was aligned with the initial wavevector, in this new configuration $\mathbf{B}^{(0)}$ is oriented with an angle of $\pi/4$ with respect to the initial $\mathbf{k}$, while the initial perturbation is still linearly polarized in the y direction, perpendicular to both $\mathbf{B}^{(0)}$ and $\mathbf{k}$. In this respect, the initial perturbation is an Alfvén wave. The fluctuation of the various quantities at time $t = 15$ for this run are plotted in Figure 2.8. The most evident difference with respect to the previous case is that in this case phase-mixing is recovered. This can be seen looking for example at δB_x and δB_z component. This process is slower than what observed in the simulation by Vásconez et al. (2015) since the in-plane Alfvén velocity is smaller, due to the x component of $\mathbf{B}^{(0)}$ that is now reduced by a factor $\cos(\pi/4)$. Another particular feature of this configuration is that the evolution is not symmetrical any more respect to the line $y = \pi$. This lack of symmetry is a consequence of the nonvanishing $B_z^{(0)}$ component. In fact, considering the linearized HMHD Equations in the case of in-plane $\mathbf{B}^{(0)}$ ($\theta = 0$), and calculating all the terms on the RHSs of Equations (2.2) and (2.3) at the initial time, it is found that each component of the RHS has a well-defined symmetry (symmetrical or antisymmetrical) with respect to the line $y = \pi$. But, this property does not hold anymore if $\theta \neq 0$. This explains why the

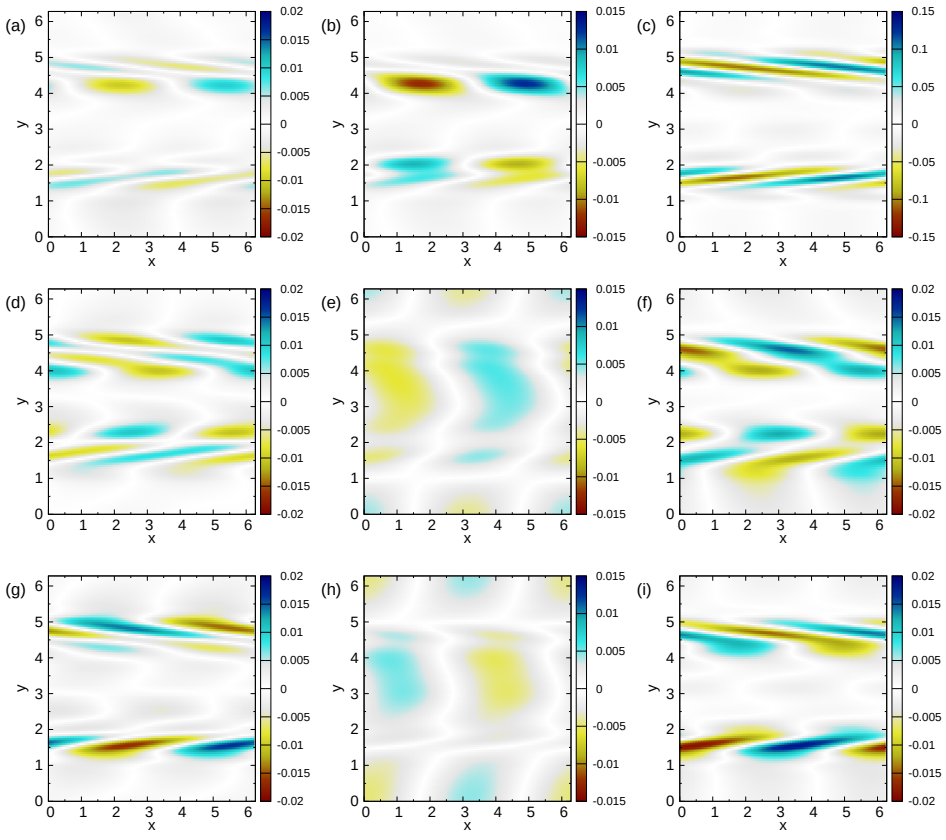

Figure 2.8: $\delta\rho$ (a), δT (b), δj_z (c), δv_x (d), δv_y (e), δv_z (f), δB_x (g), δB_y (h), δB_z (i) at time $t = 15.0$ (RUN 2).

results in the configuration corresponding to RUN 2 are not symmetric.

Similar as in the previous case, a localized perturbation in the x and z components of velocity and magnetic field perturbation develops in the two shear layers. In this case, such perturbations appear to be progressively stretched along an oblique direction, due to phase-mixing, so that the perpendicular wavevector tends to increase until it becomes of the order of $\tilde{\varepsilon}^{-1}$. We characterized the nature of the fluctuations that arise in the two shear regions. First, we estimated the value of the perpendicular wavevector as $k_\perp = 9.94$ at the time instant $t = 15$. Then we estimated the velocity of propagation in parallel and perpendicular direction. We did it through a similar approach as that used for RUN 1. We identified the minimum of δB_z in the space region where $4.0 < y < 5.0$ and followed its position for five computational times. Then, we linearly interpolated the x and y components of the position of the minimum as functions of time, finding the following two values for the propagation velocity along the x and y directions: $v_x = 0.8$ and $v_y = 2.2 \times 10^{-2}$. In order to compare these velocities with the predictions of the linear theory, the specific geometry of this configuration has to be taken into account. The background magnetic field direction is given by: $\hat{\mathbf{b}} = \cos\theta \hat{\mathbf{e}}_x + \sin\theta \hat{\mathbf{e}}_z$ and the direction of the wavevector is given by: $\hat{\mathbf{k}} = (k_x \hat{\mathbf{e}}_x + k_y \hat{\mathbf{e}}_y)/k$, where $k = \sqrt{{k_x}^2 + {k_y}^2}$. From the previous two equations we get $k_\parallel = k_x \cos\theta$ and, using the condition $k_y \gg k_x$, we can make the following approximation $k_\perp \simeq k_y$. Hence, the estimated velocities are $v_\parallel = v_x/\cos\theta \simeq 1.12$ and $v_\perp \simeq v_y \simeq 2.2 \times 10^{-2}$. By comparing these values with the linear modes group speeds $v_{g\parallel}$ and $v_{g\perp}$ (see Table 2.3), we found that the propagation velocity estimated from the simulation results is compatible with the KAWs group velocity, while it does not agree with the group velocity of FM and SM waves. We remark that the

Table 2.3: Frequency ω, group velocities $v_{g\parallel}$ and $v_{g\perp}$, and parallel phase velocity $v_{\phi\parallel} = \omega/k_\parallel$, for $k_\parallel = \sqrt{2}/2$, $k_\perp = 9.94$, $\beta = 1.25$, for kinetic Alfvén wave (KAW), fast magnetosonic (FM) and slow magnetosonic (SM) wave. The velocities values are normalized to the local Alfvén velocity.

	ω	$v_{g\parallel}$	$v_{g\perp}$	$v_{\phi\parallel}$
KAW	0.96	1.47	0.047	1.36
FM	14.88	0.11	1.49	21.04
SM	0.36	0.51	-0.016	0.51

values presented in Table 2.3 have been calculated using $\beta = 1.25$, which corresponds to the value at the center of the shear layers, where the perturbation is localized. The hodogram plotted in Figure 2.9 confirms the interpretation of the observed magnetic fluctuations as KAWs. It fact, it shows a polarization that turns clockwise when moving in the y direction, as expected from linear theory. We can conclude that also in this case the initial large amplitude Alfvén mode is locally converted into a KAW; in this case phase-mixing plays a role in the formation of small scales. The formation of transverse propagating fast waves is observed also in this case, but this phenomenom is less evident and plays a minor role in the dynamics of the physical system.

2.3.3 Kinetic effects

In this Section, we show the results of the kinetic simulations for the cases: in-plane $B^{(0)}$ (RUN 3) and out-of-plane $B^{(0)}$ (RUN 4). As in the HMHD cases, also here small-scale magnetic fields fluctuations form in the shear regions. Furthermore, since HVM simulations are nonlinear, the proton velocity distribution function (VDF) f displays non-Maxwellian features due to wave-particle interactions where these small-scale are present. To quantify these deformations, we computed the L^2–norm difference (Greco

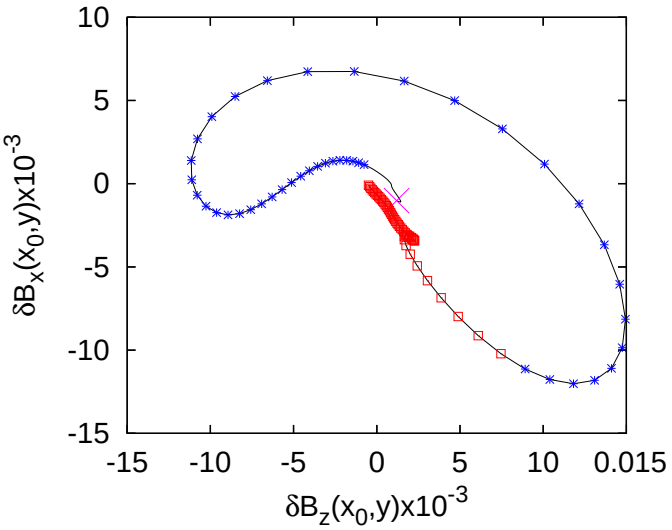

Figure 2.9: Hodogram of δB_z and δB_x for $\pi \leq y \leq 2\pi$ at $x = \pi$ and $t = 13.0$ (black line). The purple cross indicates the value at $y = \pi$, shear region values are plotted with blue asterisks and out of shear values with red squares (RUN 2).

et al., 2012):

$$\varepsilon(x, y, t) = \frac{1}{n}\sqrt{\int \left[f(\mathbf{x}, \mathbf{u}, t) - f_M(\mathbf{x}, \mathbf{u}, t)\right]^2 d^3\mathbf{u}} \tag{2.32}$$

where $f_M(\mathbf{x}, \mathbf{u}, t)$ is the Maxwellian distribution function associated with $f(\mathbf{x}, \mathbf{u}, t)$, constructed in a way that density, bulk velocity and total temperature of the two VDFs are the same. Figure 2.10 shows the evolution of $\varepsilon_{max}(t) = \max_{(x,y)\in D} \varepsilon(x, y, t)$ as a function of time. Red stars, black triangles and blue diamonds respectively indicate RUN 3, RUN 4 and, finally, the case performed by Vásconez et al. (2015), which has been included in Figure 2.10 for a better comparison.

In the case considered by Vásconez et al. (2015), $\varepsilon_{max}(t)$ smoothly increases and saturates at $\varepsilon^{sat} \simeq 0.035$. On the other hand in both RUN 3 and RUN 4 cases, $\varepsilon_{max}(t)$ rapidly increases for times $t < t_d \simeq 8$ (indicated

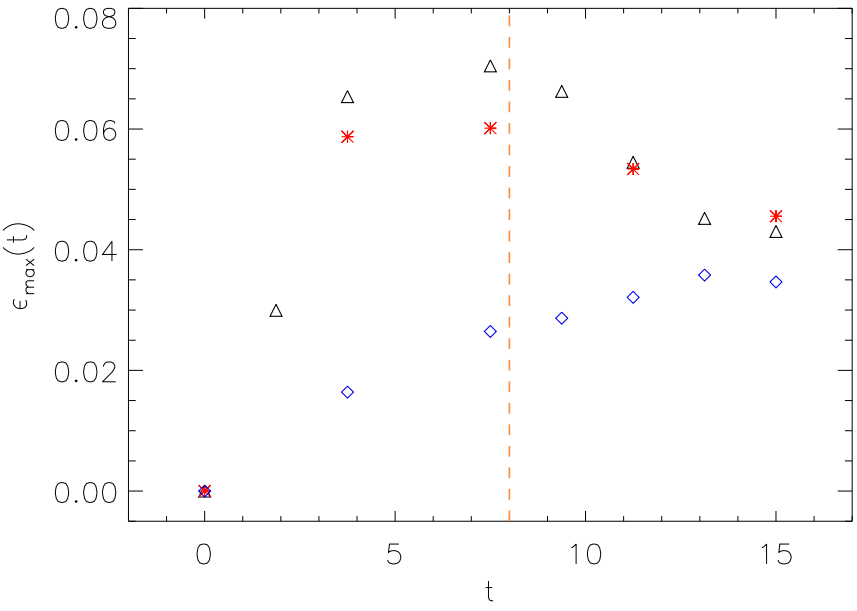

Figure 2.10: Quantity $\varepsilon_{max}(t)$ plotted as a function of time in Vásconez et al. (2015) (blue diamonds), RUN 3 (red stars) and RUN 4 (black triangles).

in Figure 2.10 with a orange dashed line) reaching values about two times bigger than ε^{sat}. Then, for $t > t_d$ it decreases and finally approaches a value comparable with ε^{sat}. We remark that t_d is the time necessary for the phase-mixing process to form transverse wavevectors comparable with $\tilde{d}_p^{-1}$ in Vásconez et al. (2015) configuration.

As well as for the case considered in Vásconez et al. (2015), KAW-like fluctuations produce modifications of the VDFs in both RUN 3 and RUN 4 cases. However, both the new cases of study suggest the presence of a transient period where kinetic effects are stronger compared to what observed by Vásconez et al. (2015). In order to characterize the nature of this transient and the nature of the asymptotic behavior, we analyze in detail two time instants: i) $t = 7.5$, which corresponds to the time where $\varepsilon_{max}(t) = \max_t \varepsilon_{max}(t)$ and is equivalent to $60\Omega_{cp}^{-1}$ and ii) that $t = 15$, which is the final instant of the simulation and corresponds to $120\Omega_{cp}^{-1}$. Figure 2.11 shows the 2D contour plots of $\varepsilon(x, y)$ at $t = 7.5$ (top panels) and $t = 15$ (bottom panels) as a function of x and y for the two runs. The intensity of $\varepsilon(x, y)$ is slightly smaller in the RUN 3 case compared with the RUN 4 case. Moreover, the $\varepsilon(x, y)$ shape is more structured in the RUN 3 case than in the RUN 4 case. Indeed in the in-plane $B^{(0)}$ case (RUN 3), at both $t = 7.5$ [panel (a)] and $t = 15$ [panel (c)], $\varepsilon(x, y)$ presents some ripples towards the external sides of the y domain. These deformations are clearly visible at $t = 15$ [panel (c)] where at least two strong regions of non-Maxwellianity are recovered. On the other hand, in the out-of-plane $B^{(0)}$ case (RUN 4), the region where $\varepsilon(x, y)$ is significantly not null is more uniform and confined within the shear. Moreover for both RUN 3 and RUN 4 cases, $\varepsilon(x, y)$ is not zero in two slab-like regions at $t = 7.5$ [see Figures 2.11(a)–(c)], while, at $t = 15$ [see Figures 2.11(b)–(d)], it is concentrated into bubble-like areas. We

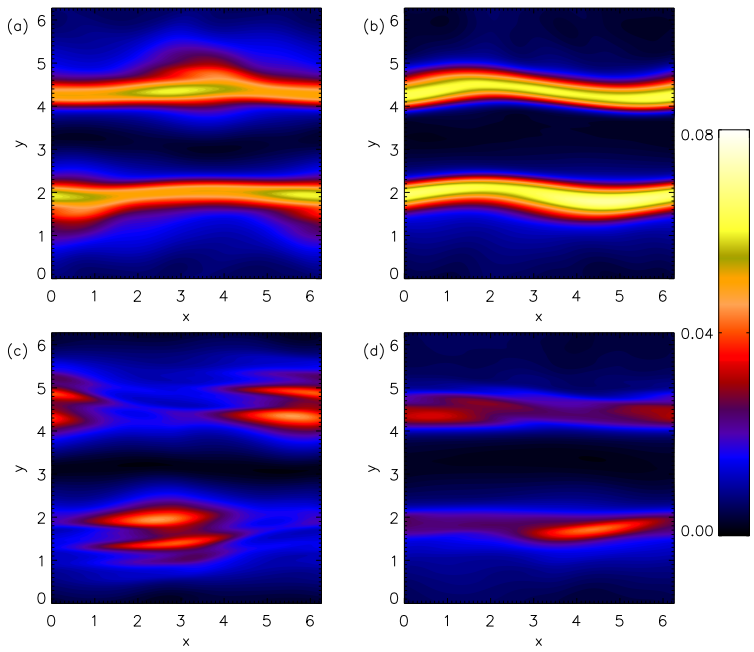

Figure 2.11: Contour plots of $\varepsilon(x, y)$ at time $t = 7.5$ (top panels) and $t = 15$ (bottom panels). Left column refers to RUN 3, while right column indicates RUN 4.

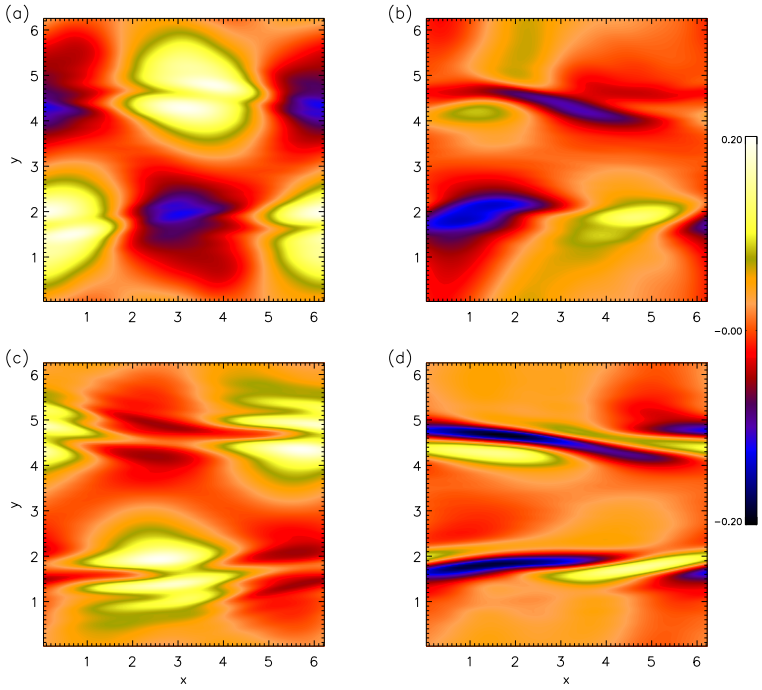

Figure 2.12: Contour plots of $R(x, y)$ at time $t = 7.5$ (top panels) and $t = 15$ (bottom panels). Left column refers to RUN 3, while right column indicates RUN 4.

suggest the following interpretation for these features: at $t = 7.5$ the large amplitude initial perturbation is interacting with the background structure modifying the VDFs in the shear layer. This interaction gives rise to the formation of KAWs that, at bigger times, remain the only actors responsible for the VDFs deformations. Indeed, the region where at time $t = 15$ the distribution function departs from the Maxwellian shape are associated with the presence of KAWs. Departures of the proton distribution function from the Maxwellian form can be also identified with the temperature anisotropy index (Perrone et al., 2013), $R(x, y, t) = 1 - T_{p\perp}(x, y, t)/T_{p||}(x, y, t)$, being $T_{p\perp}$ and $T_{p\|}$ respectively the proton perpendicular and parallel temperatures evaluated respect to the local magnetic field $\mathbf{B}$. Figures 2.12 shows instantaneous spatial distribution of $R(x, y)$ at $t = 7.5$ (top panels), and

at $t = 15$ (bottom panels); corresponding to RUN 3 (left panels) and RUN 4 (right panels). This figure confirms a previous result by Vásconez et al. (2015): KAWs produce both $R > 0$ and $R < 0$ regions, corresponding to anisotropic VDFs in the parallel and perpendicular directions. A clear correlation between the kinetic deformations of f and the spatial distribution of the index R is recovered and both the parameters R and ε recall the shape of the magnetic field fluctuations [see Figures 2.5(i) and 2.8(i)].

In order to display the effects of wave-particle resonances on the distribution function, we present in Figure 2.13 the 3D iso-surface plots ($f = 0.015$) of the VDFs for $t = 7.5$ (top panels) and $t = 15$ (bottom panels) taken at the spatial point where ε is maximum. Left panels refer to RUN 3, while right panels refer to RUN 4. In all cases, VDFs are clearly gyrotropic respect to the local magnetic field. Moreover at $t = 7.5$ VDFs presents deformations towards both positive and negative velocities [see Figures 2.13(a)–(b)], while, at $t = 15$, a single beam is present in the positive velocity direction [see Figures 2.13(c)–(d)]. At this time, the VDFs shape shares a lot of characteristics with the VDFs showed in Vásconez et al. (2015), such as rings perpendicular to the direction of local magnetic field and a beam directed in the parallel direction. In order to single out the VDFs non-Maxwellian features, we show in Figures 2.14(a–d) the 2D contour plots of the VDFs in the plane $u_B - u_{\perp B}$, being u_B and $u_{\perp B}$ respectively the parallel and perpendicular velocities respect to the local magnetic field direction. We remark that the VDFs showed in Figures 2.14(a–d) are the same of the ones showed in Figures 2.13(a–d). At $t = 7.5$ [top panels of Figures 2.14] two beam-like deformations are recovered in the VDFs for both positive and negative velocities. On the other hand, at $t = 15$ [bottom panels of Figures 2.14], a distinct proton beam is recovered in the distribution function shape in the

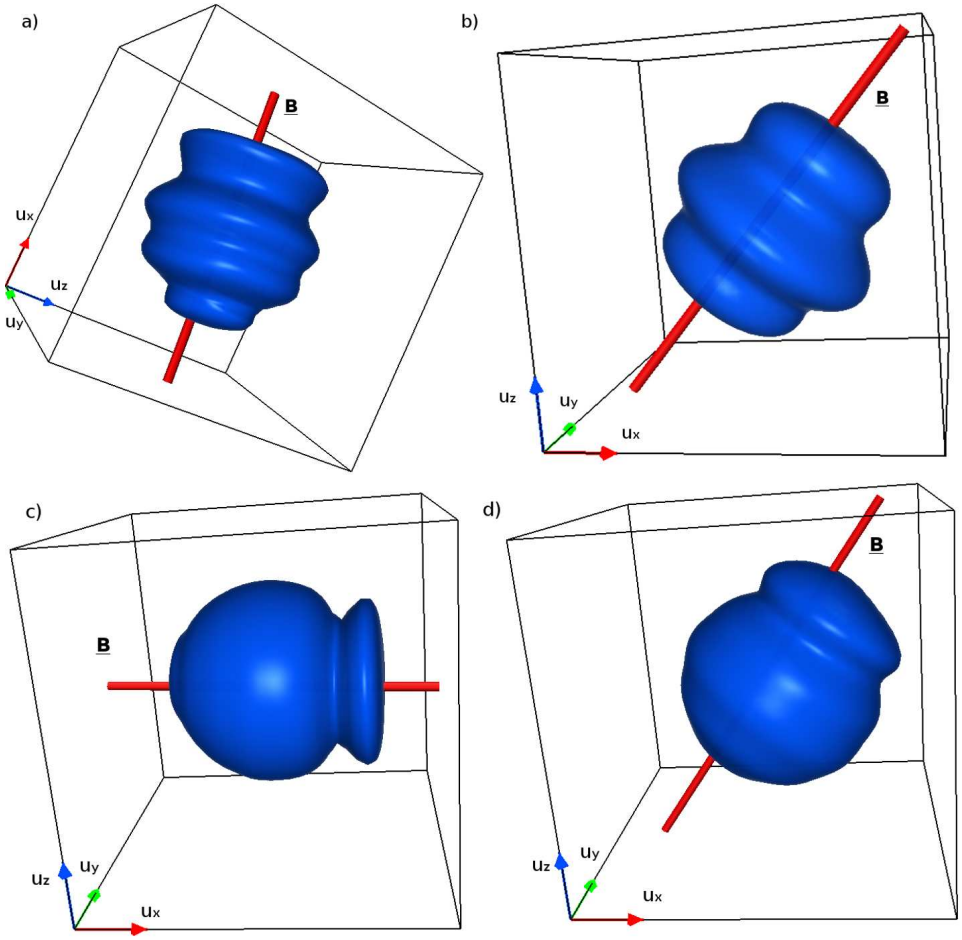

Figure 2.13: Three-dimensional iso-surface plot of the VDFs at time $t = 7.5$ (top panels) and $t = 15$ (bottom panels), where ε is maximum. Left column refers to RUN 3, while right column indicates RUN 4.

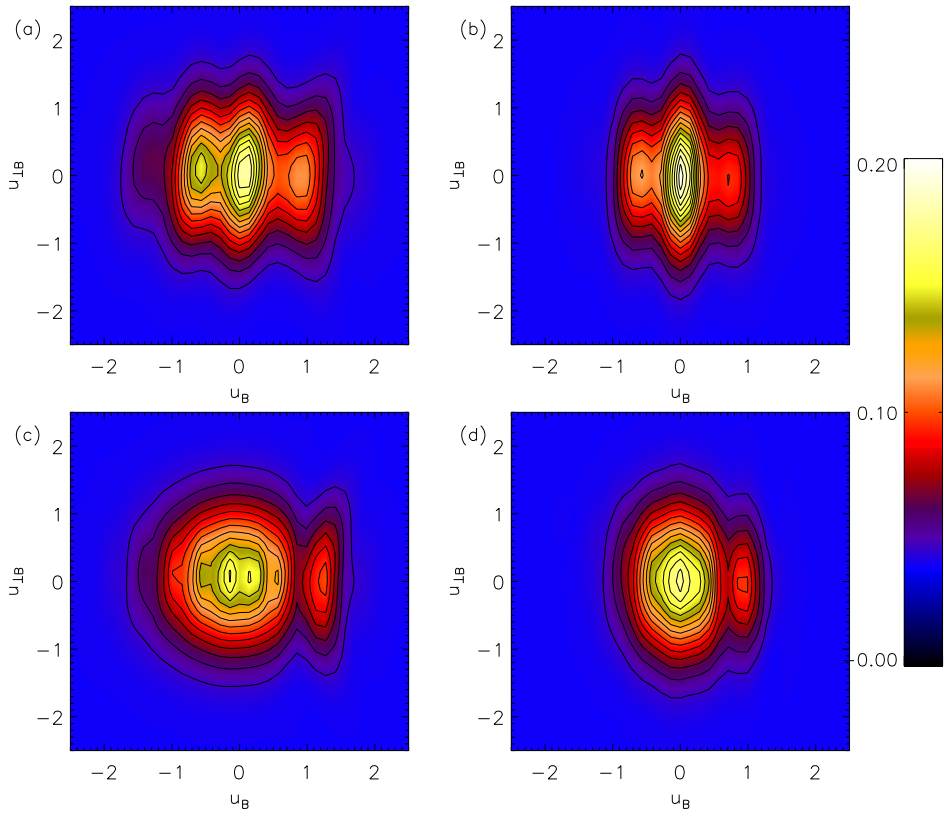

Figure 2.14: 2D iso-surface plot of the VDFs at time $t = 7.5$ (top panels) and $t = 15$ (bottom panels), where ε is maximum and in the plane $u_B - -u_{\perp B}$. Left column refers to RUN 3, while right column indicates RUN 4.

direction parallel to $\mathbf{B}$. Beam velocities $\{v_b \simeq 1.1$ for RUN 3 [panel (c)] and $v_b \simeq 1.5$ for RUN 4 [panel (d)]$\}$ are in good agreement with the linear theory values for the KAWs parallel group velocities presented in Tables 2.2–2.3, suggesting particle resonances with this kind of waves.

2.4 Discussion

In this chapter we have studied the evolution of an initial Alfvénic perturbation propagating in an inhomogeneous equilibrium pressure-balanced structure, in which the equilibrium quantities vary in a direction (y) perpendicular to the magnetic field $\mathbf{B}^{(0)}$ orientation. Dispersive and kinetic effects have been included using a HMHD and a HVM numerical model, respectively. The same problem has been already studied (Vásconez et al., 2015) in a particular case in which the initial perturbation wavevector $\mathbf{k}_0$ is parallel to $\mathbf{B}^{(0)}$ and the initial polarization is perpenducular both to $\mathbf{B}^{(0)}$ and to the inhomogeneity y direction. In the present paper we have generalized the results of Vásconez et al. (2015), considering two different initial conditions: in the first case (in-plane $\mathbf{B}^{(0)}$), k_0 is parallel to $\mathbf{B}^{(0)}$, but the polarization is along the inhomogeneity direction; in the second case (out-of-plane $\mathbf{B}^{(0)}$), k_0 is at an angle $\theta = \pi/4$ with $\mathbf{B}^{(0)}$, and the wave is polarized in the direction perpendicular to both k_0 and $\mathbf{B}^{(0)}$, which coincides with the inhomogeneity y direction. Both configurations are inherently different from that considered by Vásconez et al. (2015); in fact, during the time evolution, the coupling between the perturbation and the background inhomogeneity makes the local wavevector k to increase and rotate toward the y direction. Then, in both cases here considered, the initial polarization is no longer perpendicular to k with increasing time. This generates compressive fluctuations in the shear regions, whose amplitude is of the same order as

the initial Alfvénic perturbation. In constrast, in the case considered by Vásconez et al. (2015), the polarization remains perpendicular to k, i.e., the perturbation remains non-compressive, at least until the wavevector k becomes large enough to make dispersive effects no longer neglibible.

In the Vásconez et al. (2015) configuration, the results have shown that in the shear regions the initial Alfvén wave is subject to phase-mixing that gradually transform such a perturbation into a KAW. One of the aims of this study is to verify whether KAWs are generated also in the new considered configurations. In the in-plane $\mathbf{B}^{(0)}$ case, no phase-mixing has been found, similar to what observed in a purely MHD case (Malara et al., 1996); nevertheless, we have found the formation of KAWs in the shear regions. KAWs have been identified both comparing their propagation velocity with the group velocity of dispersive modes, and by considering their polarization. However, the transverse wavelength $\lambda_\perp$ of these perturbations is of the order of the shear layer width $2\pi h \sim 1$, i.e., it is slightly larger than those found in Vásconez et al. (2015). This indicates that a coupling between the initial wave and the background inhomogeneity, different from phase-mixing, is responsible for the KAW formation in this case. In our simulations the proton inertial length is $d_p = 0.125$ (in normalized units), so that $k_\perp d_p = 2\pi d_p/\lambda_\perp \sim d_p/h \simeq 0.6$, so that the perpendicular wavelength is comparable with d_p; this explains why dispersive effects, which characterize KAWs, play a major role in the observed dynamics. However, in a case where the proton inertial length were much smaller than the shear width, it remains unclear whether KAWs would form in the in-plane $\mathbf{B}^{(0)}$ configuration. In the out-of-plane $\mathbf{B}^{(0)}$ case, we observed that the perturbation is subject to phase-mixing, which generates fluctuations in the shear layers at scales even smaller than the shear layer width. Also in this case, such

flucuations have been identified as KAWs. The most general initial configuration for a linearly polarized Alfvén wave can be considered as a linear combination of the three case here discussed. Then, we conclude that when an Alfén wave propagates in transverse inhomogeneous structures, KAWs are eventually produced regardless of the initial wave polarization and of the propagation angle θ.

The large-amplitude simulations performed by the HVM model have shown that at KAW locations the ion distribution function is progressively modified with respect to the initial Maxwellian. Temperature anisotropies are generated, with $T_{||} > T_{\perp}$ or the reverse, according to the phase of the KAW. The shape of the distribution function reveals resonant wave-particle interactions. At locations where $T_{||}$ is particularly large, a beam of ions moving along the magnetic field in the propagation direction of the initial wave is observed.

These results have been derived within a simplified context, where it is possible to distinguish between a single well-defined wave an the inhomogeneous background. However, some indications about the possibility of generating KAWs in more complex situations, like in turbulence, can be deduced. In fact, the wave-inhomogeneity coupling considered in this study is of a similar nature as the nonlinear coupling between fluctuations which generates the turbulent cascade in MHD: the phenomenon we studied is closely related to the mechanism that favours perpendicular spectral transfer in the nonlinear cascade (Shebalin et al., 1983). Then, our results give a positive indication about the possibility to generate KAW-like fluctuations at proton scales within a turbulent cascade, as suggested by solar wind observations (Bale et al., 2005; Sahraoui et al., 2012).

Chapter 3

Particle dynamics in RMHD decaying turbulence

The heliospheric plasma is not in thermodynamic equilibrium. It is in fact populated by suprathermal particles whose energies are sometimes even relativistic. Particle energization in the heliosphere happens for example in the solar corona during solar flare events, but also in the interplanetary shocks, near coronal mass ejections, and in planetary magnetosphere. The mechanisms responsible for the acceleration of particles are still in debate (see, e.g., Reames (1999); Verkhoglyadova et al. (2015)). Processes related to turbulence has been proposed to be contributors to mechanisms that drive particle acceleration. Turbulence is a phenomena that involves interaction among structures at different scales with a net energy cascade from larger to smaller scales. When turbulence is at play the electromagnetic field is not random in space, but the turbulent dynamics organizes the fluctuations in coherent structures like magnetic islands, flux tubes and current sheets (Greco et al., 2009). When a particle encounters one of these current sheets produced by turbulence, it can be accelerated especially if this current sheet

is associated with a magnetic island or a flux tube where the particle can be trapped, and if the electric fields in or near the current sheet are enhanced by ongoing flux pileup or magnetic reconnection (Ambrosiano et al., 1988). The latter effect is thought to be particularly important in explosive events in the corona, such as flares and coronal mass ejections, in which the energy released is provided by magnetic reconnection. During an event of magnetic reconnection magnetic energy is converted into fluid motion and also to particle acceleration (Priest and Forbes, 2007). In a turbulent medium many magnetic reconnection events happens in the vicinity of X-points, i. e. those points where the magnetic field is zero and the magnetic lines near that point are X shaped (Wan et al., 2013). Another mechanism that can be responsible for particles acceleration in the corona and in the heliosphere is the interaction of particles with waves (Hollweg and Isenberg, 2002; Cranmer and van Ballegooijen, 2003; Gary & Nishimura, 2004). An example of such a mechanism has been given in the previous chapter of this thesis where we have shown that KAW propagating in a plasma can generate a beam of accelerated particles in the direction parallel to the background magnetic field. Usually particle acceleration in particle-wave interactions are associated with resonances phenomena, so in order to have acceleration the typical spatial and time scale of variation of particle motion, like gyroradius and gyroperiod, have to be comparable to the scale of variation of the waves. This two mechanism, turbulence and waves, are not in contradiction to one another; they coexist and can both contribute to acceleration.

The mechanism for acceleration proposed in the present section is related to turbulence. We present results from test particle simulations in a 3D reduced version of magnetohydrodynamics in a plasma where turbulence activity is started by large scale perturbation present at the initial time and

then decays in time. When turbulence has evolved and formed coherent structures particles are placed in the system and their trajectory is then followed for a few non linear times during which the turbulence continues to evolve and decay.

First we describe the reduced MHD model and simulations and how to use results from this model in test particle simulations. Then we describe the set up of test particle simulations and we show preliminary results on energization, particle velocity distribution function and the influence that the Reynolds number of the fluid model considered can have on particle acceleration. Finally we discuss the results obtained and compare them to previous works.

3.1 From Reduced MHD to test particle simulations

Many heliospheric plasmas, for example solar corona, are permeated by a strong large scale magnetic field. In this kind of plasmas, in which the turbulence can be considered quasi-2D, the parallel gradients of the turbulent fluctuations with respect to the background magnetic field are small compared to the perpendicular gradients. In such a physical situation a good description of the dynamics has been proposed to be a reduced version of classical Magnetohydrodynamics (MHD) called Reduced MHD (RMHD). The RMHD model has been widely studied theoretically (Strauss, 1976; Montgomery, 1982; Zank and Matthaeus, 1992) and applied to the study of coronal heating in open fieldline regions (Oughton et al., 2001) and in coronal loops dynamics (Rappazzo et al., 2007, 2008). In order to derive RMHD equations one has to make the following assumptions. The back-

ground magnetic field is homogeneous and its intensity is much stronger than the intensity of turbulent fluctuations, the typical scale of variation of the fluctuations in the direction parallel to the background magnetic field is much larger than the parallel scale. Furthermore only low frequency dynamics is considered and therefore magnetosonic activity is eliminated by suppressing fluctuations with polarization parallel to the background field; therefore in the leading order the plasma is incompressible. If we suppose that the strong guide field $\mathbf{B_0}$ is directed in the z direction, the RMHD equations in non dimensional form read:

$$\frac{\partial \bar{\mathbf{V}}}{\partial t} + \left(\bar{\mathbf{V}} \cdot \nabla\right) \bar{\mathbf{V}} = -\nabla P + \left(\bar{\mathbf{B}} \cdot \nabla\right) \bar{\mathbf{B}} + c_a \frac{\partial \bar{\mathbf{B}}}{\partial z} + \frac{1}{Re} \nabla^2 \bar{\mathbf{V}} \tag{3.1}$$

$$\frac{\partial \bar{\mathbf{B}}}{\partial t} + \left(\bar{\mathbf{V}} \cdot \nabla\right) \bar{\mathbf{B}} = \left(\bar{\mathbf{B}} \cdot \nabla\right) \bar{\mathbf{V}} + c_a \frac{\partial \bar{\mathbf{V}}}{\partial z} + \frac{1}{Re_m} \nabla^2 \bar{\mathbf{B}} \tag{3.2}$$

$$\nabla \cdot \bar{\mathbf{V}} = \nabla \cdot \bar{\mathbf{B}} = 0 \tag{3.3}$$

where $\bar{\mathbf{B}}$ is the magnetic field normalized to a typical value of magnetic field fluctuation δb, $\bar{\mathbf{V}}$ is the fluid velocity normalized to the typical value of velocity fluctuations δv, P is the sum of the magnetic and kinetic pressure normalized to δb^2, c_A is the Alfvén velocity normalized to $\delta b/\sqrt{4\pi\rho_0}$ (where ρ_0 is the plasma mass density), lengths are normalized to a typical length in the direction perpendicular to the background magnetic field $L_\perp$, t is normalized to the non linear time $t_{nl} = L_\perp/\delta v$. Moreover, the gradients and Laplacian in Equation (3.1)-(3.3) are directed in the xy plane, along with the fluctuating components of the magnetic and velocity fields. (Recall that magnetic and velocity fluctuations directed in the parallel direction would represent magnetosonic activity). Finally, Re and Re_m are the kinetic and

magnetic Reynolds numbers given by:

$$Re = \frac{\rho_0 L_\perp \delta v}{\nu}, \qquad Re_m = \frac{4\pi L_\perp \delta v}{\eta c^2} \tag{3.4}$$

where ν is the dynamic viscosity and η is the resistivity. In Equations (3.1)-(3.3) the magnetic field and velocity field have the form:

$$\bar{\mathbf{B}}(x, y, z, t) = \mathbf{B}_0 + \mathbf{b} = (b_x, b_y, B_0) \tag{3.5}$$

and

$$\bar{\mathbf{V}}(x, y, z, t) = (\mathbf{V}_x, \mathbf{V}_y, 0). \tag{3.6}$$

where B_0 is the magnitude of the guiding field and b_x, b_y and v_x, v_y are the magnetic and velocity fluctuations in the perpendicular direction. An important parameter in RMHD is the Kubo number K defined as:

$$K = \frac{\delta b}{B_0} \frac{L_\parallel}{L_\perp} \tag{3.7}$$

where $L_\parallel$ is the typical scale in the parallel direction and the relation $L_\parallel \gg L_\perp$ holds (for further discussion of the role of Kubo number see, e.g., Shalchi (2015)). In the cases we are going to consider the Kubo number is set equal to 1.

Test particle simulations consist of evolving the trajectory of a charged particle in an electromagnetic field, solving the Lorentz equations, here reported in cgs units:

$$\frac{d\mathbf{r}}{dt} = \mathbf{v}, \tag{3.8}$$

$$\frac{d\mathbf{v}}{dt} = \frac{q}{m}\left(\frac{\mathbf{v}}{c} \times \mathbf{B} + \mathbf{E}\right). \tag{3.9}$$

Here $\mathbf{r}(t)$ is the particle position at time t, $\mathbf{v}(t)$ is particle velocity at time

t, q is the particle charge, m is the particle mass, $\mathbf{B}(\mathbf{r}(t), t)$ and $\mathbf{E}(\mathbf{r}(t), t)$ are the magnetic and electric field, and c is the speed of light. In order to solve Equations (3.8)-(3.9) the electric and magnetic field have to be provided externally in some way. One way is using a synthetic model that defines the fields at each time and position. An example of this approach can be found in the next chapter of this thesis. The other possibility is to use data from numerical simulations defined on a spatial and temporal grid. This approach has been widely used in literature both using data obtained in MHD simulations (Ambrosiano et al., 1988; Dmitruk et al., 2003a; Turkmani et al., 2005) and RMHD data (Dalena et al., 2014). Since simulations data are usually defined on a spatial grid and represented in discrete time steps, in a test particle code the values of these fields have to be interpolated in space and time in order to get the actual values of $\mathbf{E}$ and $\mathbf{B}$ at $r(t)$ at time t. Another crucial operation is to translate the value of the field coming from simulation, and so defined in certain "code units", to the units of the test particle code. How we did the last operation is explained in the following. First of all the expression of the electric field in RMHD, in dimensional form, is:

$$\mathbf{E}(x, y, z, t) = -\frac{\mathbf{V} \times \mathbf{B}}{c} + \eta \mathbf{J}, \tag{3.10}$$

where η is the resistivity, and $\mathbf{J} = \frac{c}{4\pi} \nabla \times \mathbf{B}$ is the current. This makes Equation (3.9) become:

$$\frac{d\mathbf{v}}{dt} = \frac{q}{m} \left(\frac{\mathbf{v}}{c} \times \mathbf{B} - \frac{\mathbf{V} \times \mathbf{B}}{\mathbf{c}} + \eta \mathbf{J} \right). \tag{3.11}$$

Then we normalized the dimensional quantities using RMHD normalization quantities in the following way: $\mathbf{v} = \delta v \tilde{\mathbf{v}}$, $\mathbf{b} = \delta b \tilde{\mathbf{b}}$, $t = t_{nl} \tilde{t}$, $\mathbf{J} = \delta b / (L_\perp c) \tilde{\mathbf{J}}$ and $\eta = L_\perp \delta v / c^2 \tilde{\eta}$, where all "$\sim$" values represent now variables written in

the test particle code unit. Substituting in the Lorentz Equations we get:

$$\frac{L_\perp}{\frac{L_\perp}{\delta v}} \frac{d\tilde{\mathbf{r}}}{d\tilde{t}} = \delta v \tilde{\mathbf{v}}, \tag{3.12}$$

$$\frac{\delta v^2}{L_\perp} \frac{d\mathbf{v}}{dt} = \frac{q\, \delta b\, \delta v}{mc} \left(\tilde{\mathbf{v}} \times \tilde{\mathbf{b}} - \tilde{\mathbf{V}} \times \tilde{\mathbf{B}} + \tilde{\eta} \tilde{\mathbf{J}} \right). \tag{3.13}$$

Simplifying common factors and dropping the "$\sim$" yields to two simple nondimensional equations:

$$\frac{d\mathbf{r}}{dt} = \mathbf{v}, \tag{3.14}$$

$$\frac{d\mathbf{v}}{dt} = \alpha \left(\mathbf{v} \times \mathbf{B} - \mathbf{V} \times \mathbf{B} + \eta \mathbf{J} \right), \tag{3.15}$$

with

$$\alpha = \frac{q\, \delta b\, L_\perp}{m\, c\, \delta v}. \tag{3.16}$$

Using the relation $\delta b / B_0 = \delta v / v_A$, which is true for purely Alfvénic fluctuation, and approximately true for RMHD, it is possible to write α in this way:

$$\alpha = \frac{L_\perp}{d_p},$$

where $d_p = (qB_0/mc)v_A$ is the ion inertial length. Consequently α in a turbulence picture is a parameter that measures the ratio between the large scale where energy is injected and the small scale where energy is dissipated. If coronal parameter are used $\alpha \simeq 10^5$. Such a broad band scale resolution is not achievable in numerical simulations, so using such a value of α in our simulation would not be consistent with the turbulence RMHD model. In order to be consistent with the RMHD simulations we identify the dissipation scale in the RMHD model with d_p. When turbulence is present, then one can therefore relate the ion inertial scale and energy containing scale to

the Reynolds number (Matthaeus et al., 2005) using the relation

$$d_p = L_\perp Re^{-3/4},$$

and consequently one finds that

$$\alpha = Re^{3/4}.$$

In this way we obtained an expression for α that depends only on the RMHD Reynolds number and scales with the resolution of RMHD simulations. In the next section we present briefly the RMHD simulations from which magnetic and electric field data are obtained and then we display all the results related to the test particle simulations performed.

3.2 Numerical simulations and results

The initial conditions of RMHD simulations are set in order to generate a turbulent cascade. Large scale modes are superposed to the background magnetic field at the beginning. At $t = 0$ the typical mean square values of velocity and magnetic fluctuations are $v^2 = b^2 = 1$ with a cross helicity $\sigma_c = 0.015$. Excited wavevectors have $4 \leq k_\perp \leq 15$ with approximately equal energy in each k_z, where $k_\perp$ and k_z are the wavevectors in perpendicular and parallel direction, respectively. The initial values of k_z go from 0 to 5. The spectrum knee due to this fluctuations is at $k_0 = 6$ with an asymptotic high-k slope $q = -2.333$. Periodic conditions are imposed at the boundaries, the computational domain in test particle code unit is $D(x, y, z) = [0, 2\pi] \times [0, 2\pi] \times [0, 20\pi]$, and the background magnetic field intensity is $B_0 = 10$. The spectral magnetic and kinetic energy is the same

for each mode and the modes have random phases. In less than one non linear time turbulence develops in the computational domain forming coherent structures like current sheets, then as the time passes, these structures are dissipated by resistivity. There is no external forcing applied on the plasma; rather the energy is supplied only by the initial perturbation. We used data from different simulations where we changed the Reynolds number keeping the same large scale configuration at the beginning. The number of grid points used along with Reynolds numbers and corresponding α are reported in Table 3.1. We used data sampled from RMHD simulation with a time

n_x	n_y	n_z	η, ν	Re	α
256	256	128	5×10^{-3}	200	53.18
512	512	256	2.2×10^{-3}	454.54	98.44
1024	1024	256	1.2×10^{-3}	833.33	155.10

Table 3.1: Number of point and Reynolds numbers in RHMD simulations, and corresponding α value is test particle simulation.

spacing of 0.1 non linear time. 10^5 particles are injected at time $t = 0.5$ when turbulence is at play and their trajectories are followed for 3 non linear times up to $t = 3.5$. The particles are placed in random position with a specified initial speed and random directions. We performed runs for initial speed $v_i = 0$, $v_i = 1$ (the typical turbulent velocity), $v_i = 10$ (the typical Alfvén velocity) and $v_i = 100$. Electric and magnetic field are interpolated in space and linearly interpolated in time. The time step is chosen in order to resolve the particle gyromotion along the background magnetic field. We first present results obtained for simulations with the smallest values of α, i.e. $\alpha = 53.18$. These results do not change qualitatively, for the values of α used in this work, when the value of α is changed. The effects of varying α are discussed later. In Figure 3.1 the PDFs of the particle energies are plotted for a selection of times, for cases with different initial particle

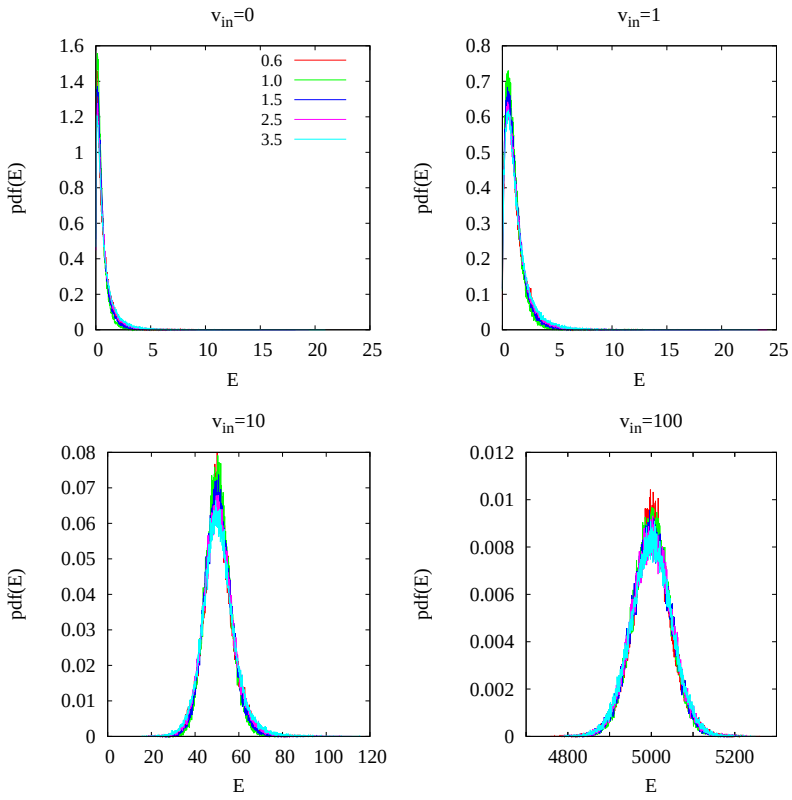

Figure 3.1: Energy PDFs at different times, for different initial velocities: $v_i = 0$ (top left), $v_i = 1$ (top right), $v_i = 10$ (bottom left), $v_i = 100$ (bottom right).

speeds. We can see that for every initial condition, particles are energized. This effect is more evident when the initial velocity is small. In Figure 3.2 the PDF of perpendicular velocity are shown. If we look at the case when $v_i = 0$, we can see that the width of the PDF of particle velocity in the perpendicular directions shrinks as time goes on. This effect even if less evident, because of the larger initial velocity, is present also in the other cases. We will try to give an explanation to that later. The evolution of parallel velocity PDFs, showed in Figure 3.3 is completely different. As the time goes on the tail of the parallel velocity PDFs extend to larger values for both positive and negative velocities. We believe that this behavior is

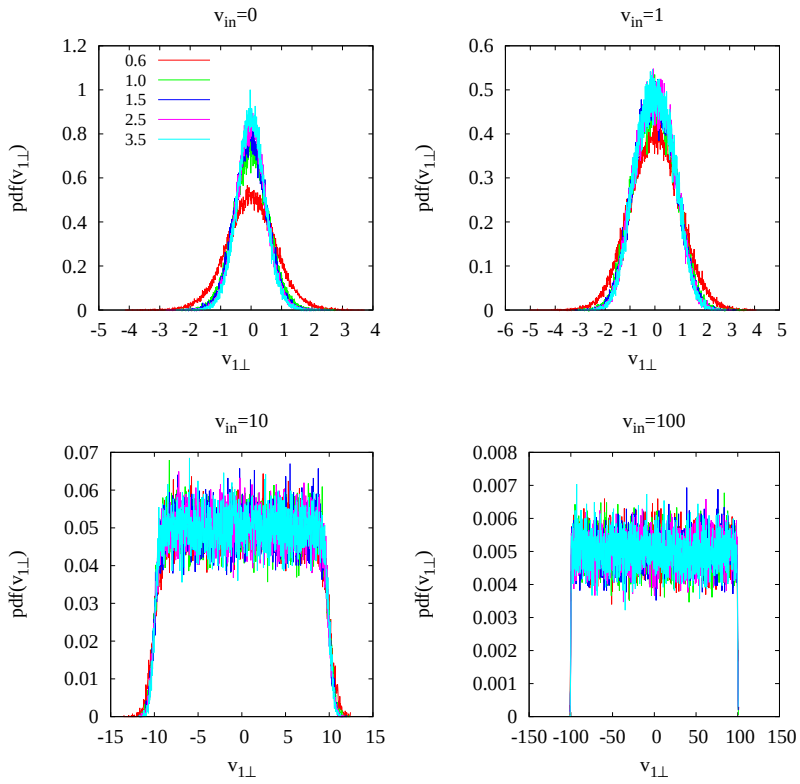

Figure 3.2: Perpendicular velocity (x-direction) PDFs at different times, for different initial velocities: $v_i = 0$ (top left), $v_i = 1$ (top right), $v_i = 10$ (bottom left), $v_i = 100$ (bottom right).

due to the parallel electric field given by current sheets that can accelerate particles in both directions depending on the sign of the current. This effect is less evident when the initial velocity is larger. This is due to the fact that particle with larger velocities cannot stay on a current sheet for a long period, because they are fast, and so they interact with current sheets for a very short time, and because their Larmor radius is large compared to the typical current sheet thickness. The fact that particle are accelerated more in parallel than in perpendicular direction is confirmed by Figure 3.4. In Figure 3.4 the 1% most energetic particles distribution functions are plotted for different times for each different initial conditions. We can see that the

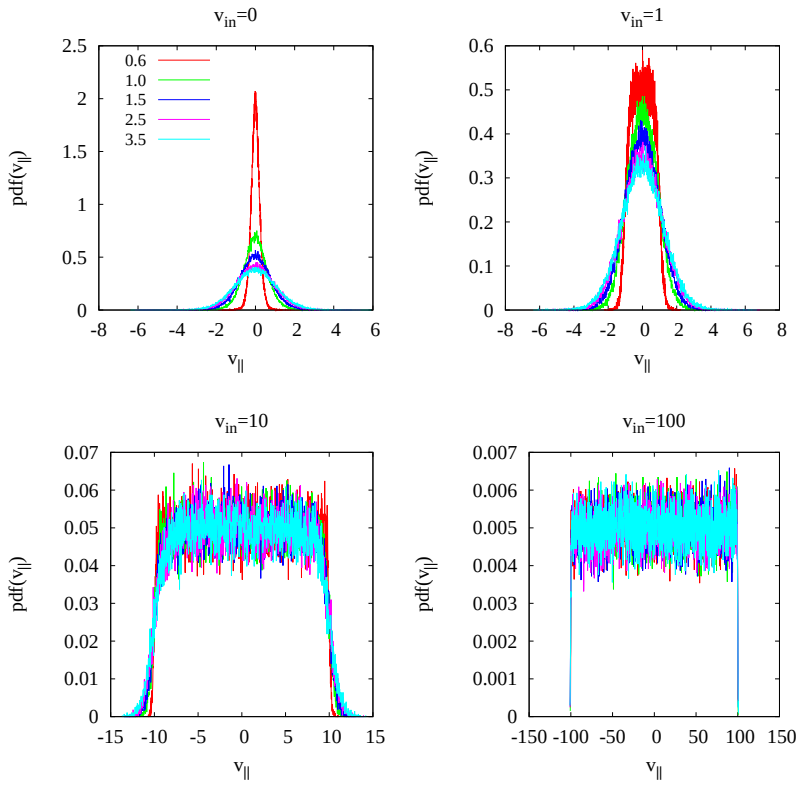

Figure 3.3: Parallel velocity PDFs at different times, for different initial velocities: $v_i = 0$ (top left), $v_i = 1$ (top right), $v_i = 10$ (bottom left), $v_i = 100$ (bottom right).

distribution functions are elongated in the direction of the parallel velocity when the initial speed is small compared to the Alfvén speed, in the other two cases they are more isotropic, but none of the most energetic particles is found to have a small parallel velocity. We can also see that as time goes on the distribution function, especially when the initial speed is low, moves to higher values of $v_\parallel$ without expanding in $v_\perp$. The effect of varying α is showed in Figure 3.5 where the average energy per particle in function of time is plotted. We can see that when α is bigger particles are more energized on average. This result is interesting because when α becomes bigger the Reynolds number is increasing and the resistivity is decreasing. One of

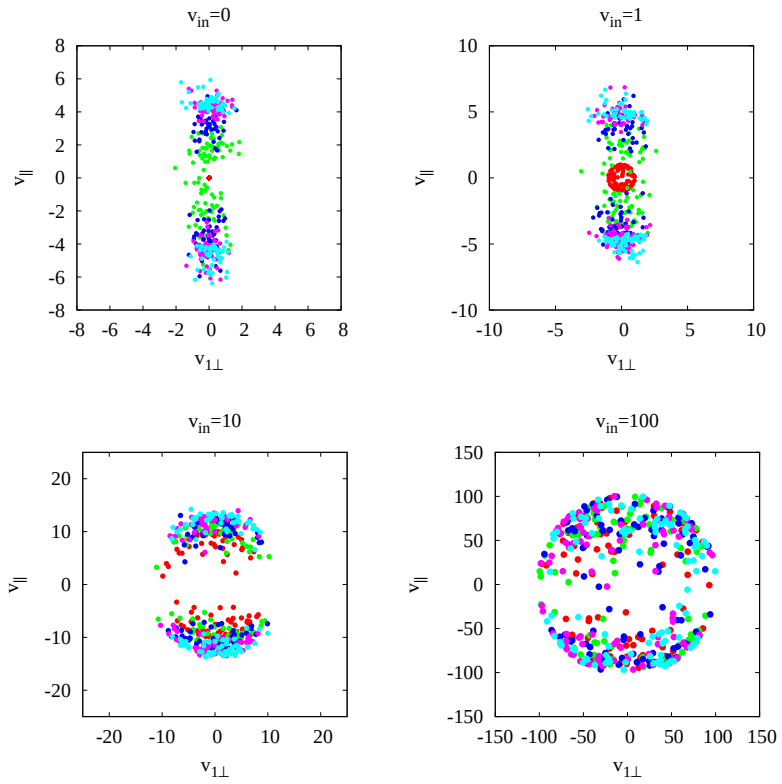

Figure 3.4: Velocity distribution function of the 1% most energetic particles at different times, for different initial velocities: $v_i = 0$ (top left), $v_i = 1$ (top right), $v_i = 10$ (bottom left), $v_i = 100$ (bottom right).

the limitation of our model is, in fact, that the value of resistivity, that is related to the Reynolds number, is very far from the physical values that one can find for example in solar corona. This non physical resistivity can be responsible for non realistic parallel acceleration. In our case even if the resistivity becomes lower the average energization increases. We have also to say that this bigger energization does not happen in the same physical time since the non linear times increases with α. It is interesting also to focus on energization at the very initial time. The observed oscillating behavior of Figure 3.5 is zoomed in Figure 3.6, for the case $v_i = 0$ (the other cases show the same behavior). We can see how the average energy oscillates between

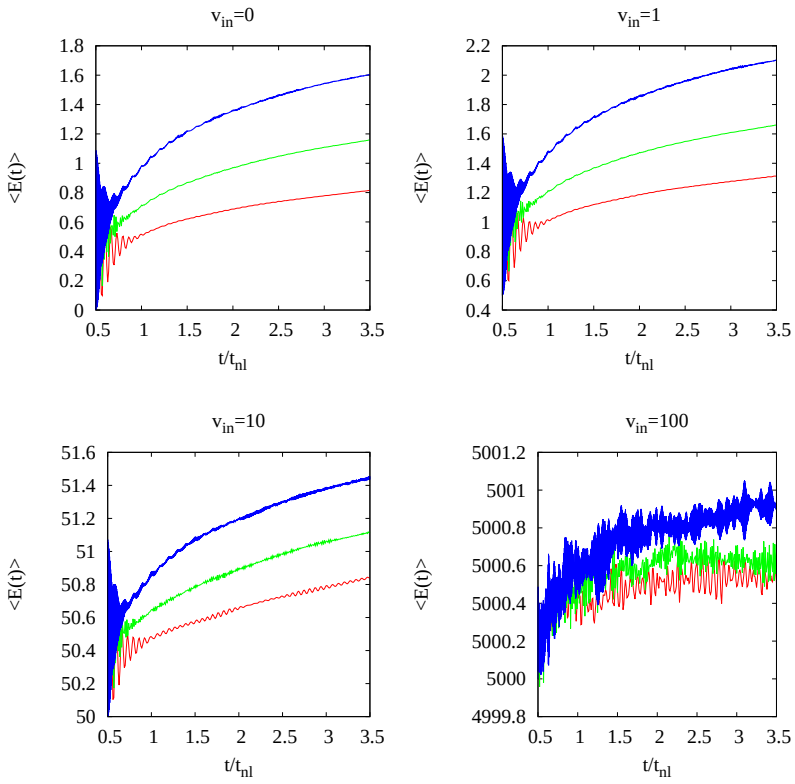

Figure 3.5: Average particle kinetic energy in function of time for $\alpha = 53.18$ (red), 98.44 (green), and 155.10 (blue).

$< E >= 0$ and $< E >= 0.8$. This happens because when particle are placed in the system they are immediately affected by the $\mathbf{E} \times \mathbf{B}$ drift, where

$$\mathbf{E}_\perp \approx -\mathbf{V} \times \mathbf{B} \tag{3.17}$$

is the inductive electric field associated with RMHD dynamical activity, and $\mathbf{B}$ is, at the leading order, the background magnetic field. The drift velocity is given by:

$$v_d = \frac{\mathbf{E}_\perp \times \mathbf{B}}{\mathbf{B}^2} \tag{3.18}$$

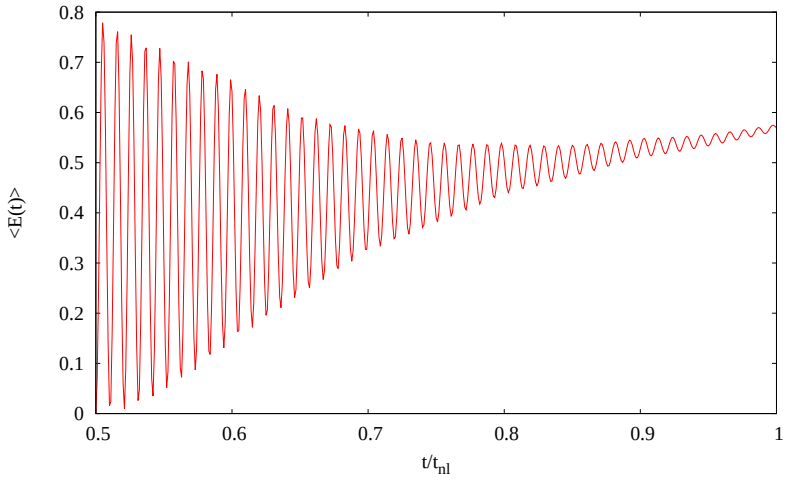

Figure 3.6: Particle avarage energy during the pick-up process.

and the energy associated to the drift is $E_d = \delta v^2/2$, that is comparable to the average of the two values between which the energy oscillates. Moreover the period of energy oscillation is the same of the typical particle gyroperiod and this confirms that $\mathbf{E} \times \mathbf{B}$ drift is actually at play. When the particles start gyrating their phases are coherent, but eventually after half non linear time this coherency is lost and energy starts growing without oscillating. The $\mathbf{E} \times \mathbf{B}$ can be responsible for the shape of perpendicular velocity PDF. In fact if these PDF are due to the drift the reason why they shrink can be explained by the decaying of turbulent fluctuation amplitudes. In order to evaluate how much energy, not due to the initial pick-up process, is gained on average by a particle we plotted in Figure 3.7 the gained energy $< \Delta E(t) >$ defined as:

$$< \Delta E(t) >=< E(t) >_T - E_d - E_i$$

where E_d is the energy associated to the drift and E_i is the initial energy. Particle with smaller initial speed are on average more energized and this is

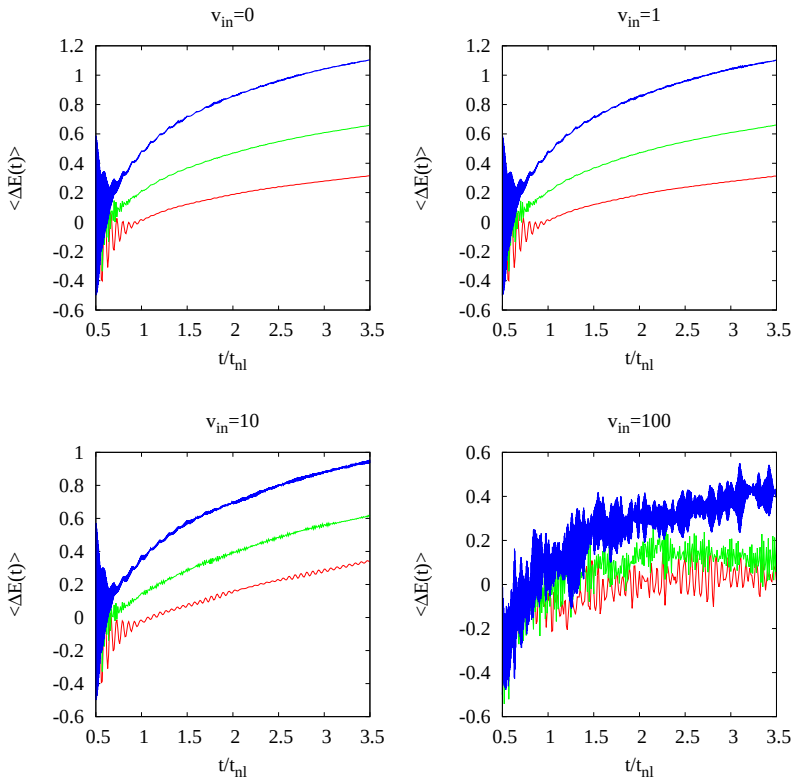

Figure 3.7

in accordance with what we said previously about the weaker interaction of faster particles with current sheets. Finally in Figure 3.8, the average power transferred to a single particle averaged on the last non linear time is plotted in function of α. Also this quantity increases with increasing α suggests that larger systems will more greatly energize particles. The important question, concerning how this increased energization scales to very large, physically relevant astrophysical systems, will be more deeply investigated in future works.

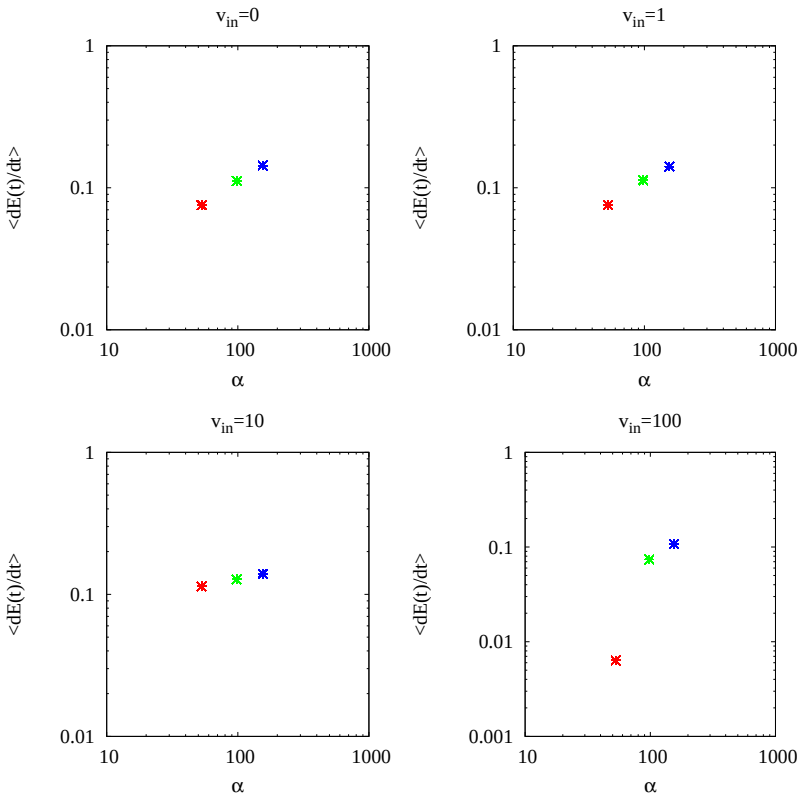

Figure 3.8: Average power transferred to a single particle averaged on the last non linear time ($2.5 \leq t \leq 3.5$ for $\alpha = 53.18$ (red), 98.44 (green), and 155.10 (blue)).

3.3 Discussion

The preliminary results of this work on particle acceleration in 3D RMHD decaying turbulence have shown that particles are preferentially accelerated in the parallel direction. This phenomenon is due to the presence of current sheets where a strong electric field parallel to the background magnetic field $\mathbf{B_0}$ is present. Particles with an higher initial velocity, that also have a bigger Larmor radius, weakly interact with these coherent structures and are less energized on average. When particles are injected in the system they are immediately subject to a drift caused by the electric field perpendicular to $\mathbf{B}_0$ given by the turbulent perpendicular fluctuations. The energy associated

to this drift is of the order of the fluctuations energy. The pick-up process makes particle gyrating in phase at the very initial times, then this coherent phenomenon vanish because of the electric field change in space and time. The $\mathbf{E} \times \mathbf{B}$ drift shapes the PDF of perpendicular velocity. We considered also the effect of varying the Reynolds number. As we showed previously, Reynolds number is connected to the value of α, the constant appearing in the rhs in Equation 3.15, by the Equation

$$\alpha = Re^{3/4}. \tag{3.19}$$

An increasing Reynolds number means an increasing α. If we suppose that in our experiment the same particle are considered, and so q/m is fixed, and that the typical level of fluctuations considered δv and δb are kept the same for each RMHD numerical experiment, the value of α depends only on the box size. The results of our test particle numerical simulations show that particles are more energized in bigger boxes in time comparable to the typical system non linear times. It is also important to notice that when α increases resistivity goes down, approaching a more realistic physical value. We have also shown that the average power transferred to particles increases with α. It is interesting to compare our results with the results obtained by Dmitruk et al. (2004). In that work numerical experiments of test particle energization in turbulent magnetic and electric fields obtained from pseudospectral direct numerical solutions of compressible three-dimensional MHD equations with a strong background magnetic field were presented. The authors found that in the configuration considered electrons were more accelerated in the parallel directions and protons in the perpendicular direction. The second of these results seems to be in contrast to what was

found in the numerical experiments here presented. The two configuration, our and the one from Dmitruk et al. (2004), are somewhat similar from a physical point of view, since a strong background magnetic field is present in both cases. Nevertheless there are differences that can play an important role. The first one is that in our case electric and magnetic field are changing in time, while instead, in Dmitruk et al. (2004), a static field is considered. Another important feature that makes our case different from the other is that in RMHD approximations the effect of compressibility is completely ruled out. This effect is instead present in a full MHD model, along with the presence of fluctuations in the direction parallel to $\mathbf{B}_0$. The different results found in the two cases may well be specifically associated with one of these differences in the models; however, the clarification and validation of this hypothesis will be left to future work on this problem.

Chapter 4

Particle diffusion in synthetic turbulence

The transport of energetic particles in the heliosphere and in solar plasmas where turbulence is present is an important but difficult problem of astrophysics. Understanding transport is relevant for electron transport in solar coronal loops (Galloway et al., 2006), for particle transport parallel to the magnetic field in the solar wind, where regimes ranging from scatter free (or ballistic) to diffusive (determinated by pitch angle diffusion) are reported (Lin, 1974; Dalla et al., 2003; Zhang et al., 2003; McKibben, 2005; Perri and Zimbardo, 2007, 2009), and for the transport and the acceleration of cosmic rays, which sensitively depends on the "diffusion" induced by turbulence (Duffy et al., 1995; Perri and Zimbardo, 2012a; Zimbardo and Perri, 2013; Lazarian and Yan, 2014).

In this chapter we concentrate on transport induced by magnetic turbulence: this is one of the main factors influencing energetic particle transport in astrophysical plasmas. Basically, magnetic fluctuations give rise to a random walk of magnetic field lines which causes the cross field transport of

plasma particles, and, for the strong fluctuation levels and large Larmor radii found in astrophysical plasma, to non adiabatic changes of parallel velocity corresponding to pitch angle diffusion. Many studies have addressed these issues, both from the theoretical (Giacalone and Jokipii, 1999; Pommois et al., 2001; Teufel and Schlickeiser, 2002; Matthaeus et al., 2003; Shalchi et al., 2004) and from the observational point of view (Reames, 1999; Mazur et al., 2000) but a clear understanding is still lacking.

A large number of numerical studies has been devoted to the calculation of particle diffusion coefficients D_i ($i = x, y, z$), both for transport parallel and perpendicular to the average magnetic field (Giacalone and Jokipii, 1999; Casse et al., 2001). Anomalous, non Gaussian regimes which encompass a nonlinear scaling with time of the mean square deviation are also possible (Zimbardo, 2005; Zimbardo et al., 2006; Pommois et al., 2007; Shalchi and Kourakis, 2007). In the case of low frequency, long wavelength, magnetic turbulence, the possibility has also been considered of subdiffusive perpendicular transport due to particles retracing their trajectories after collisions or pitch angle diffusion (Rechester and Rosenbluth, 1978; Kota and Jokipii, 2000; Shalchi, 2010). This process, called compound diffusion, is essentially non-Markovian (Kota and Jokipii, 2000), due to the memory effect induced by tracing backwards the (magnetostatic) field lines, and corresponding to an anticorrelation of perpendicular particle motion.

Several parameters can influence the transport regime of energetic particles, like the turbulence level $\delta B/B_0$, the extension of the turbulence spectrum, the anisotropy of turbulence, and the ratio between the particle Larmor radius R_L and the turbulence correlation length l_c. In recent years, it has been shown that solar wind turbulence is very intermittent, too. Indeed, intermittency is one of the most typical properties of the turbulent energy

cascade, and it manifests itself as highly localized and intense magnetic field fluctuations with magnitude distributed according to a power law. In the present work we present a new numerical code where, beside the other parameters, the level of intermittency can also be tuned, and perform a numerical effort in order to understand what is the influence of the length of the turbulence spectrum, of the turbulence intermittency, and of $\delta B/B_0$ on the transport regimes.

4.1 Synthetic turbulence model

In our problem, the largest scale can be assumed as the correlation length in the solar wind turbulence $l_{max} = l_c \sim 5 \times 10^6$ km. To include the energetic proton Larmor radius R_L within the range of spatial scales, the condition $\xi > 1/\rho$ should be satisfied, where $\xi = l_{max}/l_{min}$ is the largest to smallest scale ratio, referred to as spectral width, and $\rho = R_L/l_{max}$ is the rigidity parameter. In particular, $R_L = m_p cv/(eB) \sim 2\times10^4$ km, corresponding to a rigidity parameter value $\rho = R_L/l_{max} \sim 4\times10^{-3}$. Thus, the above condition implies a spectral width between two and three decades ($\xi > 250$).

A representation of the turbulent magnetic field can be derived from the numerical solution of the MHD equations. This approach has the advantage of being based on first principles. However, in the most performant 3-D MHD simulations the spectral width ξ is of the order of 10^3. Then, studies of test particle diffusion based on numerical simulations with a realistic extention of the spatial scale range would require high-resolution 3-D samples, obtained with big computational efforts and large computing resources. For these reasons, it can be useful to adopt different approaches, referred to as "synthetic turbulence", which give a description of a turbulent magnetic field as realistic as possible, but with much lower computational effort than

direct simulations. A simple method to obtain a fluctuating magnetic field $\mathbf{B}$ is to superpose Fourier harmonics with a prescribed spectrum, random phases and with a polarization such as to satisfy the condition $\nabla \cdot \mathbf{B} = 0$ (Casse et al., 2001; Pommois et al., 2001, 2007). Since a regular grid in the wavevector space is employed, the number N_h of Fourier harmonics is proportional to ξ^3. For instance, in Zimbardo et al. (2006) up to $N_h = 220.000$ harmonics where used, corresponding to $\xi = 12$. This value is still too low for a realistic extention of the spectral range. Moreover, the randomness of phases does not allow to describe effects due to coherent interactions in turbulence, such as intermittency, i.e., the presence of strong localized fluctuations at small scales. In principle, intermittency could have an effect on particle diffusion.

Juneja et al. (1994) proposed a "wavelet-based" synthetic turbulence model which produces a function with the statistical properties of a signal measured along a line in a turbulent field; in particular, intermittency is reproduced. A generalization in 3D of the model by Juneja et al. (1994) has been proposed by Cametti et al. (1998); however, it suffers for strong limitations due to large memory requirements when increasing the spectral width ξ. In the present work we use a 3D model which has many aspects similar as in the model by Cametti et al. (1998), but with important differences. In particular, we employ a different algorithm which allows us to reproduce very large spectral widths (up to $\xi \sim 10^5$) with very low memory requirements and short computation times. In the following we outline the main features and properties of our synthetic turbulence model (STM); a more detailed description and discussion will be presented elsewhere (Malara & Sorriso-Valvo, paper in preparation).

The turbulence phenomenology includes an energy cascade, in which the

energy is trasferred from large to smaller scales due to nonlinear effects. In our STM we consider a 3D spatial domain in form of a parallelepiped $D = \{(x, y, z)\} = [0, L_x] \times [0, L_y] \times [0, L_z]$, where a periodic solenoidal turbulent field $\mathbf{B} = (B_x, B_y, B_z)$ is defined. To simulate the turbulent cascade, a hierarchy of cells is built at different spatial scales: at the largest scale ℓ_0 we have only one cell, which coincide with the whole domain D; thus, the corresponding typical size is $\ell_0 = (L_x L_y L_z)^{1/3}$. The cells relative to the next scale ℓ_1 are obtained by dividing the sides of D in two equal parts, thus obtaining eight equal parallelepipeds, each occupying 1/8 of the volume V_0 of D. Such a process is recursively repeated a number N_s of times, where N_s is the number of scales considered in the model; thus, at the scale $\ell_m = 2^{-m}\ell_0$ $(m = 0, \dots N_s)$ we have 2^{3m} cells, each occupying a volume $V_m = 2^{-3m}V_0$. All the cells at any given scale ℓ_m form a 3D lattice filling the whole domain D. We indicate the cells by

$$C^{(i,j,k;m)} = \{(x, y, z)\} = \left[(i-1)\frac{L_x}{2^m}, i\frac{L_x}{2^m}\right] \times \left[(j-1)\frac{L_y}{2^m}, j\frac{L_y}{2^m}\right] \times \left[(k-1)\frac{L_z}{2^m}, k\frac{L_z}{2^m}\right] \quad (4.1)$$

where $m = 0, \dots, N_s$ identifies the scale ℓ_m; hereafter the indexes $i, j, k = 1, \dots, 2^m$ will identify the cell position within the 3D lattice at the m-th scale. The smallest scale is $\ell_{N_s} = 2^{-N_s}\ell_0$. For instance, using $N_s = 16$ we have a spectral width $\xi = \ell_0/\ell_{N_s} = 2^{16} \simeq 6.5 \times 10^4$, while the total number of cells is

$$N_{cell} = \sum_{m=0}^{N_s} 2^{3m} \simeq 3 \times 10^{14} \quad (4.2)$$

The turbulent field is modelled as a superposition of spatially-localized eddies. Each eddy is associated with a cell, so the total number of eddies concides with N_{cell}. We indicate by $\delta\mathbf{B}^{(i,j,k;m)}$ the field of the eddy associ-

ated with the cell $C^{(i,j,k;m)}$. Since the field is solenoidal, we write it in the form $\delta\mathbf{B}^{(i,j,k;m)} = \nabla \times \mathbf{A}^{(i,j,k;m)}$. Both $\delta\mathbf{B}^{(i,j,k;m)}$ and the vector potential $\mathbf{A}^{(i,j,k;m)}(x,y,z)$ are defined in the subdomain

$$\begin{aligned} D^{(i,j,k;m)} = \{(x,y,z)\} \quad = \quad & \left[\left(i-\frac{3}{2}\right)\frac{L_x}{2^m}, \left(i+\frac{1}{2}\right)\frac{L_x}{2^m}\right] \times \\ & \left[\left(j-\frac{3}{2}\right)\frac{L_y}{2^m}, \left(j+\frac{1}{2}\right)\frac{L_y}{2^m}\right] \times \\ & \left[\left(k-\frac{3}{2}\right)\frac{L_z}{2^m}, \left(k+\frac{1}{2}\right)\frac{L_z}{2^m}\right] \end{aligned} \tag{4.3}$$

and are vanishing outside $D^{(i,j,k;m)}$. Comparing Equations (4.1) and (4.3) we see that the subdomain $D^{(i,j,k;m)}$ is wider than the corresponding cell $C^{(i,j,k;m)}$ by a factor 2 along each space direction. Thus, the fields of adjacent cells partially overlap. Indeed, if $D^{(i,j,k;m)}$ and $C^{(i,j,k;m)}$ were coincident, the fluctuating field at a given scale would vanish at any surface border of adjacent cells. Thus, eddy overlapping is implemented in order to obtain a statistically homogeneous fluctuating field. Within a given subdomain $D^{(i,j,k;m)}$ a set of linearly rescaled local spatial coordinates are defined by the relations:

$$\begin{aligned} X^{(i;m)} = X^{(i;m)}(x) &= \frac{2^{m-1}}{L_x}\left[x - \left(i-\frac{1}{2}\right)\frac{L_x}{2^m}\right] \\ Y^{(j;m)} = Y^{(j;m)}(y) &= \frac{2^{m-1}}{L_y}\left[y - \left(j-\frac{1}{2}\right)\frac{L_y}{2^m}\right] \\ Z^{(k;m)} = Z^{(k;m)}(z) &= \frac{2^{m-1}}{L_z}\left[z - \left(k-\frac{1}{2}\right)\frac{L_z}{2^m}\right] \end{aligned} \tag{4.4}$$

The origin $(X^{(i;m)}, Y^{(j;m)}, Z^{(k;m)}) = (0,0,0)$ of rescaled coordinates corresponds to the center of the subdomain $D^{(i,j,k;m)}$, while each rescaled coordinate varies in the interval $[-1/2, 1/2]$ when the point (x,y,z) varies inside $D^{(i,j,k;m)}$.

The explicit form of the vector potential is given in terms of the rescaled coordinates in the following form

$$\mathbf{A}^{(i,j,k;m)}(x,y,z) = a^{(i,j,k;m)} F(\xi)F(\eta)F(\zeta) \tag{4.5}$$

where $a^{(i,j,k;m)}$ is the eddy amplitude and $F(t)$ is a polynomial function which determines the spatial profile of the eddy. We used the form:

$$F(t) = 256t^8 - 256t^6 + 96t^4 - 16t^2 + 1 \ , \ \text{for} \ -\frac{1}{2} \leq t \leq \frac{1}{2}$$
$$F(t) = 0 \ , \ \text{elsewhere}$$

The function $F(t)$ has one single maximum at $t = 0$ ($F(0) = 1$) and vanishes with its derivatives up to the 4-th order at $t = \pm 1/2$. Then, it represents a localized eddy which matches with neighbouring eddies with continuous derivatives up to the 4-th order. The variables ξ, η and ζ are related to the rescaled coordinates by the nonlinear relations:

$$\begin{aligned} \xi &= X^{(i;m)} + \alpha_x^{(i,j,k;m)} \left({X^{(i;m)}}^2 - \frac{1}{4} \right) \\ \eta &= Y^{(j;m)} + \alpha_y^{(i,j,k;m)} \left({Y^{(j;m)}}^2 - \frac{1}{4} \right) \\ \zeta &= Z^{(k;m)} + \alpha_z^{(i,j,k;m)} \left({Z^{(k;m)}}^2 - \frac{1}{4} \right) \end{aligned} \tag{4.6}$$

where $\alpha_x^{(i,j,k;m)}$, $\alpha_y^{(i,j,k;m)}$, $\alpha_z^{(i,j,k;m)}$ are constants which are randomly chosen in the interval $[-1, 1]$. The nonlinear mapping (4.6) introduces a distortion in the spatial profile of the eddy along the three spatial directions, whose entity is determined by the three random numbers $\alpha_x^{(i,j,k;m)}$, $\alpha_y^{(i,j,k;m)}$ and $\alpha_z^{(i,j,k;m)}$. This effect has been introduced in order to improve the statistical homogeneity of the fluctuating field. Note that the above regularity

properties of the vector potential are preserved by the mapping (4.6).

The amplitudes $a^{(i,j,k;m)}$ of the eddies are determined considering the phenomenology of the turbulent cascade. In a stationary situation, the mean energy transfer rate $\langle\epsilon\rangle$ at a given spatial scale ℓ is independent of ℓ (Kolmogorov, 1941), angular parentheses indicating a spatial average. Assuming $\langle\epsilon\rangle \sim [\delta B(\ell)]^3/\ell$, implies that the mean fluctuation at the scale ℓ is $\delta B(\ell) \propto \ell^{1/3}$. This scaling law corresponds to the Kolmogorov spectrum, where the spectral energy density $e(k) \propto k^{-5/3}$. However, the energy transfer rate ϵ is not spatially uniform, but can change from place to place according to the effectiveness of nonlinear couplings (Kolmogorov, 1962). As a result, the amplitude of fluctuations is not spatially uniform, but fluctuations stronger than the average value $\langle\delta B(\ell)\rangle$ form, which are separated by regions where fluctuations are weaker. This feature propagates to smaller scales through a multiplicative process, becoming more and more relevant with decreasing ℓ. Thus, at the smallest scale the field is characterized by very strong and localized fluctuations with wide "quiet" regions in between: this is the phenomenology of intermittency.

In our STM such a process is modelled as in the "p-model" by Menevau & Sreenivasan (1987), where p is a fixed parameter chosen in the interval $[1/2, 1]$. Energy flows from large to smaller eddies with an unequal rate ϵ: each "parent" eddy at a scale ℓ_m gives energy to its eight "daughter" eddies at the scale ℓ_{m+1} with two possible rates; namely, $\epsilon_{m+1} = 2p\epsilon_m \geq \epsilon_m$ for four daughter eddies and $\epsilon_{m+1} = 2(1-p)\epsilon_m \leq \epsilon_m$ for the remaining four daughter eddies. For $p = 1/2$ we have $\epsilon_{m+1} = \epsilon_m$, i.e., the rate ϵ is equal at all the scales and positions; this corresponds to a non-intermittent fluctuating field. With increasing p above the value $1/2$, differences between the rates increase and the level of intermittency increases, as well. In our STM p

is a free parameter that we use to investigate the effects of intermittency. More specifically, the transfer rate is recursively determined for the daughter eddies of the "$(i,j,k;m)$" parent eddy by:

$$\epsilon_{m+1,n} = 2p\,\epsilon_m\,\beta_n^{(i,j,k;m)} + 2(1-p)\,\epsilon_m\,(1-\beta_n^{(i,j,k;m)}),$$
$$m = 0,\ldots,N_s \quad , \quad n = 1,\ldots,8 \tag{4.7}$$

where $\beta_n^{(i,j,k;m)} = 1$ for four randomly chosen daughters (for instance, $n = 3,5,7,8$) which receive more energy, while $\beta^{(i,j,k;m)} = 0$ for the remaining four daughters ($n = 1,2,4,6$) which receive less energy. Finally, the amplitude of any eddy is given by

$$a^{(i,j,k;m)} = \sigma^{(i,j,k;m)} a_0 \left[\frac{\epsilon_m^{(i,j,k;m)}}{\epsilon_0}\frac{\ell_m}{\ell_0}\right]^{\alpha} \tag{4.8}$$

where $a_0 = a^{(1,1,1;0)}$ and $\epsilon_0 = \epsilon^{(1,1,1;0)}$ are the amplitude and the energy transfer rate at the largest scale, respectively. The exponent α is related to the spectral slope: the Kolmogorov spectrum corresponds to $\alpha = 1/3$. The quantity $\sigma^{(i,j,k;m)}$ represents the sign of the eddy and it is randomly chosen as $\sigma^{(i,j,k;m)} = 1$ or $\sigma^{(i,j,k;m)} = -1$. In conclusion, the fluctuating field is given by

$$\mathbf{B} = \mathbf{B}_0 + \sum_{m=0}^{N_s}\sum_{i,j,k=1}^{2^m} \nabla \times \mathbf{A}^{(i,j,k;m)} \tag{4.9}$$

where $\mathbf{B}_0$ is a uniform component representing a mean field, while $\mathbf{A}^{(i,j,k;m)}$ and related quantities are defined in Equations (4.5)-(4.8).

The quantities $\mathbf{A}^{(i,j,k;m)}$ depend only upon a set of randomly determined parameters; namely: (i) $\alpha_n^{(i,j,k;m)}$, which define the distortion of each eddy (Equation (4.6)) ; (ii) the sign $\sigma^{(i,j,k;m)}$ of each eddy (Equation (4.8)); (iii) $\beta_l^{(i,j,k;m)}$ which define the energy transfer rate of each eddy in terms of the

rate of its parent eddy (Equation (4.7)). Such parameters are determined in the following way: for any given cell an integer $l^{(i,j,k;m)}$ is calculated using the expression:

$$l^{(i,j,k;m)} = i + (j-1)2^m + (k-1)2^{2m} + f(m) \tag{4.10}$$

where $f(m)$ is defined as follows:

$$f(m) = \begin{cases} 0 & \text{if} \quad m = 0; \\ \sum_{n=0}^{m-1} 2^{3m} & \text{if} \quad m \geq 1. \end{cases} \tag{4.11}$$

It can be verified that the expression (4.10) generates all the integers between 1 and N_{cell}, thus defining a one-to-one corrispondence between the set $\{1 \leq l \leq N_{cell},\ l \text{ integer}\}$ and the set of cells. In other words, $l^{(i,j,k;m)}$ represent the absolute address of any cell. The integer $l^{(i,j,k;m)}$ is used as a seed for a random-number generating routine, which produces the above parameters (i), (ii) and (iii). We note that the total number N_{cell} of values of $l^{(i,j,k;m)}$ is, in practice, extremely high (Equation (4.2)). This ensures a global randomness of the parameters defining the structure of single eddies.

The evaluation of the field $\mathbf{B}$ at a given point $P = (x.y, z)$ would in principle to be done through the expression (4.9), where the sum on the RHS includes a number of terms as high an N_{cell}. However, since each eddy occupy a finite volume, only a small number N_{term} of terms must be considered in this sum: in particular, these are the terms corresponding to eddies whose subdomain $D^{(i,j,k;m)}$ contains the point P. Due to the eddy overlapping, the number of terms to be calculated varies in the interval $N_s \leq N_{term} \leq 8N_s$. For instance, using a number $N_s = 16$ of scales, corresponding to a spectral width $\xi \simeq 6.5 \times 10^4$, the number of terms to

be considered is not larger than 128. This makes the evaluation of the field very fast. Moreover, both N_{term} and the computation time are proportional to the number of scales N_s; for instance, increasing N_s by a factor 2 would increase the spectral range by a factor 2^{N_s} while the computation time would simply be increased by a factor 2. Another important property of our STM is that it does not require large memory storage. Indeed, in the above-described algorithm nothing needs to be kept in memory: each time the field needs to be calculated at a point P, this is done deducing all the properties of the N_{term} involved eddies directly from their absolute address $l^{(i,j,k;m)}$. Moreover, the field $\mathbf{B}$ has the same regularity properties as that of single eddies: namely, it is continuous with all space derivatives up to the 3-rd order. Finally, at variance with other methods, no spatial grids are involved; on the contrary the field is directly calculated at any spatial point without any interpolation process.

4.2 Numerical simulations and results

We perform test particle simulations integrating the Lorentz Equations for the trajectories and velocities of $N_p = 1000$ protons of fixed energy ~ 1 MeV using the Boris method as time stepper (Qin et al. (2013), Webb (2014)). In every simulation the particles are placed with equal speed $v = 2 \times 10^4$ km/s and random directions and positions inside a cubic box of length $L = 4l_c$, where $l_c = 5 \times 10^6$ km is the solar wind turbulence correlation length. The magnetic field is computed at each step through the STM described in the previous section and it has this analytical form:

$$\mathbf{B}(x, y, z) = B_0 \hat{\mathbf{z}} + \delta\mathbf{B}(x, y, z)$$

where $B_0 = 10^{-4}G$ is a constant value and $\delta\mathbf{B}(x, y, z)$ is given by Equation (4.9) and represents a 3-D isotropic turbulent field with zero mean. In this configuration we can define the diffusion coefficients parallel and perpendicular to the mean magnetic field as:

$$D_{\parallel}(t) = \frac{1}{2N_p t} \sum_{i=1}^{N_p} \left(z_i(t) - z_i(0)\right)^2 \tag{4.12}$$

$$D_{\perp}(t) = \frac{1}{2N_p t} \sum_{i=1}^{N_p} \left(x_i(t) - x_i(0)\right)^2 + \left(y_i(t) - y_i(0)\right)^2 \tag{4.13}$$

where $r_i(t) = (x_i(t), y_i(t), z_i(t))$ is the position of the i-th particle in function of time. Through the simulations we would like to investigate how transport is affected by three different features of the STM: the spectral width, the amplitude of the turbulence and the level of intermittency. Each of these is controlled by a single parameter: $\xi = l_c/l_{min}$ controls the spectral width; $\eta = \delta B/B_0$, where δB is the root mean square of the turbulent fluctuation sampled and averaged over the domain, controls the amplitude of the turbulence; p the p-model parameter controls the level of intermittency.

4.2.1 Varying the spectral width

In the simultations discussed in this section we consider a large amplitude turbulence configuration ($\eta = 1$), typical of astrophysical plasmas, first without intermittency ($p = 0.5$). We have defined $\xi = l_c/l_{min}$ as the spectral width and we can vary this parameter varying the smallest scale of the STM. It is interesting to consider the value of ξ in relation to the inverse of the "rigidity" $\rho = R_L/l_{max}$. To include the energetic proton Larmor radius R_L within the range of spatial scales of the STM spectrum, the condition $\xi > 1/\rho$ must be satisfied. In particular in our simulation

$R_L = m_p cv/(eB_0) \sim 2 \times 10^4$ km, corresponding to a rigidity parameter value $\rho = R_L/l_{max} \sim 4 \times 10^{-3}$. Thus, the above condition implies that for $\xi > 250$ the Larmor scale is inside the STM inertial range, and it is outside that range for $\xi < 250$. In Figure 4.1 the diffusion coefficients in the

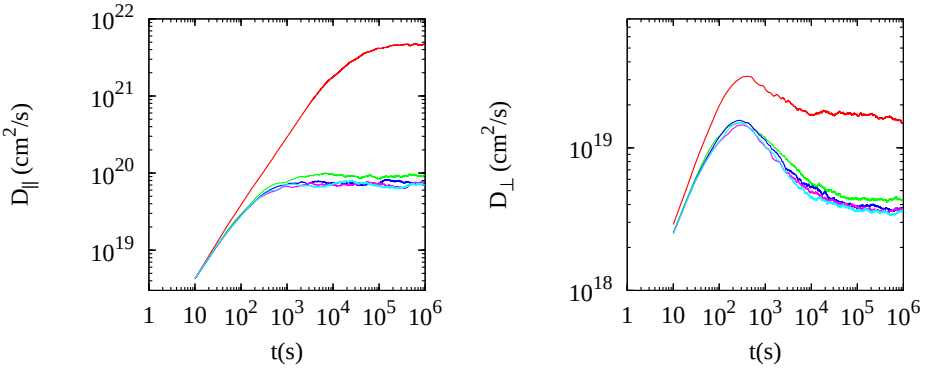

Figure 4.1: Parallel and perpendicular diffusion coefficients in function of time for different spectral width: $\xi = 4$ (red), $\xi = 128$ (green), $\xi = 256$ (blue), $\xi = 1024$ (purple) and $\xi = 16384$ (light blue).

direction parallel and perpendicular to the mean magnetic field in function of time are plotted for different values of ξ. We can notice how the value of ξ actually affects transport. When the Larmor scale is way smaller than the smallest scale of the spectrum ($\xi = 4$) the diffusion is enhanced both in parallel and in perpendicular direction. In this case (red curve) a regime of normal diffusion is reached for parallel transport at a time $t \sim 10^5$s, while subdiffusion is observed in the perpendicular direction for long times. If the minimum scale approches the Larmor scale both diffusion coefficients become smaller. We observe also that normal diffusion regime in the parallel direction is reached earlier, at a time $t \sim 10^3$s, and that in the perpendicular direction normal diffusion is recovered for long times, while a subdiffusive regime can be identified for $10^3 s < t < 10^5$s (see the discussion below). Moreover, when the spectrum extends far beyond the Larmor scale the dif-

fusion coefficients do not change anymore, meaning that all the fluctuations at a scale smaller than the Larmor radius are averaged over a gyration (purple and light blue curves), see also (Pommois et al., 2007). In Figure 4.2

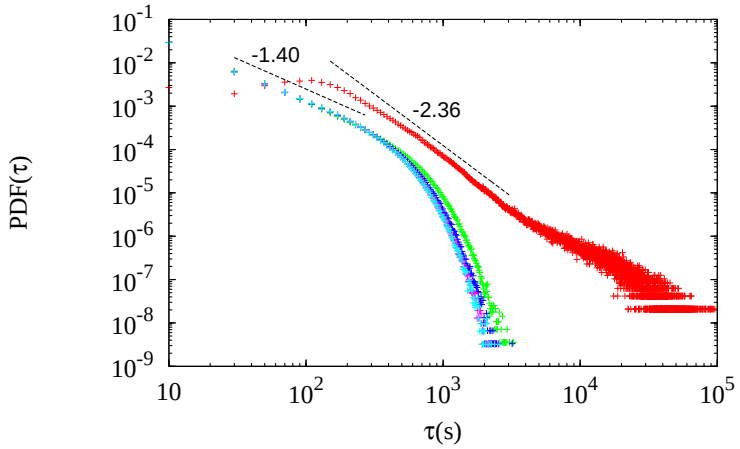

Figure 4.2: PDF of the inversion time τ for different spectral width: $\xi = 4$ (red), $\xi = 128$ (green), $\xi = 256$ (blue), $\xi = 1024$ (purple) and $\xi = 16384$ (light blue) and power laws linear fits (black).

the PDFs of the inversion time τ, i.e. the elapsed time between two sign inversion of the pitch angle cosine, are plotted for different ξ. We notice that for $\xi = 4$ the inversion times extend up to $\tau \sim 10^5$ that is also the time that needs to reach normal diffusion in the parallel direction. The PDF in this case has a maximun at $\tau \sim 10^2$ and then dicreases with an average slope $\simeq -2.36$. All the other cases at higher ξ present similar PDFs of τ. for these cases it is possible to identify a power law with slope $\simeq -1.4$ that has a break at times $10^2 < \tau < 10^3$. We notice that the time of the break corresponds to the time when the normal diffusion regime sets up in parallel transport and it moves to smaller τ as ξ increases. In Figure 4.3 two samples of the trajectory of a single particle in the case $\xi = 4$ and $\xi = 1024$ are shown. The plots are meant to show how trajectories and picth angle scattering change qualitatively when the condition $\xi > 1/\rho$ is satisfied.

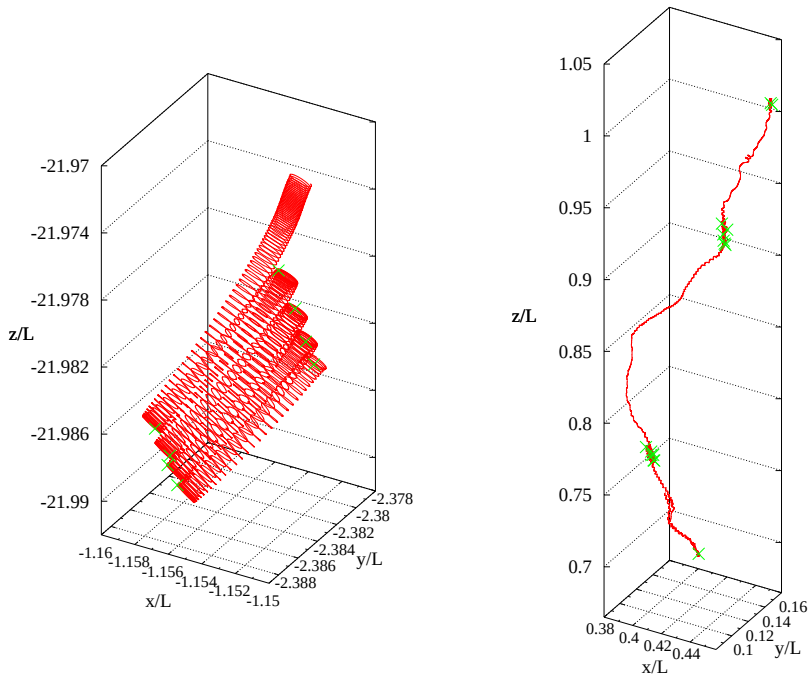

Figure 4.3: Sample of trajectory (red line) and pitch angle scattering sites (green crosses) for $\xi = 4$ (left panel) and $\xi = 1024$ (right panel). In the right panel the gyration motion is not visible because is small compared to the guiding center motion.

We selected two samples where multiple events of picth angle scattering are present. We can see how in the $\xi = 4$ case (left panel) the particle scatter due to magnetic mirroring. Instead in the case of $\xi = 1024$ (right panel) the pitch angle scattering events are concetrated in particular sites, possibly associated with magnetic mirroring, too. When a particle encounter one of this sites goes through multiple pitch angle scattering; it eventually exits the site and "fly" until it is not trapped again by another site.

4.2.2 Varying the amplitude of the turbulence

In the simulation described in this section we keep the Larmor scale inside the spectrum setting $\xi = 1024$ and consider a non intermittent turbulence

($p = 0.5$). The amplitude of the turbulence is controlled by the parameter η, that is the ratio between the root mean square of the turbulent fluctuations and the background magnetic field amplitude. In Figure 4.4 parallel and

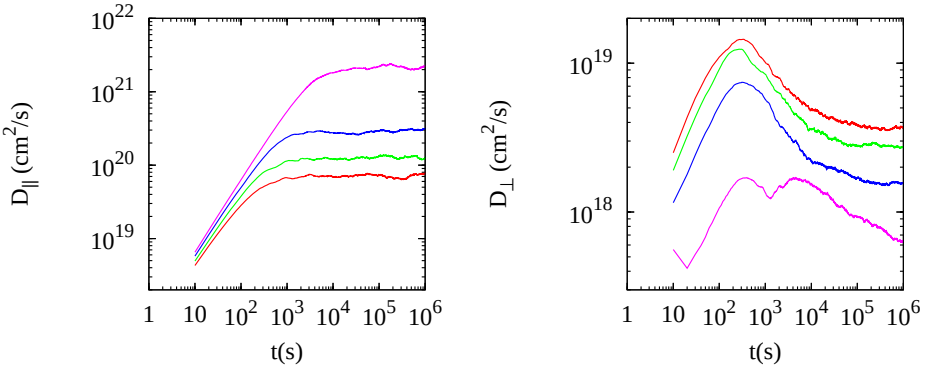

Figure 4.4: Parallel and perpendicular diffusion coefficients in function for different level of the turbulence: $\eta = 1.0$ (red), $\eta = 0.75$ (green), $\eta = 0.5$ (blue), $\eta = 0.2$ (purple).

perpendicular diffusion coefficients as a function of time are shown for different η. In every case a diffusive regime is eventually reached in the parallel direction. We have to notice that this happens the later when the level of the turbulence is the lower. The asymptotic value of the coefficient descreases when η increase meaning that strong turbulence reduces parallel transport. In the perpendicular direction the situation is more complex. In the $\eta = 1.0$ case there is an indication of recovery of diffusion at long times, instead for $\eta = 0.2$ the behaviour is clearly subdiffusive at long times. An intermediate behaviour is obtained in the intermediate cases $\eta = 0.75$ and $\eta = 0.5$, where there is an increase of the subdiffusive behaviour with the decrease of η. These results can be understood in terms of compound diffusion, a basically subdiffusive regime (Zimbardo, 2005; Webb et al., 2006; Pommois et al., 2007; Tautz and Shalchi, 2010; Bitane et al., 2010; Giacalone, 2013), which is due to particles tracing back their field lines after pitch angle dif-

fusion. In such a case, the perpendicular spreading of particles is reduced, since particles perform an effectively anti-persistent random walk (Perrone et al., 2013; Zimbardo et al., 2015), which leads to subdiffusion. On the other hand, when the level of turbulence increases, the stochastic separation of magnetic field lines increases, too, to the point that pitch angle scattered particles do not trace back the "original" field line, but another field line which is diverging exponentially. This exponential divergence is quantified by the Kolmogorov entropy and by the Kubo number (Rechester and Rosenbluth, 1978; Zimbardo et al., 2009; Bitane et al., 2010), and indeed it can be shown that it depends on the level of turbulence and on the turbulence anisotropy. Therefore, for large turbulence levels and for magnetic fluctuations with enough perpendicular structure, normal diffusion is recovered (e.g., Qin et al., 2002a,b). In Figure 4.5 the PDF of τ are plotted. We can

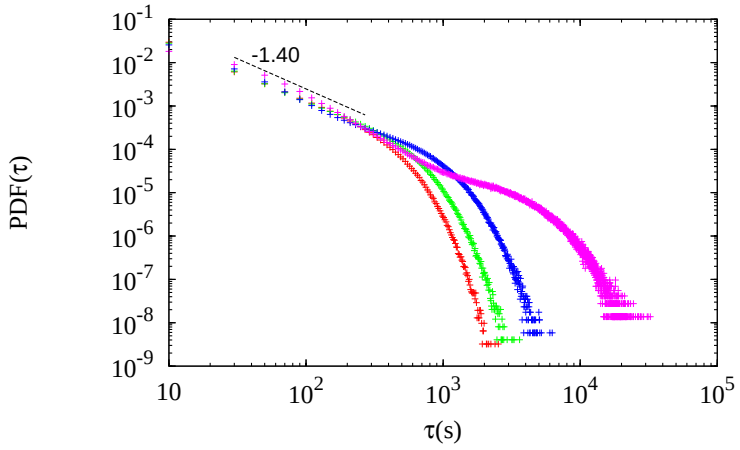

Figure 4.5: PDF of the inversion time τ for different level of the turbulence: $\eta = 1.0$ (red), $\eta = 0.75$ (green), $\eta = 0.5$ (blue), $\eta = 0.2$ (purple) and corresponding power laws linear fits (same colors).

see that as η decreases the PDFs extend to larger values of τ. A power law of the type $\propto \tau^{-1.4}$ fits the PDF for small value of τ for $\eta = 1.0$, instead for smaller value of η it is more difficult to find a power law dependence that

fits the data for at least one decade of the plot.

4.2.3 Varying the level of the intermittency

The last part of the numerical investigations is related to the influence of intermittency on transport. For all this set of simulations we fix $\xi = 16,384$ in order to keep the Larmor scale inside the STM inertial range and we consider a large amplitude turbulence ($\eta = 1$). In the section dedicated to the STM we have explained how intermittency is reproduced through a p-model. We recall that in our model $p = 0.5$ means no intermittency and $p = 1.0$ means extremely strong intermittency. In Figure 4.6 the evolution of diffusion coefficients as a function of time is plotted for different value of p. In the parallel direction, a normal diffusion regime is reached at a time $t = 10^3 s$ for all p but, interestingly, the asymptotic value of the diffusion coefficients increases with an increasing level of intermittency. In the perpendicular direction, changing the value of p does not make such a great difference, the transport appears to be subdiffusive up to 10^5 s and becomes eventually diffusive, with all the curves converging to the same asymptotic value. A possible explanation for why intermittency has the effect of enhancing parallel diffusion can be found in Figure 4.7 where the PDFs of τ are plotted. We can see that the shape of the PDFs does not change qualitatively when p varies. They all present a power law dependence of the type $\propto \tau^{-1.4}$ at small τ and an exponential decay at larger τ. What does change is the position of the break of the power law that moves to larger τ as p increases. This means that in presence of intermittency a particle has a greater probability to travel for longer times without inverting its motion than the case where intermittency is absent. We believe that is related to the fact that intermittency appears as strong burst in the magnetic field

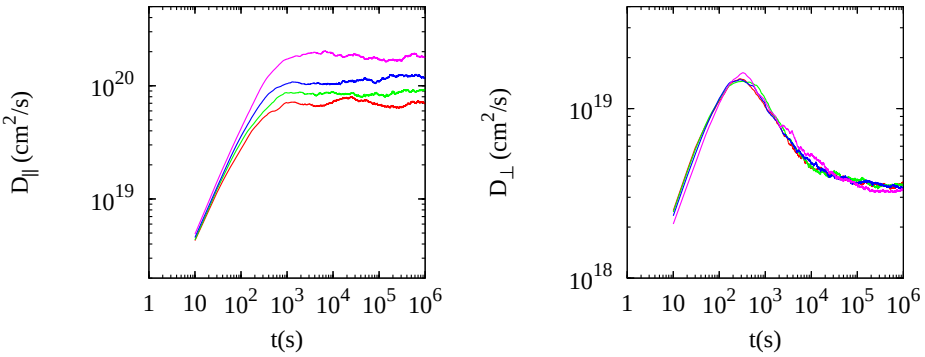

Figure 4.6: Parallel and perpendicular diffusion coefficients in function of time for different level of the intermittency: $p = 0.5$ (red), $p = 0.7$ (green), $p = 0.8$ (blue), $p = 0.9$ (purple).

fluctuations at small scales. A stronger intermittency means that this bursts are stronger and more localized in space and this allows a particle to travel longer without changing the direction of its motion, as it is shown in Figure 4.7.

4.3 Discussion

The numerical simulations performed showed very interesting and new results. In the perpendicular direction, in every case considered, the transport is normal. There is no evidence of superdiffusive transport along the magnetic field. In the perpendicular direction we found normal diffusion or subdiffusion, depending on the stochasticity of the field lines. When the intensity of the turbulent fluctuations is comparable to the intensity of the background magnetic field the diffusion in the perpendicular direction is normal. A subdiffusive regime in the perpendicular transport, instead, is found when the level of turbulence is low or when the fluctuation energy at the Larmor scale is small. We showed that the latter, that is related to the

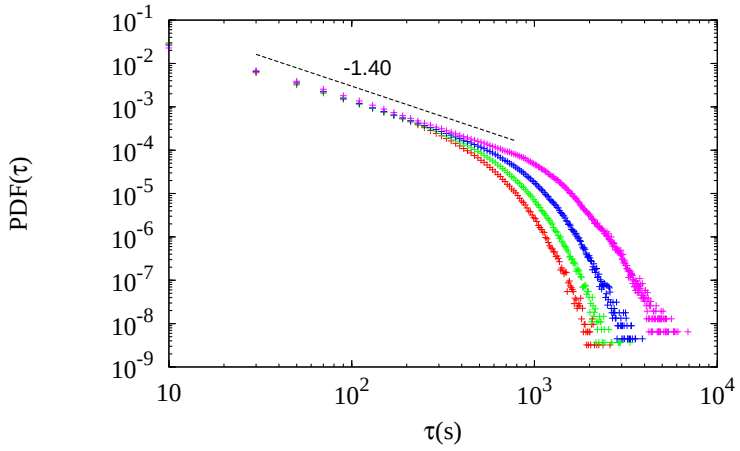

Figure 4.7: PDF of the inversion time τ for different level of the intermittency: $p = 0.5$ (red), $p = 0.7$ (green), $p = 0.8$ (blue), $p = 0.9$ (purple) and power law linear fit (black).

length of the intertial range, plays an important role in transport. When a spectrum that extend up to the Larmor scale is considered both parallel and perpendicular diffusion coefficients become smaller than the case were the Larmor scale $k_L = 1/R_L$ is beyond the smallest scale of the turbulence inertial range. The STM used for these simulation was crucial to achive this results, because of its capability in reproducing broad band turbulence with small computational costs. Another important feature of the STM model considered was the possibility to reproduce intermittency through a p model. We showed here the first result of the effect that intermittency can have in particle transport. The results of our simulation showed how an increasing level of intermittency enhances parallel transport. Our explanation for this phenomenon is that the presence of intermittency can be seen as the presence of concetrated bursts of magnetic field intensity. More intermittency means that these coherent structures are more strong and concentrated in space. This gives to a particle the possibility to diffuse more between two interaction with these kind of structure of this type, during which the particle

goes through pitch angle scattering. We didn't find any effect of intermittency in the perpendicular transport. In a future work it will be interesting to compare the power law PDF reported in Figure 4.7 with the power law distributions of scattering times found in the solar wind by Perri and Zimbardo (2012b). In that case, magnetic field measurements by the Ulysses spacecraft at 5 AU were used, and the scattering time was obtained from the inverse of the magnetic variance, using the quasi-linear theory expression for the pitch angle diffusion coefficient. A comparison of this type could give more information about how appropriate the use of linear theory is to study this kind of phenomena. Another possible future work is the study of the role of intermittency in influencing the perpendicular transport when low level turbulence is considered. Finally the case of anisotropic turbulence as to be taken into account. It has been shown, in fact, that in astrophysical plasmas, for example in solar wind, the turbulence spectrum is highly anisotropic, the turbulent cascade favoring the formation of smallest scale in the direction perpendicular to the local magnetic field.

Chapter 5

Conclusion

We would like to summarize briefly the results achieved in this work and discuss possible future works.

The numerical simulations of the dynamics of low layers of solar corona have revealed that the phenomenology of this region is highly influenced by the kind of waves that propagates through it. We showed that when an Alfvén wave is injected, an anisotropic power-law spectrum forms with a dominance of perpendicular wavevectors at altitudes $\sim 10^4$ km. Density fluctuations are generated near the X-point by Alfvén wave magnetic pressure, and propagate along open field lines at a speed comparable with the local Alfvén velocity. In the magnetosonic case, small scales form only around the X-point, where a phenomenon of oscillating magnetic reconnection is observed to be induced by the periodic deformation of the magnetic structure due to incoming waves. There are several future steps that could be taken in the study of this problem. The first one is to consider a more realistic 3D configuration. Moreover, considering a system that extends to higher altitude, where longitudinal gradient like density stratification cannot be neglected, can be another possible improvement. A study of this

kind could be used to predict what feature will be observed by the future mission Solar Probe Plus when it will go beyond the Alfvénic point. Finally, the method of projected characteristic developed is a valuable tool that can be used to simulate open structures in the heliosphere overcoming the limitation of periodical boundary conditions.

In the second chapter we showed that when an Alfvén wave propagate in a 2D pressure-balanced structure where the magnetic field intensity has a perpendicular gradient, kinetic Alfvén waves are produced. Kinetic Alfvén waves have been shown to be responsible for the distortion of the distribution function and consequent generation of kinetic temperature anisotropy. In particular kinetic Alfvén waves resonate with particles producing beams in the proton velocity distribution function directed in the direction parallel to the background magnetic field. In the work here presented we showed that in certain configurations the phenomenon of phase-mixing can be responsible for kinetic Alfvén waves generation. A future work will be to study the dynamics of propagation of an Alfvén wave in a configuration where the background quantities (density, temperature and magnetic field) are homogenous, and a parallel velocity field with a perpendicular shear is present. This set up is intented to represent, for instance, microstreams in the solar wind. In this case, phase-mixing would also be at play and this could lead to kinetic Alfvén wave generation, this time in a medium where the Alfvén velocity and the plasma β are homogeneous.

Preliminary results in the work of particle acceleration in 3D Reduced MHD decaying turbulence have shown that in such configuration particles are preferentially accelerated in the parallel direction. As discussed at the end of the chapter this results are very different to what previously found in a similar configuration where a 3D compressible MHD model with a strong

background magnetic field has been considered. The cause of this differences have to be investigated more deeply in future works. Moreover, understanding how particles energization scales with the Reynolds number of the turbulent system considered will be important to compare our results with physical heliospheric environments, like solar corona, where Reynolds number values are too high to be reproduced in numerical experiments.

In the fourth chapter the problem of particle diffusion in turbulence was studied through test particle simulation in a magnetic field produced by a synthetic turbulence model. This model gave us the possibility to consider a magnetic field with a broad band inertial range with a small computational cost and to reproduce intermittency. Our numerical experiments showed the first evidence that intermittency can influence particle transport in turbulent medium. In particular we found that the role of intermittency, in presence of strong turbulence, is to enhance parallel diffusion. No effect due to intermittency have been observed in the perpendicular transport. The turbulence considered in this work was isotropic and embedded in a strong background magnetic field. The future work on this problem will be considering an anisotropic spectrum where at small scales perpendicular wavevectors dominate on parallel ones, since it has been shown that such an asymmetry can be a results of turbulence evolution in the presence of a strong background magnetic field.

Appendix A

Numerical calculation of the vector potential

The magnetic field of our model can be expressed in terms of a vector potential $\mathbf{A}(x,z) = A(x,z)\mathbf{e}_y$:

$$\mathbf{b}(x,z) = \nabla \times (A(x,z)\mathbf{e}_y) \tag{A.1}$$

where the following equations hold for the magnetic field components:

$$b_x(x,z) = -\frac{\partial A(x,z)}{\partial z} \tag{A.2}$$

$$b_z(x,z) = \frac{\partial A(x,z)}{\partial x} \tag{A.3}$$

We derive an analytical expression for $A(x,z)$ as a function of the magnetic field components using the periodicity of b_x and b_z along the z-direction.

The magnetic field components can be written as:

$$b_x(x,z) = \sum_{k_z} \hat{b}_x(x,k_z)e^{ik_z z} \tag{A.4}$$

$$b_z(x,z) = \sum_{k_z} \hat{b}_z(x,k_z)e^{ik_z z}. \tag{A.5}$$

Equations (A.2)-(A.5) establish that the partial derivatives of $A(x,z)$ have to be periodical functions of the variable z. The most general form of $A(x,z)$ that fulfills this condition is:

$$A(x,z) = \sum_{k_z} \hat{A}(x,k_z)e^{ik_z z} + cz + A_0 \tag{A.6}$$

where c and A_0 are both constants. The value of c and of the coefficients $\hat{A}(x,k_z)$ define A univocally. We can calculate them by substituting expression (A.6) and the Equations (A.4) and (A.5) in the Equations (A.2) and (A.3):

$$\sum_{k_z} \hat{b}_x(x,k_z)e^{ik_z z} = -\sum_{k_z} ik_z \hat{A}(x,k_z)e^{ik_z z} - c \tag{A.7}$$

$$\sum_{k_z} \hat{b}_z(x,k_z)e^{ik_z z} = \sum_{k_z} \frac{\partial \hat{A}(x,k_z)}{\partial x} e^{ik_z z}. \tag{A.8}$$

From the Equation (A.7) we get:

$$\hat{A}(x,k_z) = \frac{\hat{b}_x(x,k_z)}{-ik_z} \qquad \forall k_z \neq 0 \tag{A.9}$$

$$c = -\hat{b}_x(x,0) \tag{A.10}$$

and from the Equation (A.8) we obtain the expression for $\hat{A}(x,0)$:

$$\hat{A}(x,0) = \int_0^x \hat{b}_z(x',0)dx'. \tag{A.11}$$

Using the Equations (A.9),(A.10) and (A.11) we have the analytical solution for $A(x,z)$:

$$A(x,z) = \int_0^x \hat{b}_z(x',0)dx' + \sum_{k_z \neq 0} \frac{\hat{b}_x(x,k_z)}{-ik_z} e^{ik_z z} - \hat{b}_x(x,0)z + A_0 \qquad \text{(A.12)}$$

where the constant A_0 is completely arbitrary. The vector potential $A(x,z)$ at any given time τ is numerically calculated using Equation (A.12) where the Fourier coefficients $\hat{b}_x(x,0)$ and $\hat{b}_z(x,k_z)$ are obtained by an FFT algorithm and the integral is computed with the Simpson's rule.

Appendix B

Numerical tests on different time steppers for test particle simulations

This appendix is devoted to show the test done on several time stepper in order to find the best one to deal with the problem of particle diffusion in the synthetic turbulence model presented in Chapter 4.

The equations that describe the motion of a particle of mass m and charge q in a magnetic field $\mathbf{b}$ are:

$$\frac{d\mathbf{v}}{dt} = \frac{q}{m}\left(\frac{\mathbf{v}}{c} \times \mathbf{b}\right), \tag{B.1}$$

$$\frac{d\mathbf{r}}{dt} = \mathbf{v}, \tag{B.2}$$

where c is the speed of light. Multiplying scalarly equation B.1 times $\mathbf{v}$ we get that the kinetic energy of the particle is conserved, which also means that the magnetic field does not make work on the particle. It just changes its direction not modifing its speed. In order to study these equations nu-

merically it is worth to write them in a non dimensional form. We can put $\mathbf{v} = V_0\tilde{\mathbf{v}}$, $\mathbf{b} = B_0\tilde{\mathbf{b}}$, $\mathbf{r} = L_0\tilde{\mathbf{r}}$, and $t = L_0/V_0\tilde{t}$, where the $\tilde{}$ variables are non dimensional and are multiplied by characteristic quantities. Substituting in B.1 and B.2 and dropping the tilde for non dimensional quantities yields to:

$$\frac{d\mathbf{v}}{dt} = \beta\left(\mathbf{v} \times \mathbf{b}\right), \tag{B.3}$$

$$\frac{d\mathbf{r}}{dt} = \mathbf{v}. \tag{B.4}$$

These two equations are non dimensional. The parameter β can be espressed in the following ways:

$$\beta = \frac{qB_0}{mc}\frac{L_0}{V_0} = \omega_L\tau = L_0/r_L$$

where $\tau = L_0/V_0$ is a characteristic time, and $\omega_L = qB/mc$ and $r_L = mcV_0/qB$ are the Larmor frequency and radius, respectively. This parameter represent how big is the gyromotion in space and time scales in respect of the tipical time and spatial scales of the problem we are considering. A big β means that the gyroperiod is small compared to the evolution time scale of the particles motion or, alternatively, that the Lamor radius is small compared to the typical spacial scale of the problem we are considering. Viceversa a small beta means that the evolution of the system is significant in a gyroperiod time scale or that the typical spacial scale of variation of the magnetic field are less than a Larmor radius. Chosing $\beta = 1$ means studying the evolution of the particle at the Larmor scale. In order to test the usefulness of a numerical method to integrate equations B.3 and B.4 we think that the best choice is to put $\beta = 1$, because in this way we can test whether the method is good to "capture" both the gyromotion and the guiding center motion. The value of β, is the same used in the problem

of particle diffusion presented in Chapter 4. We have tested four different integrators:

I) Adams-Bashfort fourth order (AB)

II) Boris method

III) Runge Kutta fourth order (RK4)

IV) Runge Kutta fifth order with an adaptive time-step (ARK5)

whose main features are briefly reported below.

Adams-Bashforth

It is a fourth order backward method that advances the equations of motion in this way:

$$\mathbf{r}_{i+i} = \mathbf{r}_i + \frac{\Delta t}{24}\left(55\mathbf{v}_i - 59\mathbf{v}_{i-1} + 37\mathbf{v}_{i-2} - 9\mathbf{v}_{i-3}\right) \tag{B.5}$$

$$\mathbf{v}_{i+i} = \mathbf{F}_i + \frac{\Delta t}{24}\left(55\mathbf{F}_i - 59\mathbf{F}_{i-1} + 37\mathbf{F}_{i-2} - 9\mathbf{F}_{i-3}\right) \tag{B.6}$$

where Δt is the step-size, $\mathbf{r}_i \equiv \mathbf{r}(t_i)$, $\mathbf{v}_i \equiv \mathbf{v}(t_i)$, $t_i \equiv i\Delta t$, and $\mathbf{F}_i \equiv \mathbf{F}(t_i)$ is the right hand side of Equation (B.4). The method has to be initialiazed for the first three steps.

Boris method

This second order symplectic Webb (2014) method was developed by Boris in 1970. Given position and velocity at the i-th step, Boris algorithm computes the $i+1$-th quantities solving these equations:

$$\frac{\mathbf{r}_{i+1} - \mathbf{r}_i}{\Delta t} = \mathbf{v}_{i+1} \tag{B.7}$$

$$\frac{\mathbf{v}_{i+1} - \mathbf{v}_i}{\Delta t} = \frac{q}{m}\left[\mathbf{E}_i + \frac{(\mathbf{v}_{i+1} + \mathbf{v}_i) \times \mathbf{B}_i}{2c}\right] \tag{B.8}$$

where Δt is the step-size, $\mathbf{r}_i \equiv \mathbf{r}(t_i)$, $\mathbf{v}_i \equiv \mathbf{v}(t_i - \Delta t/2)$, $t_i \equiv i\Delta t$, $\mathbf{E}_i \equiv \mathbf{E}(\mathbf{r}_i, t_i)$, $\mathbf{B}_i \equiv \mathbf{B}(\mathbf{r}_i, t_i)$. The scheme can be made explicit solving analytically $\mathbf{v}_{i+1}$ in terms of $\mathbf{v}_i$. In the case we are considering $\mathbf{E}_i = 0$.

RK4

The fourth order Runge Kutta method is a classical integrator for ordinary differential equations. It requires four evaluations of the time derivative: once at the initial and final points and twice at trial midpoints:

$$\begin{aligned}
\mathbf{F}_1 &= \mathbf{F}\left(\mathbf{y}_i, t\right) && \text{Initial point} \\
\mathbf{F}_2 &= \mathbf{F}\left(\mathbf{y}_i + \frac{\Delta t}{2}\mathbf{F}_1, t + \frac{\Delta t}{2}\right) && \text{First trial midpoint} \\
\mathbf{F}_3 &= \mathbf{F}\left(\mathbf{y}_i + \frac{\Delta t}{2}\mathbf{F}_2, t + \frac{\Delta t}{2}\right) && \text{Second trial midpoint} \\
\mathbf{F}_4 &= \mathbf{F}\left(\mathbf{y}_i + \Delta t\mathbf{F}_3, t + \frac{\Delta t}{2}\right) && \text{Final point}
\end{aligned}$$

where we put position and velocity at the i-th step in a six dimensional vector $\mathbf{y}_i$ and now $\mathbf{F}$ is also six-dimensional containing the right hand sides of Equation (B.3)-(B.4). Time is advanced using a weighted averaged derivative:

$$\mathbf{y}_{i+1} = \mathbf{y}_i + \Delta t\left(\frac{\mathbf{F}_1}{6} + \frac{\mathbf{F}_2}{3} + \frac{\mathbf{F}_3}{3} + \frac{\mathbf{F}_4}{6}\right) \tag{B.9}$$

RK5 with an adaptive timestep

This method uses a fifth order Runge-Kutta with a RK4 method embedded to advance in time. The difference between the advanced quantities at each step for the two methods can be used to adjust the time step in order to mantain a certain accuracy. If Δ is this difference we can write it as:

$$\Delta = \phi(\Delta t)^5$$

where ϕ is a real number. Now we can compare Δ with a scaling quantity $\mathbf{y}_{scal}$, the ratio of the two quantities being the accuracy ϵ:

$$\Delta = \epsilon \mathbf{y}_{scal}.$$

We decided to define:

$$\mathbf{y}_{scal} = \left| \Delta t \frac{d\mathbf{y}}{dt} \right| \tag{B.10}$$

and so

$$\epsilon = \frac{\Delta}{\mathbf{y}_{scal}} = \frac{\phi \Delta t^4}{\left| \frac{d\mathbf{y}}{dt} \right|}.$$

To have a good accuracy ϕ must be ~ 1 and the maximun possible value for $\mathbf{y}_{scal}$ must be put in Equation (B.10). Considering that:

$$\left| \frac{d\mathbf{y}}{dt} \right| = \begin{cases} \left| \frac{d\mathbf{r}}{dt} \right| = |\mathbf{v}| \leq 10^{-3} \\ \left| \frac{d\mathbf{v}}{dt} \right| = \beta |\mathbf{v}||\mathbf{B}| \leq 10^{-3} \end{cases}$$

we extimate $max(\mathbf{y}_{scal}) = 10^{-3}$. In the case we are studying $\Delta t = 10^{-2}$ and so we decide to set $\epsilon = 10^{-5}$. If we call ϵ_{num} the numerical value of ϵ at a

certain time step this condition must be fulfilled:

$$\epsilon_{num} \geq \epsilon.$$

If this doesn't not happen the time step is reduced until the condition is fulfilled, or until a minimum value for Δt_{min} is reached. Instead, if it does happen Δt is increased, but never exciding the initial value. We fixed $\Delta t_{min} = 10^{-4}$.

We performed three different preliminar tests, with different background magnetic field and initial conditions, but same number of time steps $N_t = 10^8$. The time-step value is $\Delta t = 10^{-2}$ (that can change in time only for the ARK5). This value has been chosen to solve the gyromotion properly. The magnitude of all this quatities has been chosen to simulate the features of the particle diffusion problem we would like to study.

Test 1 (Synchroton)

$$v_{0x} = 10^{-3}, \qquad v_{0y} = 0, \qquad v_{0z} = 0;$$

$$b_x = 0, \qquad b_y = 0, \qquad b_z = 1;$$

$$x_0 = 0, \qquad y_0 = 0, \qquad z_0 = 0;$$

This are the initial condition for a particle that moves circulary around an homogeneous magnetic field. The motion is in the plane xy.

Test 2 (Spiral motion)

$$v_{0x} = 10^{-3}, \qquad v_{0y} = 0, \qquad v_{0z} = 10^{-3};$$

$$b_x = 0, \qquad b_y = 0, \qquad b_z = 1;$$

$$x_0 = 0, \qquad y_0 = 0, \qquad z_0 = 0;$$

This test is the same of Test 1, but with a not null component of the initial velocity parallel to the background magnetic field. This changement will result in a spiral motion of the particle along z.

Test 3 (Chaotic motion)

$$v_{0x} = 10^{-3}, \qquad v_{0y} = 10^{-3}, \qquad v_{0z} = 10^{-3};$$

$$b_x = a\sin z + c\cos y, \qquad b_y = b\sin x + a\cos z, \qquad b_z = c\sin y + b\cos x;$$

$$\text{with } a = 1/\sqrt{3}, b = 1, c = \sqrt{2/3};$$

$$x_0 = 0, \qquad y_0 = 0, \qquad z_0 = 0;$$

In this test we consider a ABC background magnetic field that is well known to cause a chaotic dynamic of a charged particle that moves through it.

For the first two tests it is possible to compare the numerical solution to the analitical one, this means that not only the conservation of energy, but also the error on numerical trajectory can be monitored. This is the analitical solution for Equations B.3 and B.4, in Test 1 and 2 where $\mathbf{B}_0 = (0, 0, 1)$:

$$x(t) = \frac{v_{0x}}{\beta}\sin(\beta t) - \frac{v_{0y}}{\beta}\cos(\beta t) + \frac{v_{0y}}{\beta} + x_0$$

$$y(t) = \frac{v_{0y}}{\beta}\sin(\beta t) + \frac{v_{0x}}{\beta}\cos(\beta t) - \frac{v_{0x}}{\beta} + y_0$$

$$z(t) = v_{0z}t + z_0$$

$$v_x(t) = v_{0x}\cos(\beta t) + v_{0y}\sin(\beta t)$$

$$v_y(t) = v_{0y}\cos(\beta t) - v_{0x}\sin(\beta t)$$

$$v_z(t) = v_{0z}$$

where $\mathbf{r}_0 = (x_0, y_0, z_0)$ and $\mathbf{v}_0 = (v_{0x}, v_{0y}, v_{0z})$ are the intial position and velocity. For Test 3 there is not an analytical solution for the particle motion

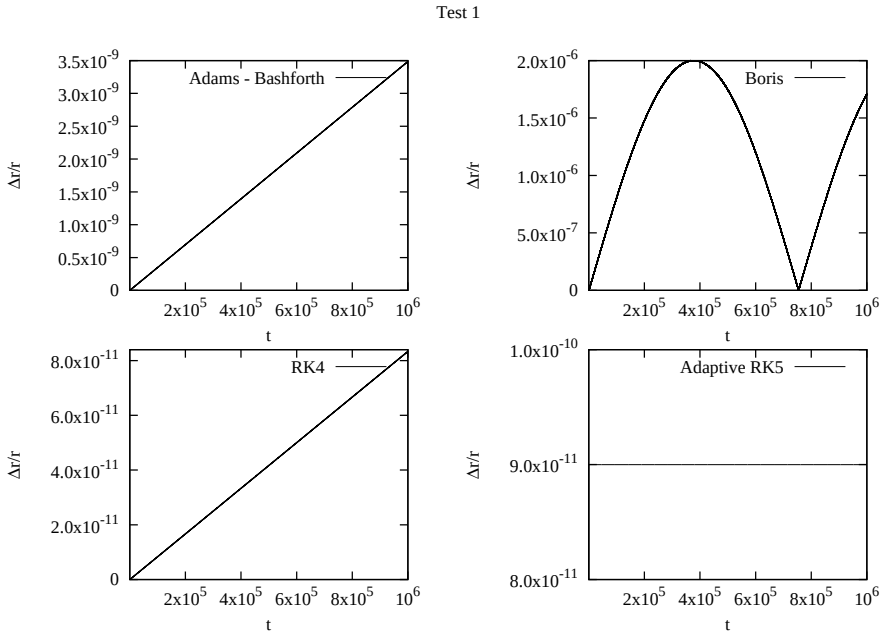

Figure B.1: TEST 1. Difference of position for numerical and analitical solution normalized to the lenght of the trajectory.

and so it is used only to test each method capability to conserve energy. We report here a series of plots and tables that summarizes the results obtained. In Figure B.1 we plot the error on the trajectory made by the four method for Test 1. If we call $\mathbf{r}(t)$ the numerical solution and $\mathbf{r_e}(t)$ the exact analitical solution at time t, we can define the relative error on the trajectory Δr as:

$$\Delta r(t) = |\mathbf{r}(t) - \mathbf{r}_e(t)|\,.$$

In order to have a relative error we normalize Δr to the total distance run by the particle, that considering the speed constant because of energy conservation gives:

$$\frac{\Delta r}{r} = \frac{|\mathbf{r}(t) - \mathbf{r_e}(t)|}{v \Delta t N_t}.$$

The minimum value of the maximum error this time is owned by the RK4, but the trends of the errors in time are very different one from the other. RK4 and AB present a linear growing trend and Boris a periodic one. The latter is due to the fact that Boris method makes a phase error Qin et al. (2013) that sums at each step and periodically brings the error to oscillate between a maxium value that corresponds to the diameter of the gyration and a minimum value that is $\sim 10^{-9}$. It is worth to give a separate explanation to what happens for the ARK5. We see that the relative error is almost constant. It may look strange that the magnitude of the error is larger than the RK4. This strange behaviour is due to the fact that at the first step the fifth order method makes an error larger than the fourth order, after that step its behaviour shows a better control on the trajectory error than the RK4. This is an example that shows that it is not always true that higher order leads to higher precision. In Figure B.2 we plot the error on energy. If we call $E(t)$ the numerical energy at time t and E the exact initial energy, that should be conserved, we can define the error on energy as:

$$\frac{\Delta E}{E} = \frac{E(t) - E}{E}.$$

We can see that for all the methods the error on energy grows linearly in time in absolute value and that the Boris method best conserve energy. In Figure B.3 and B.4 we have the two errors already discussed for Test 1 in the case of Test 2 where a not null component of the velocity parallel to the

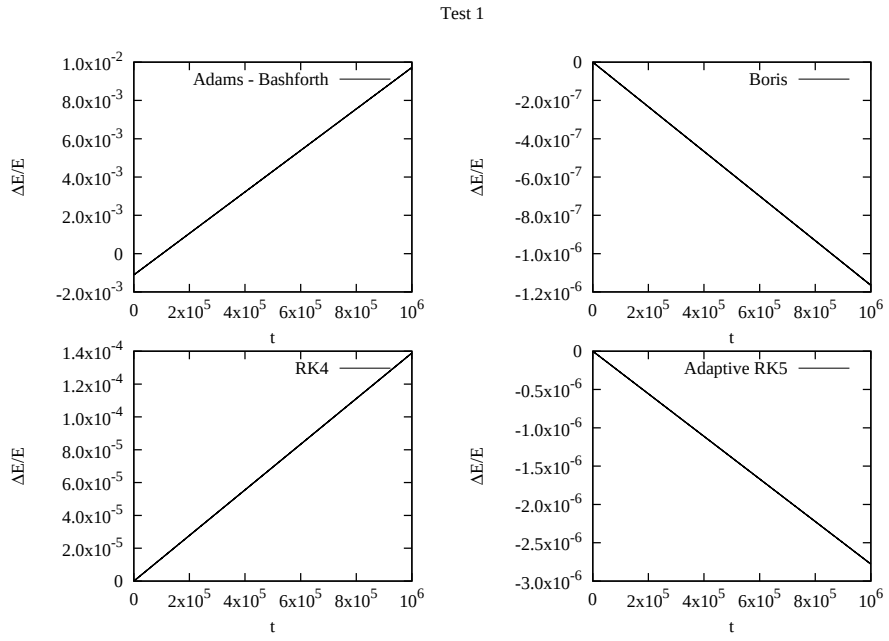

Figure B.2: TEST 1. Relative error of the numerical energy compared to the initial value.

magnetic field is added. Also in this case the RK methods better describe the correct trajectory and the Boris method best conservs energy. In Figure B.5 we plot the error on energy for Test 3. The motionof the particle in this case is chaotic and this has a great impact in the conservation of energy for the four methods. The Boris method beats the other method by several order of magnitudes showing a very slow not linear growing. For the other three method the error grows more rapidly in time in absolute value the evolution presenting different growing rates. As a conclusion of this tests we can say that for a periodic motion with only one scale involved the RK methods better approximate the exact trajectory, but this represent a very singular case. When the motion is not periodic and we cannot monitor the trajectory error Boris method maintain the best conservation of energy. In Tables B.1, B.2, and B.3 we have also reported the computational times of

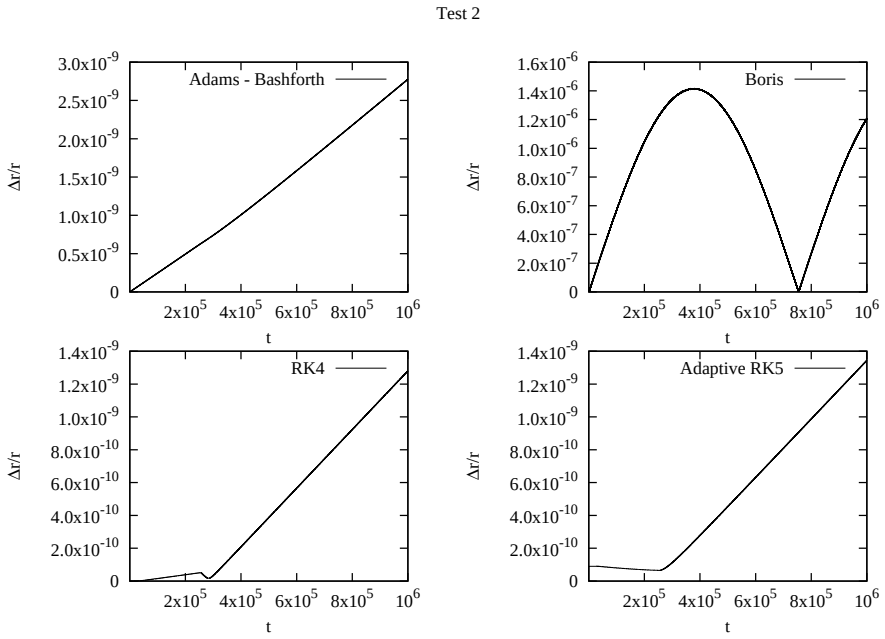

Figure B.3: TEST 2. Difference of position for numerical and analitical solution normalized to the lenght of the trajectory.

each simulation, showing that for RK methods where multiple evaluation of the derivative at each time step are involved, the computational time become much larger and this makes them uncomfortable when a large number of time step have to be taken (10^8 in our case).

Test 1	$\max(\Delta r/r)$	$\max(\lvert\Delta E/E\rvert)$	cpu time
Adam-Bashfort	3.5×10^{-9}	1.0×10^{-2}	$2.5s$
Boris	2.0×10^{-6}	1.2×10^{-6}	$3.3s$
RK4	8.0×10^{-11}	1.4×10^{-4}	$8.5s$
adaptive RK5	9.0×10^{-11}	3.0×10^{-6}	$12.7s$

Table B.1: Relative error in position and energy, and computational times for Test 1.

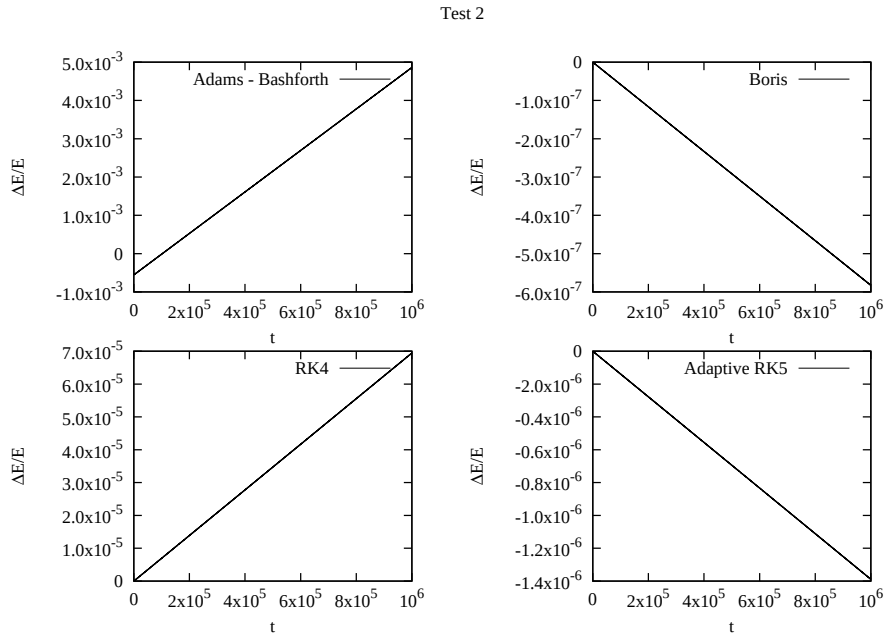

Figure B.4: TEST 2. Relative error of the numerical energy compared to the initial value.

Test 2	$\max(\Delta r/r)$	$\max(\lvert\Delta E/E\rvert)$	cpu time
Adam-Bashfort	2.5×10^{-9}	5.0×10^{-3}	$2.6s$
Boris	1.4×10^{-6}	6.0×10^{-7}	$3.7s$
RK4	1.3×10^{-9}	7.0×10^{-5}	$8.6s$
adaptive RK5	1.3×10^{-9}	1.4×10^{-6}	$13.1s$

Table B.2: Relative error in position and energy, and computational times for Test 2.

Tests on particle diffusion

Since we are interested in studying diffusion of a big number of particles it is a good question to ask if one of the methods we have discussed enhanches or reduces diffusion respect to another one. For this reason we performed simulations of test particle diffusion in a magnetic field obtained by the synthetic turbulence model described in Chapter 4. We inject 10^3 particles with random initial position in a cubic box $C = [0, 1] \times [0, 1] \times [0, 1]$, with

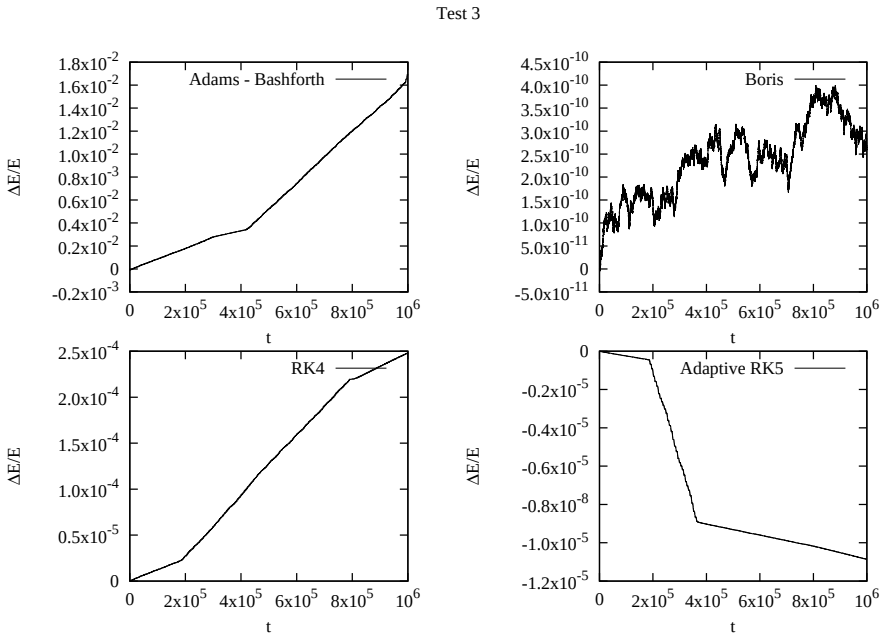

Figure B.5: TEST 3. Relative error of the numerical energy compared to the initial value.

Test 3	$\max(\lvert\Delta E/E\rvert)$	cpu time
Adam-Bashfort	1.7×10^{-2}	$18.4s$
Boris	4.0×10^{-10}	$19.7s$
RK4	2.5×10^{-4}	$1m12s$
adaptive RK5	1.1×10^{-5}	$1m48s$

Table B.3: Relative error energy, and computational times for Test 3.

equal speed $v = 10^{-3}$ and random directions, the time step is always $\Delta t = 10^{-2}$ and the total number of steps is 10^7. We consider a strong level of turbulence $\eta = 1$, a magnetic spectrum that extends beyond the Larmor scale $\xi = 1024$ and different level of intermittency (see Chapter 4). The first thing we found is that the fourth other Adam-Bashfort is not stable for this problem, the energy goes to infinity at large time. For this reason we decide to discard this method. We discard also the RK4 method, since it can be considered as a simplified version of the RK5 with adaptive time-step. The

results of the test is plotted in Figure B.6. The diffusion coefficients $D_{\parallel}$ and $D_{\perp}$ are defined as:

$$D_{\parallel}(t) = \frac{1}{2N_p t} \sum_{i=1}^{N_p} (z_i(t) - z_i(0))^2$$

$$D_{\perp}(t) = \frac{1}{2N_p t} \sum_{i=1}^{N_p} (x_i(t) - x_i(0))^2 + (y_i(t) - y_i(0))^2$$

where the index i refers to a single particle and N is the total number of particles. The agreement between diffusion coefficients computed with Boris method and the RK5 is good for all the value of intermittency considered. This means that the two methods are interchangeable for this problem. The reason why we didn't run the simulation for 10^8 steps is that the computational time for the RK5 would have been too big.

At the end of all these analysis we decided to use the Boris method as numerical integrator for our study on particle diffusion. This choice is based on several reasons that came out from the various tests. First of all the Boris method, being sympletic, is the best of the four in conserving energy, expecially when particle dynamics is chaotic. It is also very fast in respect of the RK methods and even if it makes a phase error while describing the gyration of a particle this does not affect the diffusion coefficients evolution, that is comparable to the one obtained with the RK5. Finally, the reason why we decided to reject the AB method is that pushing it forward for 10^8 time steps it turns out to be unstable.

We decide also to took a different decision for the method used in the problem of particle acceleration in RMHD, where we used the RK5 with adaptive time step, that is the stepper commonly used for this type of problems in literature (Dmitruk et al., 2004; Dalena et al., 2014). In fact, this is

a completely different problem, where the electric field is present and energy is not conserved. Moreover, even if we consider a bigger number of particle (10^5, compared to 10^3 for particle diffusion), the number of time step to be taken for each particle in this simulation is way smaller (of the order of 10^4) and the evalution of the fields at each time step is faster than for the STM. This makes the computational time using the RK5 reasonable for this problem. Of course, the Boris method would have been way faster, but an analysis similar to what done for the particle diffusion problem would have been required in order to compare the results from the two methods. We decided to leave this work for further studies.

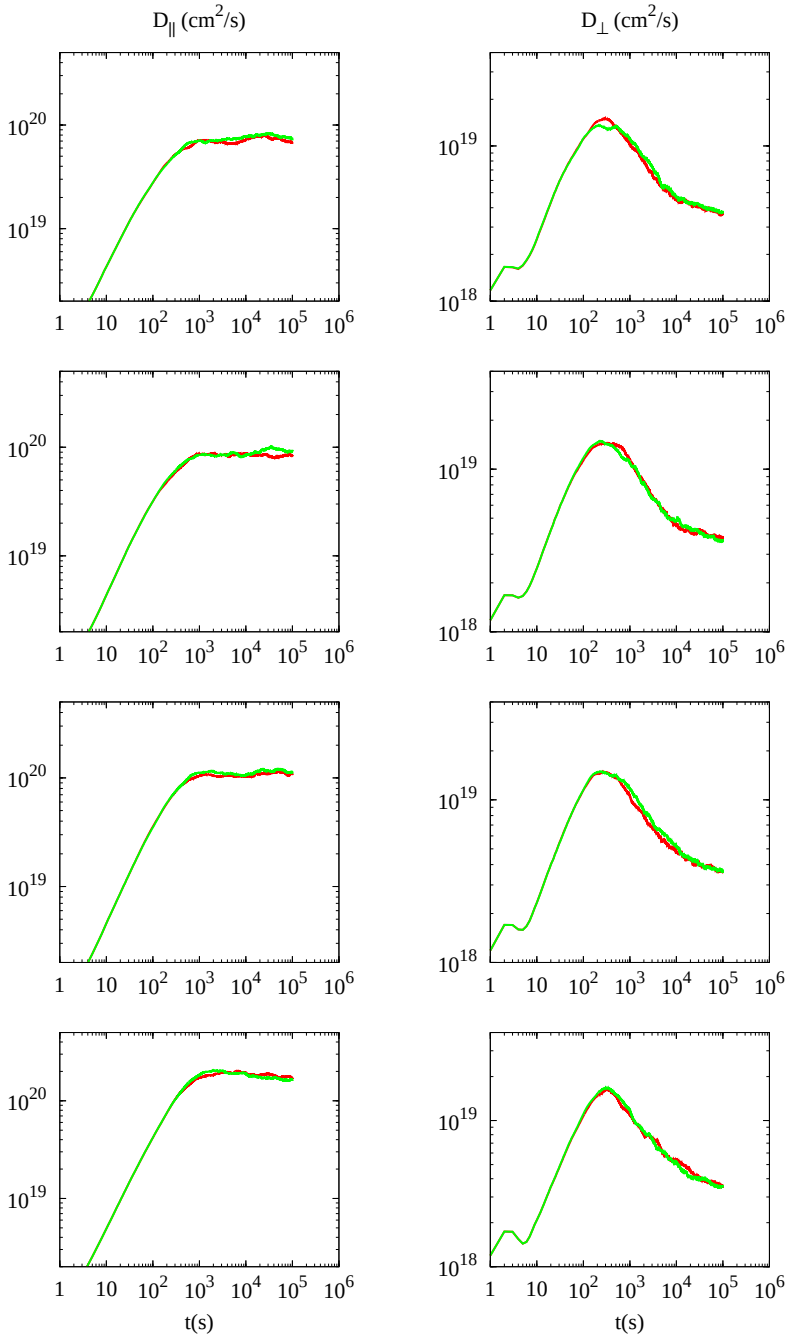

Figure B.6: Parallel and perpendicular diffusion coefficient computed using Boris method (red lines) and RK5 (green lines), for the different values of the intermittency parameter p used in Chapter 4 ($p = 0.5$ first row, $p = 0.7$ second row, $p = 0.8$ third row, and $p = 0.9$ fourth row).

Appendix C

A numerical code for test particle simulations

The numerical simulations relative to the studies of particle diffusion and acceleration presented in this work have been performed using a numerical code realized to run test particle simulations. In this appendix we describe its features and discuss its performances. The code is parallized using the Open Multiprocessing (OMP) paradigm. The reasons why we used OMP instead of Message Passing Interface (MPI) are several. First of all test particle simulations consist in computing the solution of the Lorentz equation for the motion of particles that are indipendent one to the other. This implies that also the processes associated to each particle are indipendent one to the other and do not need to exchange information, except if the calculation of average quantities along the run is required. This is not required in our case, and the calculus of average quantities is postponed at the end of each run, while the output is analysed. For this reason an MPI architecture is not strictly required by the nature of the computational problem. Secondly, an OMP architecture is easier to deal with, it requires a few commands and can

be implemented on an already existing serial code. What we did is to realize a serial version of the code and then implement the parallelization using OMP commands. An MPI parallelization would have required a completely different approch and could not have been implemented on an already existing program. Finally, in the OMP approch the memory is shared among all the processors and this turns out to be very useful for our case since the private memory available on each processor in the machine we used was not big. In our biggest simultions that involves the use of fields obtained from Reduced MHD simulations data the common memory to be stored was of the order of hundreds of GBs. Of course there are ways to overcome this difficulties with the MPI architecture but they are more cumbersome to implement. An MPI program is usually more powerful than an OMP one, expecially if a big amount of computational power is available, but in our particular case with limited computational resources an MPI parallelization would have not produced a big gain in terms of computational time respect to an OMP one. We think so because the OMP parallel region in the code we realized is way bigger that the serial part, as we are going to explain describing the structure of the MAIN.

The `MAIN` (reported below) uses the module `omp_lib` that contains OMP libraries, the module `PARA` that contains almost all the parameters used by the program and the module `INPUTMOD` where the subroutine called in the program along with other subroutines, cited below, are written. The initialization part begins with the declaration of some variables and the creation of the folder where the output will be written (the name of the folder is written in the module `PARA`). Two integer values are assigned to the variables that represent the units of the files where the initial and final values of position and velocities will be written. This files are open a little bit

further in the initialization part and remain open along all the simulation. Their name contain a label indicating which time stepper has been used in the simulation. This label changes with the method, that is identified by an integer number `ODESTEP` declarated in the module `PARA`. In the initialization the arrays that contain the magnetic and electric field in space and time are allocated and they are fill by the data from simultion by mean of the subroutine `READ_FIELDS`. This part can be commented when a synthetic model for computing the fields is used and no data has to be read, as in the case of particle diffusion described in this work. The initial serial part ends with the assignement of the value `tin` (declared in `PARA`) to the variable `t` representing time. The computing part that is the central and bigger part of the code is where the OMP paralellization is set in. It consists in the loop of the computation of the solution of the equation of a single particle nested into the loop on each particles. The first one is parallelized with the OMP command `OMP DO PARALLEL` using a dynamic assignement of processes. Inside this loop a file is open for each particle where the values of position, velocity, energy and magnetic moment can be written at each chosen time (defined by an integer parameter `iprint`). A different file unit is associated to each particle. Particle position and velocity are initialized through the subroutine `INITIALIZE`. A random number generator routine is supplemented to this subroutine and can be used to assign a random initial position or velocity to the particle. After the initialization the initial energy and magnetic moment are computed and are written along with position and velocity in the initial conditions file. The magnetic moment is computed through the subroutine `FIELDS` that gives the value of the electric and magnetic fields at a given position and time. The form of this subroutine varies with the problem studied. In the problem of particle diffusion described in this work

the subroutine contains the synthetic turbulence model, instead in the problem of particle accelaration in RMHD fields the subroutine contains all the operation necessary to interpolate the value of the fields in space and time. In the inner loop the user has the possibility to choose among three different time stepper: the Boris method (subroutine boris_derivs), an adaptive fifth order Runge-Kutta (subroutine odeint, see Press et al. (1992)), and a forth-order Runge Kutta (subroutine RK4, see Press et al. (1992)).

These three scheme are described in Appendix B. In the closure part the arrays where the fields are stored are deallocated, the final values of position, velocity, and energy are written in the file opened at the beginning and the computational time is computed.

This is the `MAIN` :

```
PROGRAM MAIN

USE INPUTMOD
USE omp_lib
USE para

IMPLICIT NONE

real*8 :: t
integer :: iline,i
integer, PARAMETER :: neq=6
real*8,  dimension (neq) :: y             ! position and velocity vector
real*8 :: Initial_Kenergy,kene            ! kinetic energy
real*8 :: tinitial,tfinal,oinitial,ofinal ! computational time
integer :: istep
character (5) :: method
character (10) :: ciline
integer :: MythreadID, Numthreads
integer :: itve, iip, ife
real*8, dimension (1:NLINE,7) :: frve
real*8, dimension (1:NLINE,6) :: inipos
real*8, dimension (3) :: Ef,Bf
```

```
real*8 :: mu,modv,modb,costh
integer :: ipart

 call cpu_time(tinitial)
 call system ('mkdir '// dir)
 call system ('mkdir '// dir //'/results')

 iip=200+NLINE
 ife=200+NLINE+1

 SELECT CASE(ODESTEP)
 CASE (1)
 write(method,'(A1)') 'B'
 CASE (2)
 write(method,'(A1)') 'A'
 CASE (3)
 write(method,'(A3)') 'RK4'
 END SELECT

 open (unit=iip, file=trim(dir)//'/'//trim(method)// &
                       '-ini.dat', status='UNKNOWN')
 open (unit=ife, file=trim(dir)//'/'//trim(method)//&
                 '-final_nrg.dat', status='UNKNOWN')

!$ oinitial=omp_get_wtime()

 ALLOCATE(Bfldx(NGRID(1),NGRID(2),NGRID(3),isamplein:isamplefin))
 ALLOCATE(Bfldy(NGRID(1),NGRID(2),NGRID(3),isamplein:isamplefin))
 ALLOCATE(Efldx(NGRID(1),NGRID(2),NGRID(3),isamplein:isamplefin))
 ALLOCATE(Efldy(NGRID(1),NGRID(2),NGRID(3),isamplein:isamplefin))
 ALLOCATE(Efldz(NGRID(1),NGRID(2),NGRID(3),isamplein:isamplefin))

 CALL READ_FIELDS()                ! fields reading

 t=tin

!$omp parallel private (MYThreadID,iline,ciline,y,Initial_Kenergy, &
                       t,istep,kene,itve,Ef,Bf,modv,modb,costh,mu)
!$     MythreadID=omp_get_thread_num()
```

```
!$     Numthreads=omp_get_num_threads()
!$omp do schedule (dynamic,1)                    ! parallel region beginning
 DO iline = 1, NLINE                             ! cycle on the particles

 IF (iline .lt. 10) then
  write(ciline,'(A5,I1)') '00000',iline
  ELSE
   IF (iline .lt. 100) then
   write(ciline,'(A4,I2)') '0000',iline
   ELSE
    IF (iline .lt. 1000) then
    write(ciline,'(A3,I3)') '000',iline
   ELSE
    IF (iline .lt. 10000) then
    write(ciline,'(A2,I4)') '00',iline
    ELSE
     IF (iline .lt. 100000) then
     write(ciline,'(A1,I5)') '0',iline
     ELSE
      write(ciline, '(I6)') iline
     ENDIF
    ENDIF
   ENDIF
  ENDIF
 ENDIF
ENDIF

itve= 100+MythreadID
open (itve, file=trim(dir)//'/'//trim(method)//'-trajvelenemu' &
                      //trim(ciline)//'.dat', status='UNKNOWN')

CALL INITIALIZE (y,neq,iline)                   !particles initialization

t=tin
Initial_Kenergy=0.5d0*(y(4)*y(4)+y(5)*y(5)+y(6)*y(6))

CALL FIELDS(Ef,Bf,y,t)
modv=dsqrt(y(4)*y(4)+y(5)*y(5)+y(6)*y(6))
modb=dsqrt(Bf(1)*Bf(1)+Bf(2)*Bf(2)+Bf(3)*Bf(3))
costh=(y(4)*Bf(1)+y(5)*Bf(2)+y(6)*Bf(3))/(modv*modb)
```

```
 mu=(modv*modv*(1.d0-costh*costh))/(2*modb)
 if (modv==0) then
 mu=0.d0
 endif

 write(100+MythreadID,'(8F21.14)')  y(1), y(2), y(3), y(4),&
                           y(5), y(6), Initial_Kenergy, mu

 inipos(iline,1)=y(1)
 inipos(iline,2)=y(2)
 inipos(iline,3)=y(3)
 inipos(iline,4)=y(4)
 inipos(iline,5)=y(5)
 inipos(iline,6)=y(6)

  DO   istep = 1, NTMAX              ! time cycle for each particle evolution

   !CALL boris_derivs(y,dt,t)
    CALL odeint(y,neq,t,t+dt,INTERR,dt_guessed,dt_min,derivs,rkqs)
   !CALL rk4(y,neq,t,dt,derivs)

    t=istep*dt+tin
    kene=0.5d0*(y(4)*y(4)+y(5)*y(5)+y(6)*y(6))

    IF (MOD(istep,iprint) == 0) THEN
    modv=dsqrt(y(4)*y(4)+y(5)*y(5)+y(6)*y(6))
    modb=dsqrt(Bf(1)*Bf(1)+Bf(2)*Bf(2)+Bf(3)*Bf(3))
    costh=(y(4)*Bf(1)+y(5)*Bf(2)+y(6)*Bf(3))/(modv*modb)
    mu=(modv*modv*(1.d0-costh*costh))/(2*modb)
    write(itve,'(8F21.14)') y(1), y(2), y(3), y(4),&
                              y(5), y(6), kene, mu
    ENDIF
  ENDDO

! write(*,*) 'iline=', iline, MythreadID
  frve(iline,1:3)=y(1:3)
  frve(iline,4:6)=y(4:6)
  frve(iline,7)=kene
```

```
  close(itve)

END DO                                ! time cycle ending
!$omp end do
!$omp end parallel                    ! parallel region ending

 do i=1,NLINE
  write(iip,'(6F21.14)') inipos(i,1),inipos(i,2),inipos(i,3), &
                         inipos(i,4),inipos(i,5),inipos(i,6)
  write(ife,'(7F21.14)') frve(i,1),frve(i,2),frve(i,3), &
                         frve(i,4),frve(i,5),frve(i,6),frve(i,7)
 enddo

 DEALLOCATE (Bfldx,Bfldy,Efldx,Efldy,Efldz)

!$ ofinal=omp_get_wtime()              ! computational time extimation
!$ write(*,'(" oTime = ",f6.3," seconds.")'), ofinal-oinitial
!$ write(*,'(" Number of threads=",I2)'),Numthreads
 call cpu_time(tfinal)

END PROGRAM MAIN
```

The code performances have been tested. The first test consisted in a simulation of 10^4 particles whose trajectories have been evolved for 10^3 time steps with the adaptive Runge-Kutta scheme described in Appendix B using RMHD data for the electric and magnetic fields. The second test consists in a simulation of 10^2 particles whose trajectories have been evolved for 10^4 time steps with the Boris method using the synthetic turbulence model presented in this work (see Chapter 4). Performances are evaluted plotting the speed-up in function of the number of processes (or threads). Speed-up Sp is defined as:

$$Sp = \frac{T_s}{T_p}$$

where T_s is the computational time with one processor (serial) and T_p is

the computational time for each processor when more than one processor is used (parallel). Speed-up in OMP is relevant only in the case when the majority of the computational time is spent in the parallel region. This is what happen in our simultation, so speed-up actually represents a good parameters to evalute our code performances. In Figure C.1 and C.2 the speed-up is plotted for the problem of test particle in RMHD and for the problem of test particle diffusion, along with the function $Sp = n_p$, the last one representing the ideal case in which the speed-up grows linearly with the number of processors. In the first case the speed-up grows less then linearly with n_p and strats saturating to $Sp \approx 6.5$ at $n_p = 12$. In the second case the speed-up grows almost linearly with a small number of processors and then strats saturating to $Sp \approx 13$ at $n_p = 16$. Even if the number of processes at which the speed-up saturates is not so high in both cases, it was sufficient for us to run the simulation presented in this work in a couple of hours per run.

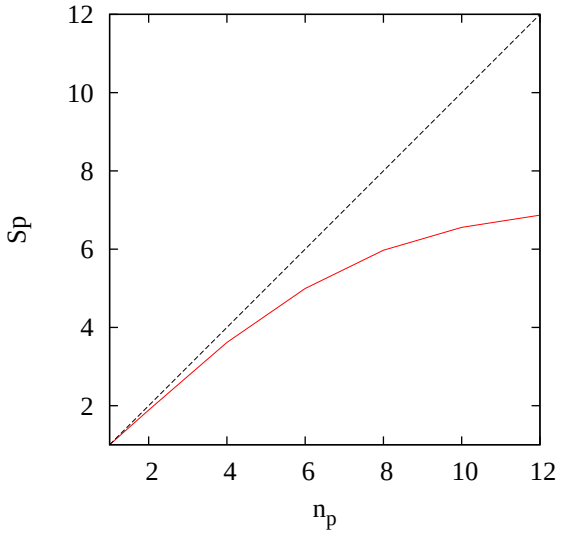

Figure C.1: Speed-up in function of the number of processors (thread), for 10^4 particles, 10^3 time steps per particle, and the adaptive fifth order Runge-Kutta as time stepper, in a test particle simulation that uses RMHD data for electric and magnetic fields.

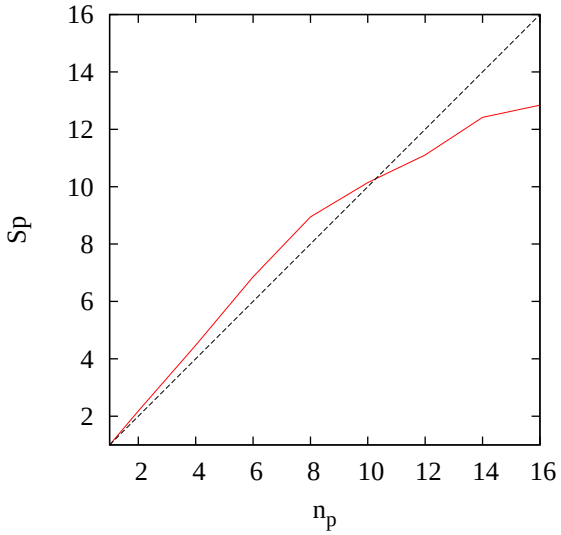

Figure C.2: Speed-up in function of the number of processors (thread), for 10^2 particles, 10^4 time steps per particle, and the Boris method as time stepper, in a test particle simulation where the magnetic field is computed with the syntetic turbulence model described in Chapter 4.

Bibliography

Acton, L. W., Culhane, J. L., Wolfson, C. J., Rapley, C. G., Phillips, K. J. H., Antonucci, E., Bentley, R. D., Hayes, R. W., Joki, E. G., Jordan, C., Kayat, M. A., Kent, B., Leibacher, J. W., Nobles, R. A., Parmar, A. N., Strong, K. T., & Veck, N. J., 1981, The Astrophysical Journal, 224, L137

Ambrosiano, J., Matthaeus, W. H., Goldstein, M. L., & Plante, D. 1988, Journal of Geophysical Research, 93, A12, 14,383

Bale, S. D., Kellog, P. J., Mozer, F. S., Horbury, T. S. & Reme, H. 2005, Physical Review Letters, 94, 215002

Banerjee, D., Gupta, G. R., & Teriaca L. 2011, Space Science Review, 158, 267

Belcher, J. W., & Davis, L. 1971, Journal of Geophysical Research, 76, 3534

Birkhoff, G., & Mac Lane, S., A survey of Modern Algebra, 4th Ed. (Macmillan Publishing Co., Inc, New York, NY, 1977) pp. 118-120.

Bitane, R., Zimbardo, G., & Veltri, P. 2010, The Astrophysical Journal, 719, 1912–1917

Buchlin, E., Cargill, P. J., Bradshaw, S. J. & Velli, M. 2007, Astronomy & Astrophysics, 469, 347

Chae, J., Schühle, U., & Lemaire, P. 1998, The Astrophysical Journal, 505, 2, 957

Cirtain, J. W., Golub, L., Lundquist, L. et al. 2007, Science, 318, 1580

Califano, F., Chiuderi, C., & Einaudi, G. 1990, The Astrophysical Journal, 365,757

Califano, F., Chiuderi, C., & Einaudi, G. 1992, The Astrophysical Journal, 390,560

Cametti, F., Carbone, V., & Veltri P. 1998, Le Journal de Physique IV France, 08, 197

Carbone, V., & Veltri, P. 1990, Geophys. Astrophys. Fluid Dynamics, 52, 153

Chen, C. H. K., Boldyrev, S., Xia, Q., & Perez, J. C. 2013, Physical Review Letters, 110, 225002

Cranmer, S. R., & van Ballegooijen, A. A. 2003, The Astrophysical Journal, 594, 573

Cranmer, S. R., van Ballegooijen, A. A., & Edgar, R. J. 2007, The Astrophysical Journal Supplement, 171, 520

Casse, F., Lemoine, M., & Guy, P. Physical Review D, 65, 023002

Dalena, S., Rappazzo, A. F., Dmitruk, P., Greco, A., & Matthaeus 2014, The Astrophysical Journal, 783:143

S. Dalla, A. Balogh, S. Krucker, et al. 2003, Geophysical Research Letters, 30, 19

Davila, J. M. 1987, The Astrophysical Journal, 317, 514

Décamp, N., & Malara F. 2006, Electron Acceleration in Turbulent Coronal Loops by Kinetic Alfvén Waves, in "SOHO-17. 10 Years of SOHO and Beyond", H. Lacoste & L. Ouwehand Eds., ESA SP-61

DeForest, C. E., Hoeksema, J. T., Gurman, J. B., Thompson, B. J., Plunkett, S. P., Howard, R., Harrison, R. C. & Hassler, D. M. 1997, Solar Physics, 175, 393

DeForest, C. E. & Gurman, J. B. 1998, The Astrophysical Journal, 501, L217

Dmitruk, P., Matthaeus, W. H., & Seenu, N. 2004, The Astrophysical Journal, 617:667-679

Dmitruk, P., Matthaeus, W. H., Seenu, N., & Brown, M. R. 2003, The Astrophysical Journal, 597:L81-L84

Dmitruk, P., Gómez, D., & Matthaeus, W. 2003, Physics of Plasmas, 10, 9

P. Duffy, J. G. Kirk, Y. A. Gallant, & R. O. Dendy 1995, Astronomy & Astrophysics, 302, L21

R. K. Galloway, P. Helander, & A. L. MacKinnon 2006, The Astrophysical Journal, 646, 615

Gary, S. P., & Nishimura, K. 2004, Journal of Geophysical Research, 109, A02109

S. Ghosh, M. Hossain, and W. H. Matthaeus, Computer Physics Communications, 74, 18 (1993).

Ghosh, S, Matthaeus WH, Roberts DA & Goldstein ML 1998, Journal of Geophysical Research 103, 23691

Giacalone, J. 2013 Space Science Review 176, 73

J. Giacalone & J. R. Jokipii 1999, The Astrophysical Journal, 520, 204

Grappin, R., Léorat, J., & Buttighoffer, A. 2000, Astronomy & Astrophysics, 362,342

Greco, A., Matthaeus W. H., Servidio, S., Chuychai, P., & Dmitruk 2009, The Astrophysical Journal, 691:L111-L114

Greco A., Valentini F., Servidio S. & Matthaeus W. H. 2012, Physical Review E, 86, 066405

Hellinger, P., Trávníček, P. M., Štěpán Štverák, Matteini, L. & Velli, M. 2013, Journal of Geophysical Research 118, 1351

Heyvaerts, J., & Priest, E. R. 1983, Astronomy & Astrophysics, 117, 220

Hollweg, J. 1987, The Astrophysical Journal, 312, 880

Hollweg, J., 1999, Journal of Geophysical Research 104, 47

Hollweg, J., & Isenberg, P. 2002, Journal of Geophysical Research, 107, 1147

Howes, G. G., Cowley, S. C., Dorland, W., Hammett, G. W., Quataert, E., Schekochihin, A. A., & Tatsuno, T. 2008a, Physical Review Letters 100, 065004

Howes, G. G., Dorland, W., Cowley, S. C., Hammett, G. W., Quataert, E., & Schekochihin, A. A. 2008b, Journal of Geophysical Research 113, A05103

Inglis, A. R., Nakariakov, V. M., & Melnikov, V. F. 2008, Astronomy & Astrophysics, 487, 1147

Ito , H., Tsuneta, S., Shiota, D., Tokumaru, M., & Fujiki, K. 2010 The Astrophysical Journal, 719, 131

Juneja, A., Lathrop, D. P., Sreenivasan, K. R., & Stolovitzky, G. 2004, Physical Review E, 49, 5179

Kappraff, J. M., & Tataronis, J. A. 1977, Journal of Plasma Physics, 18, 209

Kiyani, K. H., Chapman, S. C., Sahraoui, F., Hnat, B., Fauvarque, O., & Khotyaintsev, Yu. V. 2013, The Astrophysical Journal, 763, 10

J. Kóta & J. R. Jokipii 2000, The Astrophysical Journal, 531, 1067

Landi, S., Velli, M., & Einaudi, G. 2005, The Astrophysical Journal, 624, 392

Lazarian, A., & Yan, H. 2014, The Astrophysical Journal, 784, 38

Lee, E. M., & Roberts, B. 1986, The Astrophysical Journal, 301, 430

Lin, R. P. 1974, Space Sci. Reviews, 16, 189–256

Lysak, R. L. & Song Y. (2011) Journal of Geophysical Research, 116, A00K14

Malara, F., Veltri, P., Chiuderi, C., & Einaudi, G. 1992, The Astrophysical Journal, 396, 297

Malara, F., Primavera, L., & Veltri, P. 1996, The Astrophysical Journal, 459, 347

Malara, F., Petkaki, P., & Veltri, P. 2000, The Astrophysical Journal, 533, 523

Malara, F., De Franceschis, M. F., & Veltri, P. 2003, Astronomy & Astrophysics, 412, 529

Malara, F., De Franceschis, M. F., & Veltri, P. 2005, Astronomy & Astrophysics, 443, 1033

Malara, F., Veltri, P., & De Franceschis, M. F. 2007, Astronomy & Astrophysics, 467, 1275

Malara, F., Nigro, G., Veltri, P., & Onofri, M. 2012, Space Science Review, 172, 157

Malara, F. 2013, Astronomy & Astrophysics, 549, A54,

Marino, R., Sorriso-Valvo, L., Carbone, V., Veltri, P., Noullez, A. & Bruno, R. 2011, Planetary and Space Science, 59, 592

Matthaeus, W. H. 1982, Journal of Geophysical Research Let., vol. 9, no. 6, 660

Matthaeus, W. H., Goldstein, M. L., & King, J. H. 1986, Journal of Geophysical Research, 91, 59

Matthaeus, W. H. & Brown, M. R. 1988, Physics of Fluids, 31, 3634

Matthaeus, W. H., Goldstein, M. L., & Roberts, D. A. 1990, Journal of Geophysical Rese

Matthaeus, W. H., Zank, G. P., Smith, C. W., & Oughton S. 1999, Physical Review Letters, 82, 3444

Matthaeus, W. H., Zank, G. P., Oughton, S., Mullan, D. J., & Dmitruk, P. 1999, The Astrophysical Journal, 523, L93

Matthaeus, W. H., Qin, G., Bieber, J. W., & Zank, P. G., 2003, The Astrophysical Journal, 590:L53-L56

Matthaeus, W. H., Dasso, S., Weyngand, J. M., Milano, L. J., Smith, C. W., & Kivelson, M. G. Physical Review Letters, 95, 231101

J. E. Mazur, G. M. Mason, J. R. Dwyer, J. Giacalone, J. R. Jokipii, and E. C. Stone 2000, The Astrophysical Journal, 532, L79

McAteer, R. T. J., Gallagher, P. T., Brown, D. S., et al. 2005, The Astrophysical Journal, 620, 1101

McComas, D. J., Barraclough, B. L., Funsten, H. O., Gosling, J. T., Santiago-Muñoz, E., Skoug, R. M., Goldstein, B. E., Neugebauer M., Riley, P. & Balogh, A. 2000, Journal of Geophysical Research, 105, 10419

McIntosh, S.W., De Pontieu, B., Carlsson, M., Hansteen, V., Boerner, P., & Goossens, M. 2011, Nature, 475, 477

R. B. McKibben 2005, Advances in Space Research, 35, 518

McLaughlin, J. A., De Moortel, I, Hood, A. W., & . Brady, C. S. 2009, Astronomy & Astrophysics, 493, 227

McLaughlin, J. A., Hood, A. W., & De Moortel, I. 2010, Space Science Review, doi:10.1007/s11214-010-9654-y

Mitra-Kraev, U., Harra, L. K., Williams, D. R., & Kraev E. 2005, Astronomy & Astrophysics, 436, 1041

Mok, Y., & Einaudi, G. 1985, Journal of Plasma Physics, 33, 199

Montgomery, D. C. 1982, Physica Scripta, Vol T2/1, 83-88

Murray, M. J., van Driel-Gesztelyi, L. & Baker, D. 2009, Astronomy & Astrophysics, 494, 329

Nakagawa, Y., Hu, Y. Q. & Wu, S. T. 1987, Astronomy & Astrophysics, 179, 354

Nakariakov, V. M., Roberts, B., & Murawski, K. 1997, Solar Physics, 175, 93

Nakariakov, V. M., Roberts, B., & Murawski, K. 1998, Astronomy & Astrophysics, 332, 795

Nigro., G., Malara, F., Carbone, V. & Veltri, P. 2004, Physical Review Letters, 92, 194501

Ofman, L., Romoli, M., Poletto, G., Noci, G. & Kohl, J. L. 1997, The Astrophysical Journal, 491, L111

Ofman, L., Nakarikov, V. M. & DeForest, C. E. 1999, The Astrophysical Journal, 514, 441

Ofman L. & Aschwanden M. J. (2002) The Astrophysical Journal, 576 L153

Onofri, M., Primavera, L., Malara, F. & Londrillo, P. 2007, Journal of Computational Physics, 226, 1874

Oughton, S., Priest, E. R. & Matthaeus W. H. 1994, Journal of Fluid Mechanics, 280, 95

Oughton, S., Matthaeus, W. H., Dmitruk, P., Milano, L. J., Zank, G. P., & Mullan, D. J. 2001, The Astrophysical Journal, 551:565-575

Perri, S. & Zimbardo, G. 2007, The Astrophysical Journal Letters, 671, 177–180

Perri, S., Zimbardo, G. 2009b, The Astrophysical Journal Letters, 693, L118–L121.

Perri, S., & Zimbardo, G. 2012a, The Astrophysical Journal, 750, 87

Perri, S. & Zimbardo, G. 2012 The Astrophysical Journal, 754, 8

Perrone D., Dendy R. O., Furno I., Sanchez R., Zimbardo G., Bovet A., Fasoli A., Gustafson K., Perri S., Ricci P & Valentini F. 2013, Space Sci Rev, 178, 233

Petkaki, P., Malara, F., & Veltri, P. 1998, The Astrophysical Journal, 500, 483

Podesta, J. J., & Tenbarge, J. M. 2012, Journal of Geophysical Research 117, A10106

Poinsot, T. J., & Lele, S. K. 1993, J. Comput. Phys., 101, 104

Pommois, P., Veltri, P. & Zimbardo, G., 2001, Physical Review E, 63, 066405

Pommois, P., Zimbardo, G., & Veltri, P. 2007, Physics of Plasmas, 14, 012311

Press, W. H., and Teukolsky, S. A., and Vetterling, W. T., and Flannery, B. P., Numerical Recipes 1992, Cambridge University Press

Priest, E. & Forbes, T., 2007, Cambridge University Press

Pucci, F., Onofri, M., & Malara 2014, The Astrophysical Journal, 796:43

Rappazzo, A. F., Velli, M., Einaudi, G., & Dahlburg, R. B. 2007, The Astrophysical Journal, 657:L41-L51

Rappazzo, A. F., Velli, M., Einaudi, G., & Dahlburg, R. B. 2008, The Astrophysical Journal, 677:1348-1366

Reames, D. V. 1999, Space Science Reviews, 90, 3, 413-491

Ruderman, M. S., Nakariakov, V. M., & Roberts, B. 1998, Astronomy & Astrophysics, 338, 1118

Qin, G., Matthaeus, W. H., & Bieber, J. W. 2002, Geophysical Research Letters, 29, 1048

Qin, G., Matthaeus, W.H., & Bieber, J.W. 2002, The Astrophysical Journal, 578, L117–L120

Qin, H., Shuangxi, Z., Jianyuan, X., Jian, L., Yajuan, S., & Tang, W. M. Physics of Plasmas, 20(8):084503

A. B. Rechester & M. N. Rosenbluth 1978, Physical Review Letters, 40, 38

Sahraoui, F., Goldstein, M. L., Robert, P., & Khotyaintsev, Yu. V. 2009, Physical Review Letters 102,231102

Sahraoui, F., Belmont, G., & Goldstein, M. L. 2012, The Astrophysical Journal, 748, 100

Salem, C. S., Howes, G. G., Sundkvist, D., Bale, S. D., Chaston, C. C., Chen, C. H. K., &Mozer, F. S., 2012, The Astrophysical Journal, 745, L9

Schekochihin, A. A., Cowley, S. C., Dorland, W., Hammett, G. W., Howes, G. G., Quataert, E., & Tatsuno, T. 2009, The Astrophysical Journal, 182, 310

A. Shalchi, J. W. Bieber, & W. H. Matthaeus 2004, The Astrophysical Journal, 604, 675

Shalchi, A., and Kourakis, I. 2007, Astronomy & Astrophysics, 470, 405–409.

Shalchi, A. A. 2010, The Astrophysical Journal, 720, L127–L130

Shalchi, A. 2015 The Astrophysical Journal, 799:232

Shibata, K., Nakamura, T., Matsumoto, T., et al. 2007, Science, 318, 1591

Shebalin, J. V., Matthaeus, W. H., & Montgomery, D. 1983, Journal of Plasma Physics, 78, 2088

Similon, P. L., & Sudan, R. N. 1989, The Astrophysical Journal, 336, 442

Sorriso-Valvo, L., Marino, R., Carbone, V., Nullez, A., Lepreti, F., Veltri, P., Bruno, R., Bavassano, B. & Pietropaolo, E. 2007, Physical Review Letters, 99, 115001

Steinolfson, R. S. 1985, The Astrophysical Journal, 295, 213

Strauss, H. R. 1976, Physics of Fluids, 19, 134

Sun, M. T., Wu, S. T. & Dryer, M. 1995, J. Comput. Phys, 116, 330

Suzuki, T. K., & Inutsuka, S.-I. 2005, The Astrophysical Journal, 632, L49

Tautz, R. C., Shalchi, A. 2010, Journal of Geophysical Research, 115, A03104

TenBarge, J. M., & Howes, G. G. 2012, Phys. Plasmas 19, 055901

A. Teufel & R. Schlickeiser 2002, Astronomy & Astrophysics, 393, 703

Tomczyk, S., McIntosh, S. W., Keil, S. L., Judge, P. G., Schad, T., Seeley, D. H., & Edmondson, J. 2007, Science 317, 1192

Tomczyk, S., & McIntosh, S. W. 2009, The Astrophysical Journal, 697, 1384

Tsiklauri, D., & Nakariakov, V. M. 2002, Astronomy & Astrophysics, 393, 321

Tsiklauri, D., Nakariakov, V. M., & Rowlands, G. 2003, Astronomy & Astrophysics, 400, 1051

Tsiklauri, D., Sakai, J.-I., & Saito S. 2005, Astronomy & Astrophysics, 435, 1105

Tsiklauri, D. 2011, Physics of Plasmas, 18, 092903

Tsiklauri, D. 2012, Physics of Plasmas, 19, 082903

Turkmani, R., Vlahos, L., Galsgaard, K., Cargill, P. J., & Isliker, H. 2005, The Astrophysical Journal, 620:L59-L62

Van Doorsselaere, T., Nakariakov, V. M. & Verwichte E. 2008, The Astrophysical Journal, 676, L73

Valentini, F., Travnicek, P., Califano, F., Hellinger, P., Mangeney, A. 2007, Journal of Computational Physics 225, 753

Vásconez, C. L., Pucci, F., Valentini, F., Servidio, S., Matthaeus, W., H., & Malara F. 2015, The Astrophysical Journal, in press

Vásconez, C. L., Valentini, F., Camporeale, E. & Veltri P. 2014, Physics of Plasmas, 21, 112107

Verdini, A., & Velli, M. 2007, The Astrophysical Journal, 662, 669

Verdini, A., Velli, M., & Buchlin E. 2009 The Astrophysical Journal, 700, L39

Verdini, A., Velli, M., Matthaeus, W. H., Oughton, S., & Dmitruk, P. 2010 The Astrophysical Journal, 708, L116

Verkhoglyadova, O.P., Zank, G. P., & Li, G. 2015, Physics Reports, 557, 1-23

Voitenko, Y.,& Goossens, M. 2004, The Astrophysical Journal, 605, L149

Wan, M., Matthaeus, W. H., Servidio, S., & Oughton, S. 2013, Physics of Plasmas, 20, 042307

Wang, Y.-M., Sheeley, N. R., Jr. & Rich, N. B. 2007, The Astrophysical Journal, 658, 1340

Wang, Y.-M., Grappin, R., Robbrecht, E & Sheeley, N. R., Jr. 2012, The Astrophysical Journal, 749, 182

Warren, H. P., Mariska, J. T., Wilhelm, K., & Lamaire, P. 1997, The Astrophysical Journal, 484, L91

Webb, G. M., Zank, G. P., Kaghashvili, E. Kh., le Roux, J. A. 2006, The Astrophysical Journal, 651, 211–236.

Webb, S. 2014, Journal of Computational Physics, 270:570-576

Wu, D. J., & Chen, L. 2013, The Astrophysical Journal, 771:3

Zank, G. P., & Matthaeus, W. H. 1992, Journal of Plasma Physics, 48, 1, 85-100

M. Zhang, et al. 2003, Journal of Geophysical Research, 108, 1154

Zhang, J., Ma, J., & Wang, H. 2006, The Astrophysical Journal, 649, 464

Zimbardo, G. 2005, Plasma Physics and Controlled Fusion, 47, B755

Zimbardo, G., Pommois, P., & Veltri, P. 2006, The Astrophysical Journal, 109, L91

Zimbardo, G., Bitane, R., Pommois, P., and Veltri, P. 2009, Plasma Physics and Controlled Fusion, 51, 015005

Zimbardo, G., and Perri, S. 2013, The Astrophysical Journal, 778, 35

Zimbardo, G. et al. (2015) Journal of Plasma Physics, in press

Acknowledgements

Desidero ringraziare il Prof. Francesco Malara per avermi seguito lungo tutti questi tre anni, che hanno portato alla realizzazione di questo lavoro. Senza la sua competenza scientifica e la sua pazienza tutto questo non sarebbe stato realizzabile. Mi auguro di potere continuare a imparare da lui sempre.

I'd like to thank Prof. William H. Matthaeus from University of Delaware. The third chapter of this thesis is the result of the seven months of work done togheter at the University of Delware. I'm grateful to him for everything he taught me and for giving me the possiblity to have a wonderful experience in the USA. I hope to keep learning from him too. I would like also to thank the collegues from UD: Rohit Chhiber, Prachanda Subedi, Tulasi Parashar, Jeff Tessein, Debanjan Sengupta, Minping Wan, Michael Shay). I thank Prof. Sean Ougthon from University of Waikato for providing RMHD fields used for the study described in the third chapter of this work.

Desidero anche ringraziare tutti i colleghi del gruppo di Astrofisica e Plasmi dell'Università della Calabria (Luca Sorriso, Franco Valentini, Oreste Pezzi, Claudia Rossi, Silvia Perri, Francesca Di Mare, Elisa De Giorgio, Giusy Nigro, Vincenzo Carbone, Fabio Lepreti, Antonella Greco, Gaetano Zimbardo, Pierluigi Veltri, Sandra Savaglio, Leonardo Primavera, Sergio Servidio, e i miei "coinquilini" Tommaso Alberti e Christian Vásconez) per tutte le stimolanti discussioni avute durante le riunioni bibliografiche setti-

manali e non solo.